DØ Note
2422

Search for the Top Quark
in the
Dielectron Channel in $p\bar{p}$ Collisions at $\sqrt{s} = 1.8$ TeV

A Dissertation

Submitted to the Graduate School
of the University of Notre Dame
in Partial Fulfillment of the Requirements
for the Degree of
Doctor of Philosophy
by

Balamurali V

Nripen N. Biswas, Director

Department of Physics
Notre Dame, Indiana
November 1994

Search for the Top Quark

in the

Dielectron Channel in $p\bar{p}$ Collisions at $\sqrt{s} = 1.8$ TeV

Abstract

by

Balamurali V

A search was performed for $t\bar{t} \rightarrow ee + X$ events in $p\bar{p}$ collisions at $\sqrt{s} = 1.8$ TeV using 13.5 ± 1.6 pb^{-1} of data collected by the D0 detector at Fermilab during the 1992-93 collider run. One analysis of this data which was optimized to search for the top quark in the mass region $\sim 90 - 120$ GeV/c^2 yielded one candidate event with an expected background of 0.5 ± 0.3 events. When combined with top quark searches in other decay channels at D0, this yielded a lower limit on the mass of the top quark of 129 GeV/c^2 (at 95% CL). Another analysis of the same data was optimized to search for top masses > 120 GeV/c^2. This analysis combined with similarly optimized top quark searches in other decay channels gives 9 events with an expected background of 3.8 ± 0.9. Assuming that the number of events over the expected background is associated with top production, the $t\bar{t}$ production cross section is determined to be 8.2 ± 5.1 pb for an assumed top mass of 180 GeV/c^2.

This dissertation is dedicated to my parents.

TABLE OF CONTENTS

LIST OF FIGURES

LIST OF TABLES

ACKNOWLEDGEMENTS

I would like to thank my advisor Nripen Biswas for his guidance. He was always available for help, was always encouraging and was the reason for me being able to take part in the D0 experiment. I thank Meena for being my 'advisor' at Fermilab. Without her I would never have completed my dissertation work in any reasonable amount of time. I learned a great deal from her. She was also a friend who constantly looked out for me. I thank Jadzia for her guidance during my detection simulation work for the D0 upgrade. She was also a friend from whom I learned more than just physics. I thank Raja for his help and encouragement when I first joined the experiment. Raja and Serban and later Boaz and Nick led the top group very successfully and I am thankful for their tremendous effort. I thank Mont and Uli for their invaluable advice at very crucial times, when i needed them most. I would like to thank Jim, Srini, Meena, Uli and Bob for reading my dissertation and suggesting corrections. They also along with Sailesh, Vipin, Mrinmoy, Ashutosh, Jeff, Brajesh and Ray endured my 'practice' talks till I became better. I would also like to thank many people from Notre Dame: Ikaros Bigi for his constant encouragement and confidence in me, which was very important to me, Paul Kenney, Randy Ruchti, Mitch Wayne, Neal Cason and Bill Shephard for always being friendly and encouraging and John LoSecco for always being friendly and asking stimulating physics questions, Jim for his help with the computers, Lesley for being very friendly and helpful with all paperwork and Kathi, Tina and Sharon for their friendly help in the physics office.

My stay here has been made enjoyable by many friends, without whom work would

have become very hard. I must first thank Ashish for being a very good friend for all the five years I have known him, Ajay and Gokul for being friends and helping me get through hard times. I want to thank my classmates Benny, for helping me so much during my initial days here, Wu Xiang, Christian, Wu Zeyuan and Joe, my teachers and friends Michael and Ani, and my office mates Tony, Peter and Ray Mountain. I would also like to thank Ajay Chandhok, Seema, Rajiv and Madhu, Uma, Srini, Vasundhara, A. K., and 'tiger'. At Fermilab I would like to thank Sailesh, Vipin, Mrinmoy, Satyadev, Ashutosh, Brajesh, Srini, Shankar, Prem and Prajakta, Meena and Uli, and Dhiman and Sudeshna for all the good times I have had with them and my house mates Bob and Mike for all the fun and the fun discussions.

CHAPTER 1

INTRODUCTION

This chapter provides a brief introduction to the top quark and thus provides the motivation for this thesis. An outline of the standard model is provided first - as it is the building blocks of this model which predicts the existence of the top quark[1]. Indirect evidence for the existence of the top quark, its production at the tevatron and decay, the signature of the dielectron decay channel and the backgrounds are then discussed.

1.1 The Standard Model and Top Quark

The standard model (SM) describes the fundamental particles of nature and the interactions between them (except for gravity). The model has been very broadly tested [2] and found to predict all experimental data in high energy physics successfully. In the SM description all matter is made of two kinds of fundamental fermions — quarks and leptons. Both of them are structureless and point like on a scale of 10^{-17} m [3]. Both of them can further be classified into three families (also called generations). Each family is a replica of the others except that the particles in different family have different masses.

[1]At present there is evidence for the existence of the top quark from the CDF collaboration [1]. However as most of the analysis was done before this evidence was published, the tone of all arguments do not reflect the existence of this evidence.

The three generations of leptons are

$$\begin{bmatrix} e \\ \nu \end{bmatrix} \quad \begin{bmatrix} \mu \\ \nu_\mu \end{bmatrix} \quad \begin{bmatrix} \tau \\ \nu_\tau \end{bmatrix} .$$

The leptons interact through the weak and electromagnetic (if charged) forces but not the strong force. The e, μ and τ have an electric charge of $-1e$ while the corresponding neutrinos do not carry any electric charge.

The three generations of quarks are

$$\begin{bmatrix} u \\ d \end{bmatrix} \quad \begin{bmatrix} c \\ s \end{bmatrix} \quad \begin{bmatrix} (t) \\ b \end{bmatrix} .$$

Unlike the leptons the quarks experience the strong interaction in addition to the weak and electromagnetic interactions. This is because they carry the color charge responsible for the strong interaction. There are three color charges called red, yellow and blue and each quark mentioned above comes in the three colors. The quarks in the top row (u, c and t) have an electric charge of $+2/3e$ while the quarks in the bottom row (d, s and b) have an electric charge of $-1/3e$. Additional information about quark and lepton properties is given in table 1.1.

All the fermions mentioned above have antiparticles. They have the same mass as the original particles but the quantum numbers have the opposite sign. Only fermions in the the first generation are stable, the others decay to fermions in a lower mass family and are believed to have played a major part in the initial stages of the big bang.

The interactions between the fermions is described by local gauge theories. In these theories the dynamics of the interaction are related to symmetry principles and conservation laws. Symmetry operations (transformations) on objects in the

Table 1.1. Properies of Leptons and Quarks.

	Mass	Charge	Weak Isospin	flavor
	LEPTONS			
e	0.511 MeV	-1	-1/2	-
ν_e	< 7.3 eV	0	1/2	-
μ	105.9 MeV	-1	-1/2	-
ν_μ	< 0.27 MeV	0	1/2	-
τ	1784 MeV	-1	-1/2	-
ν_τ	< 35 MeV	0	1/2	-
	QUARKS			
up (d)	~ 10 MeV	-1/3	-1/2	
down (u)	~ 5 MeV	2/3	1/2	
strange (s)	~ 200 MeV	-1/3	-1/2	S=-1
charm (c)	~ 1500 MeV	2/3	1/2	C=1
bottom (b)	~ 5000 MeV	-1/3	-1/2	B=-1
top (t)	?	2/3	1/2	T=1

theory which leave the physical laws unchanged after the operation has been applied, are called invariances of the law. In local gauge theories the requirement of local (meaning that different transformations are carried out at different individual space time points) invariances essentially determine the form of the force laws. In the SM symmetry operations belonging to the symmetry group $SU(3)_{color}$ describe the strong interaction between quarks. Symmetry operations of the symmetry group $SU(2)_L \times U(1)$ describe the unified weak and electromagnetic interactions between all particles.

The $SU(3)_{color}$ non-abelian local gauge theory successfully describes the following properties of the strong interaction. 1) The interaction is independent of the flavor of the quarks. 2) It conserves the flavor quantum number of quarks. 3) The potential energy between two colored particles increases with the distance between them. This means that it would take infinite energy to separate a quark from a hadron — this is called color confinement (see next paragraph). 4) The interaction becomes weaker

with increasing energy and tends asymptotically towards zero (asymptotic freedom).

The strong interaction between the quarks are mediated by the 8 gauge bosons of a $SU(3)_{color}$ non-abelian local gauge theory. These are massless spin 1 particles called gluons. The non-Abelian nature of the local gauge theory makes the gluons carry color charge. This means that they change the color of the quarks and that they can interact amongst themselves. This property of the gluons is responsible for asymptotic freedom. There are compelling arguments [4] that this is responsible for the confinement of color also (property 3 above).

The $SU(2)_L \times U(1)$ electroweak theory is the unification of the weak interaction (described by $SU(2)_L$) with quantum electrodynamics ($U(1)$) through spontaneous symmetry breaking which also gives rise to the masses of the vector bosons mediating the weak interactions. This symmetry is broken in a special way — the Lagrangian retains the gauge symmetry but the symmetry is spontaneously broken in the ground state of the system. This requires the presence of a symmetry breaking spin 0 Higgs field [5]. In the minimal standard model only a single Higgs $SU(2)_L$ doublet is required.

The four gauge bosons of the Electroweak theory are W^α where α = 1,2,3 and B (associated with $SU(2)$ and $U(1)$ respectively). The $W^\pm$ weak bosons are $(W^1 \mp iW^2)/\sqrt{2}$ whereas the Z and photon (A) are given by the following linear combinations:

$$Z = W^3 \cos\theta_W - B \sin\theta_W$$

$$A = W^3 \sin\theta_W + B \cos\theta_W .$$

Here θ_W is called the electroweak mixing angle or the Weinberg angle. The W bosons cause charge changing weak interactions which involve transitions of the type $u \leftrightarrow d$ or

$e \leftrightarrow \nu_e$ in each family. Here only the left handed fermions take part in the interaction. The fermions are therefore included in a $SU(2)_L$ weak isospin(T) group with T=1/2. u, c and t have T_3 of 1/2, whereas d, s and b have T_3 of -1/2. The leptons also have the same T_3 values as the quarks. The right handed fermions are assigned to a weak isospin singlet and do not couple to the W^α. The Z causes neutral current interactions such as $\nu_\mu e \rightarrow \nu_\mu e$ and $\nu_\mu N \rightarrow \nu_\mu X$. Also they have a coupling to right handed fermions because of the electroweak mixing.

The characteristics of the interactions are tabulated in table 1.2 (see [6]). From the

Table 1.2. Characteristics of interactions.

	QED	QCD	Weak
Gauge group	U(1)	$SU(3)_{color}$	$SU(2)_L$
Vertex coupling	-ieQ	$-ig_s\frac{\Lambda^\alpha_{ij}}{2}$	$-ig\frac{\tau^\alpha_{ij}}{2}$
Gauge bosons	photons	8 gluons	3 weak bosons
Mass (GeV/c^2)	0	0	80-90
Range (m)	∞	$\leq 10^{-15}$	10^{-18}
Typical σ (m^2)	10^{-33}	10^{-30}	10^{-44}
Typical τ (s)	10^{-20}	10^{-23}	10^{-8}

properties of the electroweak interaction mentioned above it should not be possible for quarks in heavier families to decay to quarks in lighter families. However charge changing weak interactions of the type $u \leftrightarrow s$ and $u \leftrightarrow b$ are observed in addition to the type $u \leftrightarrow d$. This can be accounted for by assuming that the eigenstates of the electroweak Hamiltonian are not the eigenstates of the mass Hamiltonian. The transformation from the mass eigenstates to the electroweak eigenstates has been experimentally determined and is given by the Kobayashi-Maskawa matrix. The

matrix is unitary and is

$$\begin{pmatrix} V_{ud} & V_{us} & V_{ub} \\ V_{cd} & V_{cs} & V_{cb} \\ V_{td} & V_{ts} & V_{tb} \end{pmatrix} = \begin{pmatrix} 0.973 & 0.23 & \simeq 0 \\ \simeq 0.23 & \simeq 0.97 & \simeq 0.05 \\ \simeq 0 & \simeq 0.05 & \simeq 1 \end{pmatrix}.$$

This matrix accommodates CP violation in a natural manner [7] — CP violation is a phenomenon where processes and their CP (Charge conjugation and Parity operations applied together) conjugates do not occur with equal probabilities (it is observed to be be different by one part in a thousand). This is because a 3×3 unitary matrix cannot be written in such way that the phases are removed by redefining the wave functions. The weak interaction therefore contains complex numbers and a Hamiltonian that contains complex numbers violates time-reversal (T) invariance [7] and consequently CP invariance as for any quantum field theory CPT is invariant. The matrix is not calculable by the SM however, and so it is not known whether the phase angle is the source of CP violation.

1.2 The Top Quark

The top quark can be expected to exist from the SU(2) symmetry structure of the standard model, on the grounds of mathematical elegance. In addition there exist several indirect experimental evidences for the existence of the top quark. Three of them are given below. All these show that the b quark has the third component of isospin, $T_3 = -1/2$ and hence should have an $T_3 = 1/2$ partner, which by definition is the top quark.

1) *The branching ratio of b decays to lepton pairs*: Assuming that the b quark is a member of a weak isospin doublet, the branching ratio for the process $b \rightarrow l^+l^-X$ is expected to be less than 3×10^{-6} [8]. This is due to contributions from higher order diagrams (the lowest order contribution from Z is nil). If on the other hand the b

quark is a singlet the ratio

$$\frac{\Gamma(b \to l^+ l^- X)}{\Gamma(b \to l^+ \nu X)}$$

has been predicted to be ≥ 0.12 [9]. Using the experimental value of 0.104 for the $b \to l^+ \nu X$ branching ratio, the above limit translates to a lower limit of 1.2×10^{-2} on $\Gamma(b \to l^+ l^- X)$. Several experiments have looked at this quantity and set an upper limit of 1.2×10^{-3} [8] which is inconsistent with the hypothesis of the b quark having weak isospin 0.

2) *The forward backward asymmetry (A_{FB}) in the production of b quarks at e^+e^- collisions*: The production of b quarks at e^+e^- colliders, $e^+e^- \to b^+b^-$ occurs through both the Z and γ, as shown in figure 1.1. The contribution from the γ has a symmetric

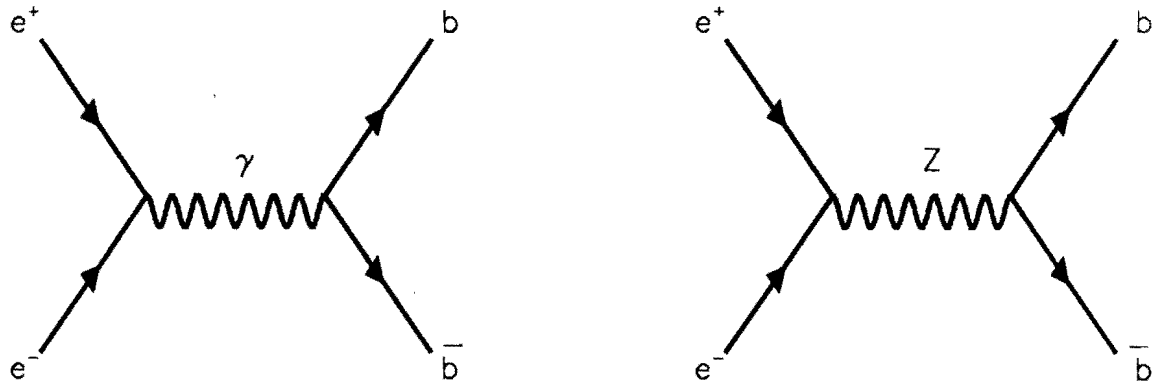

Figure 1.1. Diagrams contributing to $b\bar{b}$ production in e^+e^- collisions.

angular distribution about the plane perpendicular to the collision axis. However the

Z contribution is asymmetric. The value of A_{FB}, defined by

$$A_{FB} = \frac{\int_0^1 d\Omega \frac{d\sigma}{d\Omega} - \int_{-1}^0 d\Omega \frac{d\sigma}{d\Omega}}{\int_0^1 d\Omega \frac{d\sigma}{d\Omega} + \int_{-1}^0 d\Omega \frac{d\sigma}{d\Omega}}$$

should reflect this asymmetry and should be sensitive to the coupling of the b to the Z (the Z contribution). Here $\frac{d\sigma}{d\Omega}$ is the differential cross section and the limits are on $\cos\theta$ (θ is the polar angle). As the coupling of the b to the Z depends on the whether the b is a singlet or a doublet with the t quark, measuring A_{FB} provides information on the existence of the top quark. The coupling of the b to the Z is proportional to $T_{3L}^b + \frac{1}{3}\sin^2\theta_w$ where T_{3L}^b is 0 if the t quark does not exist and -1/2 if there is a t quark. A_{FB} and $\Gamma(Z \rightarrow b\bar{b})$ data give a value of $-0.504^{+0.018}_{-0.011}$ for T_{3L}^b [10] and hence the t quark exists (b quark is a doublet).

3) *The decay of the Z to b pairs*: The measurement of the coupling of the b to the Z can be used to determine T_{3L}^b as mentioned above. Measurement of $\Gamma(Z \rightarrow b\bar{b})$ provides another more direct way and it is found that the measured value again favours the existence of the top quark.

1.2.1 Previous Searches for the Top Quark and its Mass

The search for the top quark has been performed at many experiments. These searches have been of various natures. In some of them the standard model decay channels of the top quark are assumed to be correct - such searches have been carried out by the CDF and UA1 collaborations at $p\bar{p}$ collisions. These searches yielded lower limits on the mass of the top quark (m_t) — 91 GeV/c^2 at 95% confidence level (CL) [11]. Searches which are independent of the decay modes of the top quark like direct searches at e^+e^- colliders yield a lower limit of 46 GeV/c^2 [12, 13]. A decay independent limit of 62 GeV/c^2 at 95% CL is also obtained from the measurement of the

width of the W boson [14]. Several other measurements of parameters which depend on the mass of the top quark have also been made. Combining all these measurements gives the range of allowed m_t. The analysis done by D.Schaile constrains the mass of the top to be $178 \pm 11^{+18}_{-11}$ GeV/c^2 [15].

This thesis describes the search for the top quark in one of the standard model decay channels. It is assumed that the top decays only through the standard model decays channels and the top mass is higher than the highest lower limit on the mass of the top quark (viz. the CDF limit of 91 GeV/c^2). The decay channels and the production of the top quark at tevatron energies are described below.

1.2.2 Production at the Tevatron

The tevatron provides $p\bar{p}$ collisions at $\sqrt{s} = 1.8$ TeV. Here the top quark is expected to be mainly produced through $t\bar{t}$ pair creation [17]. The lowest order diagrams are shown in figure 1.2. The gg contribution to the total cross section varies from approximately 50% at a top mass of 90 GeV/c^2 to 10% at a mass of 200 GeV/c^2 [17]. The remaining contribution is from the dominant $q\bar{q}$ channel. The contribution from qg and $\bar{q}g$ channels is negligible.

A theoretical prediction of the top quark cross section is essential for our analysis. This is because there are several backgrounds which look like the top quark and the final event sample will always have a nonzero probability for containing background events. The top and the background cross sections are required at this point to assign a probability for the events to be background or top. The cross sections can also be used for determining the mass of the top or the lower limit on the mass of the top. This is because the experiment measures the cross section or the upper limit on the cross section — combining this with the theoretical predictions of the cross section which is made as a function of the top mass gives the top mass or the lower limit on the top mass.

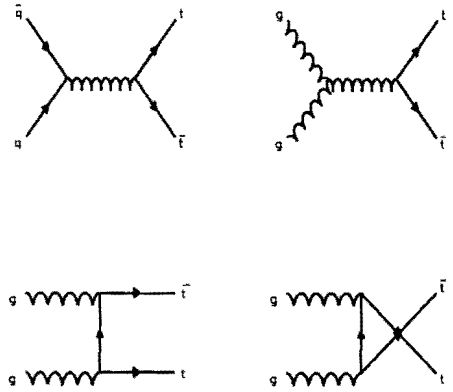

Figure 1.2. Lowest order diagrams for $t\bar{t}$ production from $p\bar{p}$ collisions.

The production rate of the top quark predicted by E. Laenen et al. [17] has been used for this analysis. Their calculation uses the exact order α^3 corrected cross section and the resummation of the leading soft gluon corrections in all orders of perturbation theory. During this resummation a new scale μ_0, which measures the sensitivity of the cross section to nonperturbative physics is introduced. The cross section for the production of the top quark is sensitive to this scale mainly through the contribution from the gg contribution. E. Laenen et al. give a central value of the cross section and a upper limit for the cross section by using two different values of this scale. These are shown in figure 1.3 by a solid curve and a dotted curve (above the solid curve) respectively. The other dotted curve (below the solid curve) is the lower limit on the cross section. Appendix A has the cross sections tabulated for m_t in the range of 90 to 200 GeV/c^2.

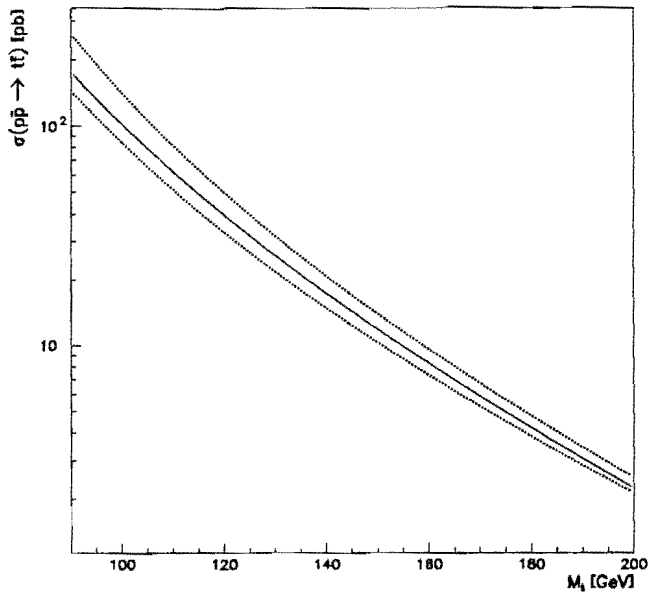

Figure 1.3. Production cross section for $t\bar{t}$ production at the tevatron. The solid curve is the central value. The dashed lines are the lower and upper limits on the cross section.

1.2.3 Standard Model Decay Channels

In this analysis we assume that the top quark decays according to the standard model. We also assume that the top quark mass is greater than the lower limit of 91 GeV/c^2, set at CDF. This means that the top quark will decay almost entirely to a b quark and a W, because the branching ratio is $\sim |V_{tb}|^2 \sim 1$. This decay has a very short lifetime which is $\sim 7.8 \times 10^{-25}$s for a top mass of 150 GeV/c^2 [16]. This is so fast that the top quarks produced in pairs decay before a toponium is formed.

As the top quarks decay to the W and b with a branching ratio of almost 1 the top decay channels are classified according to the decay channels of the W. Each W can decay leptonically or hadronically. The branching ratios to the various channels are given in table 1.3. The all jets channel in which both the Ws decay hadronically has the maximum branching ratio. However the QCD backgrounds for this channel which have a cross section many orders of magnitude greater than the top quark make

Table 1.3. Decay channels of Ws from $t\bar{t}$.

	$W_1 \rightarrow e\nu$ 1/9	$W_1 \rightarrow \mu\nu$ 1/9	$W_1 \rightarrow u\bar{d}$ 3/9	$W_1 \rightarrow c\bar{s}$ 3/9
$W_2 \rightarrow e\nu$ 1/9	1/81	1/81	3/81	3/81
$W_2 \rightarrow \mu\nu$ 1/9	1/81	1/81	3/81	3/81
$W_2 \rightarrow u\bar{d}$ 3/9	3/81	3/81	9/81	9/81
$W_2 \rightarrow c\bar{s}$ 3/9	3/81	3/81	9/81	9/81

it very difficult to look for the top in this channel. For this reason most searches for the top quark rely on the modes where at least one of the Ws decay leptonically to an electron or muon. Electrons and muons can be identified relatively cleanly unlike the tau which has a high background from QCD jets.

1.2.4 The Dielectron Decay Channel

The dielectron decay channel is the channel in which both the Ws decay to an electron. This is shown schematically in figure 1.4. This channel should have the following signature in the D0 detector. 1) The presence of two electrons with high transverse momentum (P_t). These electrons should also be well isolated considering the high mass of the top. 2) The presence of large missing transverse energy ($\not\!\!E_t$) indicating the presence of the neutrinos in the event. This is because the sum of the P_t of all particles produced in the event should be zero and when it is not zero it means that some particles have escaped detection. The undetected particles are neutrinos when the $\not\!\!E_t$ is large compared to the value expected from the resolution of the detector and the undetected low P_t particles close to the beam axis. 3) The presence of jets from the two b quarks from the top decay. The number of jets need not always be 2.

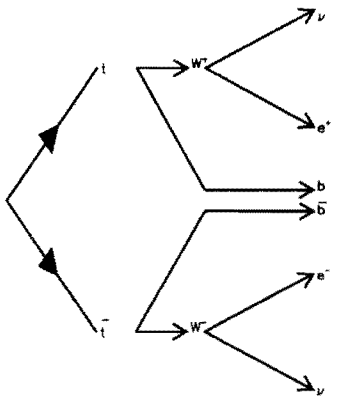

Figure 1.4. The dielectron decay channel.

It can be less than 2 when jets are merged or when the transverse energy of the jet is below the threshold imposed during the reconstruction of the event. The number of jets can be greater than two due to initial or final state radiation.

As seen from table 1.3 this channel has a branching ratio (BR) of 1/81 or 1.24%. The low BR on top of the small expected cross section for the production of the t means that the signal in this channel is going to be very small. However this channel is relatively clean compared to the other decay channels (as mentioned in the previous section) and is a promising channel to look for the top quark.

1.3 Backgrounds

There are several processes which can produce the signature of top decay to the di-electron channel mentioned above. It is important that the probabilities for such processes looking like the top be estimated so that one can understand the significance of the final signal observed. A detailed study of these backgrounds is therefore

necessary. The study is also necessary so that the analysis can be designed to make these probabilities small[2].

The background processes can be classified as physics backgrounds and instrumental backgrounds. The former are backgrounds in which the process topology and kinematics are such that they can actually look like a top decay process. The latter look like the top decay process only because some objects are misidentified (like a jet being identified as an electron). Some of the physics backgrounds are $WW \rightarrow ee$, $Z \rightarrow \tau\tau \rightarrow ee$ and $Z \rightarrow ee$. Some of the instrumental backgrounds are $W+$ jets and QCD multijet processes.

[2]It is the *number* of expected background events which is really important. However this depends on the cross section of the process and the probabilities mentioned above. As the cross section is a constant, the probabilities have to be brought down.

CHAPTER 2

THE TEVATRON AND THE D0 DETECTOR

This chapter describes the Tevatron and the D0 detector. The Tevatron is the accelerator which provides $p\bar{p}$ collisions at $\sqrt{s} = 1.8$ TeV . The detector used to study these collisions and which provided the data for this thesis is located at one of the two regions where the collisions take place. The location is called the D0 interaction region and hence D0 was the name to the detector. The present description of the detector is very brief and is only sufficient to aid in the understanding of the analysis described in the following chapters. More thorough descriptions are available in [18] and [19].

2.1 The Tevatron

The achievement of $p\bar{p}$ collisions is made possible by a series of accelerators culminating with the tevatron. The layout of these accelerators is shown in figure 2.1. The source of the protons is a magnetron surface plasma source [20] which delivers a pulsed 18 KeV negative hydrogen ion beam. This pulsed beam is first accelerated by a 750 KV potential provided by a Cockcroft-Walton electrostatic generator and then by a linac which raises the energy of the H_2 ions to 200 MeV. This beam from the linac is collected in a booster synchrotron which serves as the injector to the main ring (which is also another synchrotron). The collection of the beam is done for a duration equal to the time taken by the particles to complete six revolutions of the booster.

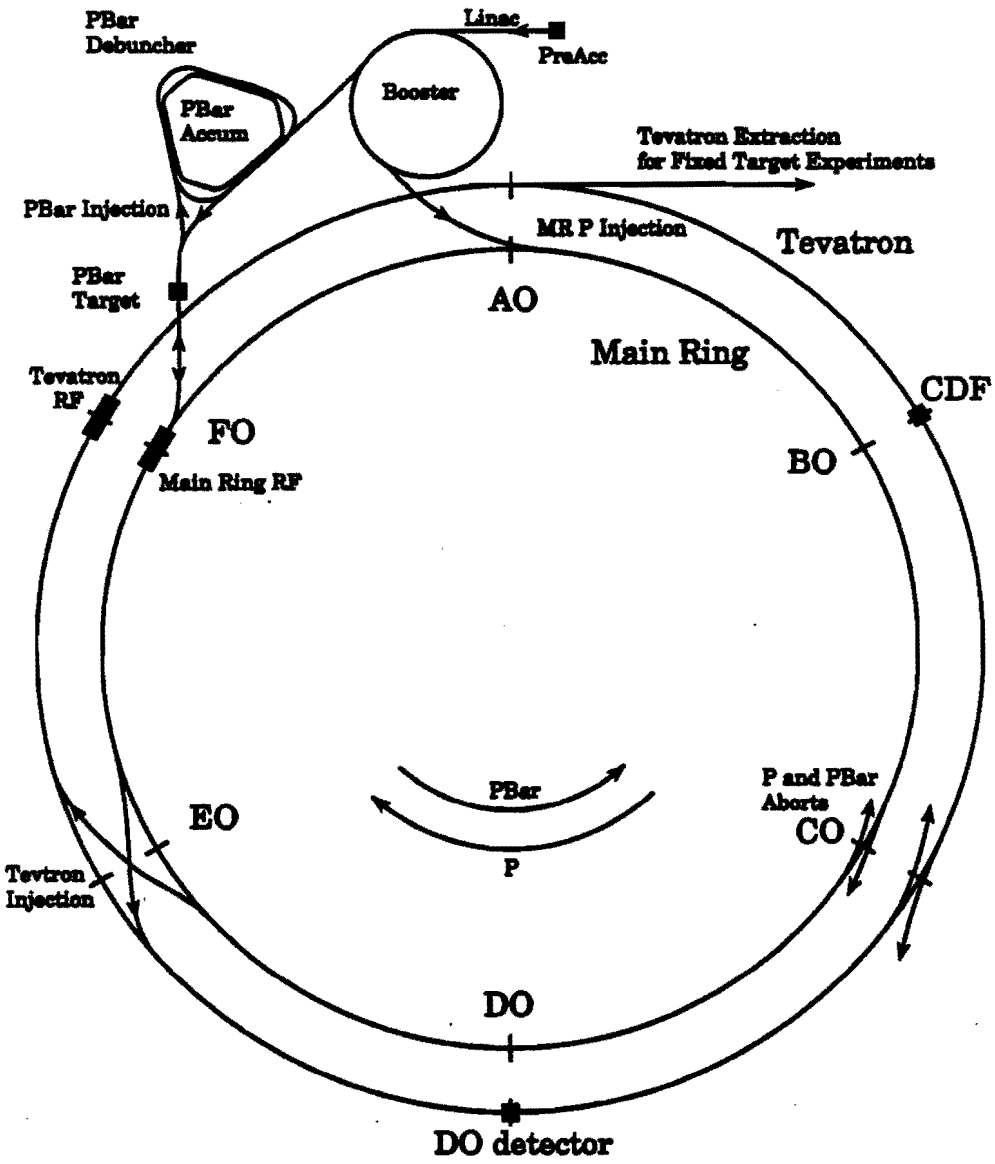

Figure 2.1. The layout of the collider facility at Fermilab.

During the collection the hydrogen ions are stripped of their 2 electrons by passage through a carbon foil. After collection they are accelerated to 8 GeV and injected into the main ring. 15 booster bunches are injected in the main ring before they are accelerated to 150 GeV, coalesced into one bunch and injected into an assigned spot in the tevatron, a synchrotron very much like the main ring but with superconducting magnets.

The antiproton source is more complicated than the proton source. Solving the technical problems in making the source paved the way for making colliders (a pp collider would be much more expensive as two accelerators would have to be built). Antiprotons are generated by operating the main ring to deliver a 120 GeV proton beam onto a nickel target. The target is such that about 10^7 antiprotons are generated at 8 GeV. These are then focussed by a lithium lens and passed through a pulsed dipole magnet which selects 8 GeV particles before they are sent to the debuncher. These antiprotons have a wide spread in momentum and are divergent. They are therefore 'cooled' to reduce the divergence and momentum spread. This is done in the debuncher and the accumulator. The method used is statistical (stochastic cooling). This relies on pickup coils which sense the deviation of the particles from an ideal orbit and send the information to a kicker magnet along a chord of the ring so that they can make corrections to the very same particles. The antiprotons are then injected into the main ring and then into the tevatron.

Six proton and antiproton bunches are injected into the tevatron at 150 GeV. They are then accelerated to 900 GeV so that collisions occur at a center of mass energy of 1.8 TeV. Special magnets placed upstream and downstream of the intersection region focus the beam to a small spot size (σ in the direction transverse to the beam is $\approx$ 40 μm) thereby increasing the luminosity. The longitudinal bunch length is however $\approx$ 30 cm. This results in a longitudinal spread of the event vertices with $\sigma \approx 30$ cm. Once the beams are setup collisions go on for up to $\sim$ 20 hours. During this

time the main ring is operated to produce antiprotons for setting up the beams again (The main ring separation from the tevatron at D0 is such that the main ring passes through the calorimeter. This is responsible for huge losses whenever a main ring bunch passes through the D0 detector [21]). The accelerator is discussed in great detail in [22].

2.2 D0 Detector Overview

The D0 detector was designed to attain several physics objectives. One of the principal aims was the discovery of new particles (like the top quark) and new phenomena. Such physics is expected to be associated with high p_t leptons, jets and large missing p_t. Thus, the detector was optimised to have [18],

1. very good electron identification and measurement,
2. identification of jets with good energy resolution,
3. good measurement of missing p_t and its direction, and
4. good muon identification.

The above characteristics were achieved with a design which consists of three major detector subsystems : The central detector, the calorimeter and the muon system. There is no central magnetic field. This is because calorimetry is the paramount tool in the detection of jets, leptons and missing p_t and the measurement of the energy and direction of these objects is not aided by having a central magnetic field [23]. Not having a central magnetic field also allows a calorimeter coverage unobstructed by the magnet coils and supports and compact construction of the tracking chambers. This and the use of Uranium as the absorber material for calorimetry results in a compact detector (keeps costs down). The three subsytems can be seen one nested inside the

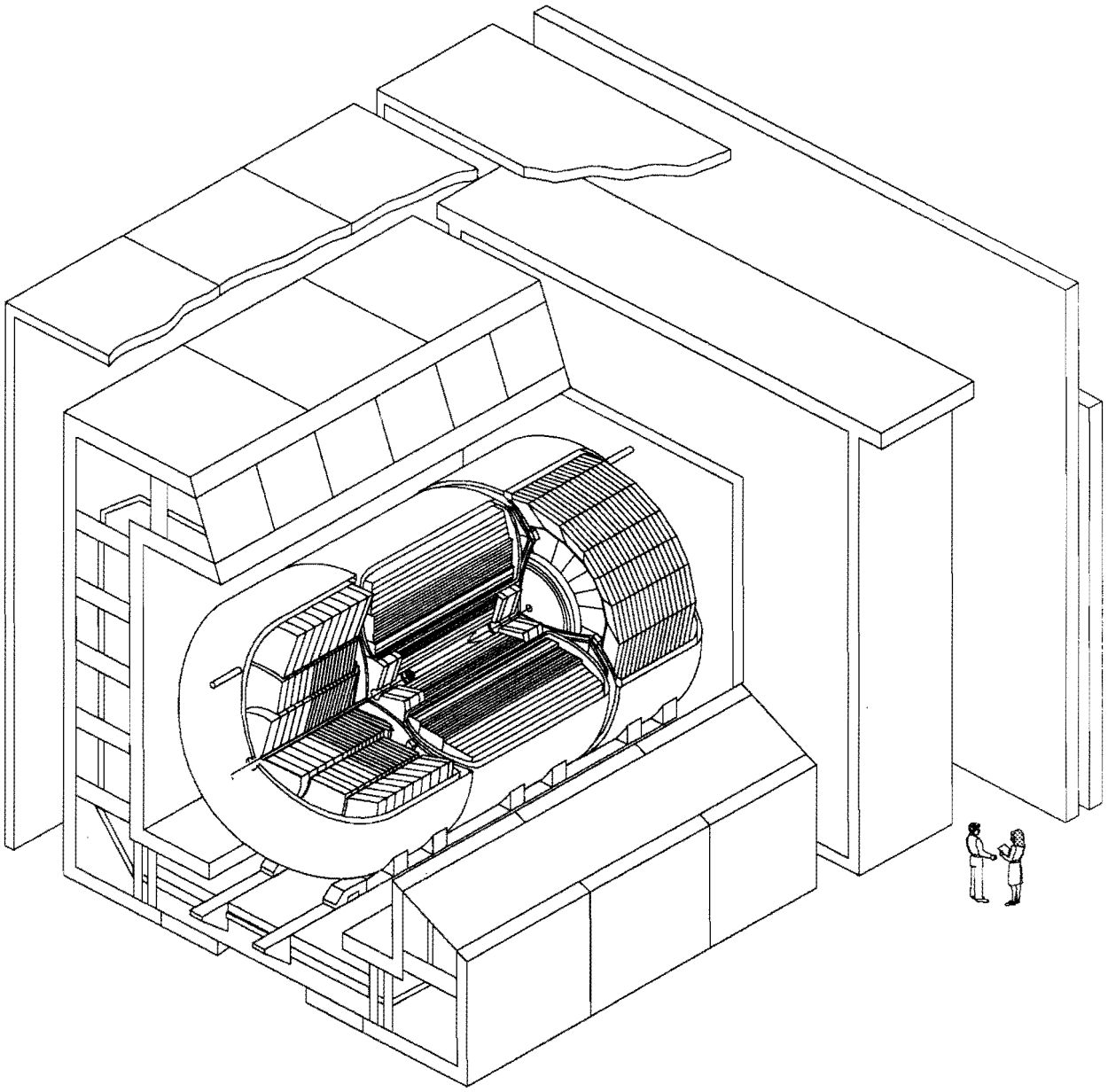

Figure 2.2. Isometric view of the D0 detector.

other in a cutaway view of the entire detector (figure 2.2). Figure 2.3 shows the elevation view. The support platform, the Tevatron beam pipe and the main ring are also shown in this figure. The support platforms house detector electronics and services for gas, power and cryogenics. The cables from the detector pass over an articulated bridge to the movable counting house (MCH) where the remainder of the electronics is located outside the Tevatron shield wall. The digitized data from the MCH is sent through high speed data cables to data acquisition processor nodes where they are recorded on 8 mm tapes. The next section describes the coordinate system used at D0. The following sections then describe each detector subsystem. The trigger and data acquisition systems are described in the next chapter when the online processing of events is discussed.

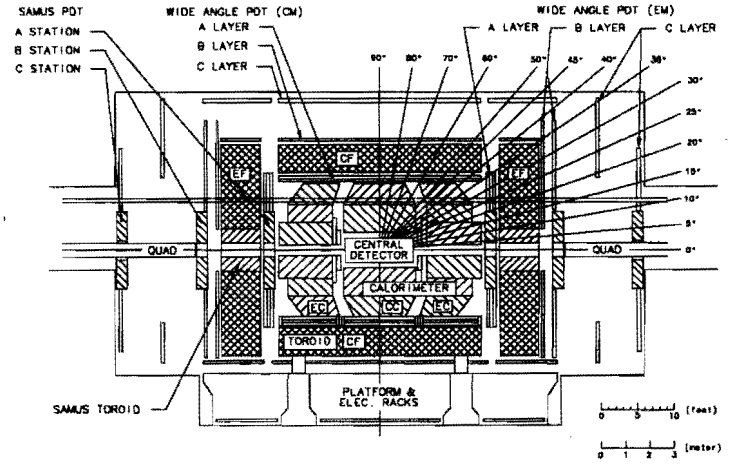

Figure 2.3. Elevation view of the D0 detector.

2.3 The D0 Coordinate System

The proton beam direction is chosen as the z axis with the nominal collision point (the center of the D0 detector) as the origin. The x axis is radially outward from the Tevatron ring. The coordinate system is right handed cartesian and therefore the

y axis is fixed and is vertically up. The radial distance r is then the distance from the beam axis, ϕ is the azimuthal angle about the beam axis and θ the polar angle subtended with the z direction. However the variable η is more often used than θ. It is given by the equation

$$\eta = -\ln(\tan(\frac{\theta}{2}))$$

and is approximately equal to the rapidity y (true for particles with $p \gg m$, p is the momentum, and m the mass of the particle) which has the advantage of being simply additive under Lorentz boosts along the z axis. The above coordinates are detector coordinates. Sometimes it is useful to talk in terms of physics coordinates for a particular event. These coordinates are defined the same way except that the origin is the interaction vertex of the event.

2.4 Central Detector (CD)

The CD consists of four detectors: 1) The vertex chamber (VTX) which is closest to the beam pipe performs tracking in the region $|\eta| < 2$, 2) the central drift chamber (CDC) which is farther away from the beam for further tracking in the central region, 3) the forward drift chamber (FDC) for tracking in the forward regions, and 4) the transition radiation detector (TRD) which aids in electron identification. An r-z view of the central detectors is shown in figure 2.4. The lack of a magnetic field in the central region allowed compact construction of these detectors. The tracking chambers (VTX, CDC, FDC) have good position resolution, two track resolving power, and good dE/dx (ionization per unit length of the track) measurement to differentiate overlapping tracks from unopened e^+ e^- pairs from photon conversions [23].

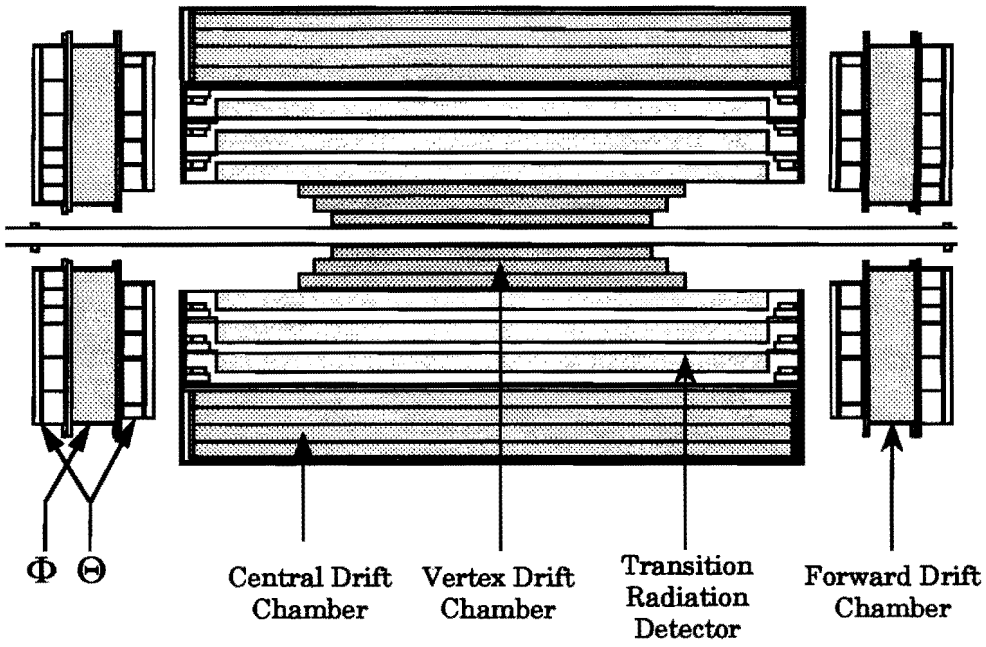

Figure 2.4. *r-z* view of the central detector.

2.4.1 The Vertex Chamber (VTX)

The VTX is made up of three layers of cylindrical drift chambers. The innermost layer is made of 16 cells in azimuth and the outer 2 layers are made of 32 cells each in azimuth. Each cell has 8 sense wires in the axial direction and are readout at both ends for measurement of the z coordinate by the charge division method. Adjacent sense wires are staggered by $\pm 100\ \mu m$ to resolve left-right ambiguities and the cells in different layers are offset in ϕ to further aid in pattern recognition. Fine field shaping is provided by the fine field, grid, cathode and sense wires. Coarse field shaping is provided by aluminium traces on carbon fiber support tubes. The location of these wires is shown in figure 2.5. The gas used for the operation of the VTX is CO_2-ethane at 1 atm with a small admixture of H_2O. In normal operation the gas is 'unsaturated', meaning the value of field per unit pressure (E/p) is not on the plateau of the curve of drift velocity vs. E/p. This is necessary to obtain the low drift velocity of 7.3 μm/ns which is required for a 50 μm resolution (table 2.1) given the 100 MHz

operation of the VTX electronics [24]. The average value of the electric field used is 1 kV/cm. Additional VTX specifications and its performance are provided in table 2.1 [18, 23, 25].

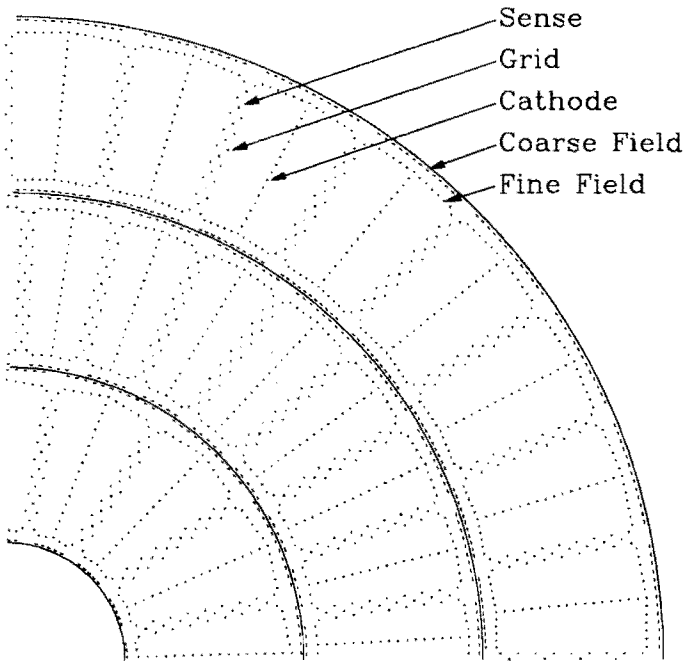

Figure 2.5. r-ϕ view of a quadrant of VTX.

Table 2.1. VTX specifications and performance.

Length	116.8 cm
Radial interval	3.7 to 16.2 cm
Number of layers	3
Azimuthal cells/layer	16,32,32
Sense wires/cell	8
Maximum drift distance	13.7 mm
Sense wire resolution	60 μm
Charge division resolution	1 cm
Pair resolution	0.7 mm

2.4.2 *The Transition Radiation Detector (TRD)*

The TRD is located just outside the VTX and covers the region $|\eta| < 1.2$. It consists of three separate cylindrical units each having its own radiator and detector. The radiator is made of 393 layers of 18 μm thick polypropylene foils separated by nitrogen gas with a mean spacing of 150 μm. The fluctuations in the spacing are also comparable to 150 μm. The energy spectrum of transition radiation X-rays generated by this configuration is peaked at 8 KeV and is mainly contained below 30 KeV. The detector for the X-rays is a two stage time-expansion type proportional wire chamber (PWC). The first stage is a 15 μm space filled with the operating gas (Xe/C_2H_6) for the conversion of the X-rays. The avalanche occurs in the second stage which contains the sense wires (anodes). Figure 2.6 illustrates the construction and also shows the location of the field shaping wires. Additional TRD specifications and performance numbers are provided in table 2.2 [18, 26, 27].

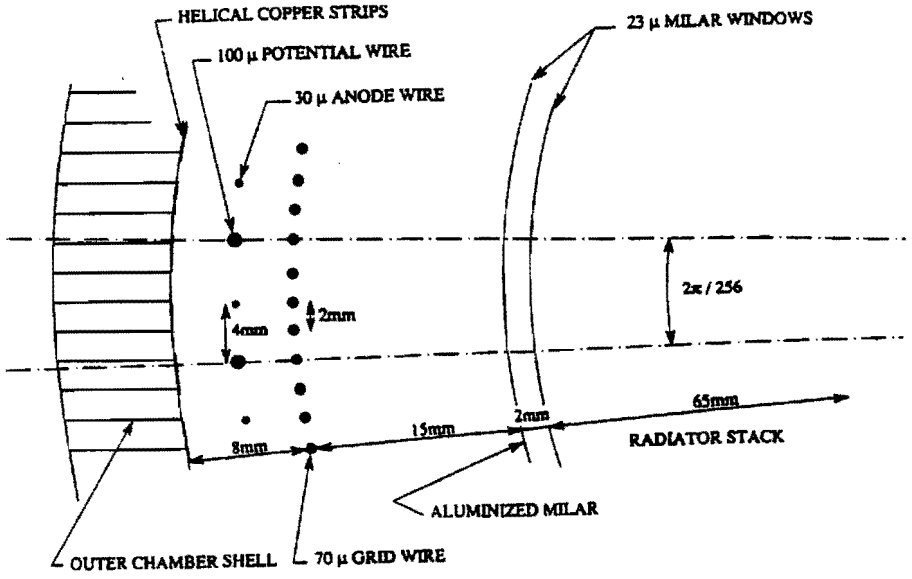

Figure 2.6. TRD radiator and proportional wire section.

Table 2.2. TRD specifications and performance.

Length	165 cm
Radial interval	17.6 to 47 cm
Number of layers	3
Sense wires/layer	256,256,512
e/π discrimination[a]	50:1

[a] at 90% efficiency

2.4.3 The Central Drift Chamber (CDC)

The CDC is located between the TRD and the central calorimeter and covers the η region from -1 to 1. Figure 2.7 shows the end view of few segments of the CDC. It is made up of 4 layers of cylindrical drift chambers . Each layer is made of 32 cells in azimuth. Each cell consists of 7 sense wires and 2 delay lines. The delay lines are readout at both ends for determination of the z coordinate from the difference in arrival time of the pulses at the two ends whereas the sense wires are readout at one end only. Adjacent sense wires are staggered by ± 200 μm to resolve left-right ambiguities and the cells in different layers are offset by half a cell to further aid in pattern recognition. Field shaping is provided by resistive strips printed on the kapton which covers each cell. The gas used for the operation of the CDC is $Ar(92.5\%)CH_4(4\%)CO_2(\%)$ with 0.5% H_2O. The drift velocity is 34 μm/ns with a drift field of 620 V/cm. Additional CDC specifications and performance numbers are provided in table 2.3 [18].

2.4.4 The Forward Drift Chamber (FDC)

The FDC extends tracking to the η regions $1 < |\eta| < 2$. The chambers are located just before the end calorimeters at both ends of the concentric barrels of VTX, TRD

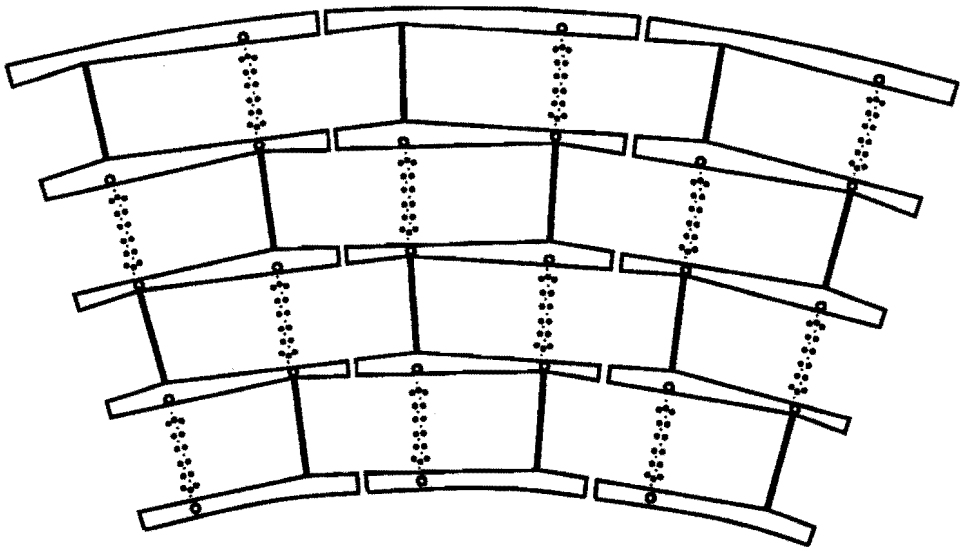

Figure 2.7. End view of three segments of CDC.

Table 2.3. CDC specifications and performance.

Length	179.4 cm
Radial interval	51.8 to 71.9 cm
Number of layers	4
Azimuthal cells/layer	32
Sense wires/cell	7
Maximum drift distance	70.8 mm
Sense wire resolution	200 μm
Delay line resolution	2 mm
Pair resolution	2 mm

and CDC. At each end the FDC consists of one Φ module sandwiched between two Θ modules. This is shown in figure 2.8 which also shows that the two Θ modules are rotated by 45 degrees with respect to each other.

The Θ modules are made of four quadrants, each of which is made of 6 cells. This is also illustrated in figure 2.8. Each of these cells have 8 sense wires and 1 delay line. The sense wires in the inner three cells are strung at one edge of the cell. The drift is therefore unidirectional and left-right ambiguities do not exist. The other cells have adjacent sense wires staggered by ± 200 μm to resolve the ambiguities. Calculation of the θ coordinate of a track requires information from the sense wires (read out at one end) and the delay lines (read out at both ends). Field shaping is provided by copper traces etched on the kapton which covers each cell. Two guard wires between each pair of sense wires provides additional fine field shaping.

The Φ module consists of 36 azimuthal cells. Each cell has 16 sense wires strung radially. Adjacent sense wires are staggered by ± 200 μm to resolve ambiguities. Like the Θ modules, field shaping is provided by copper traces etched on the kapton which covers each cell. However there is only one guard wire between each pair of sense wires which provides additional fine field shaping.

The operating gas for both the Φ and Θ modules is $Ar(93\%)CH_4(4\%)CO_2(3\%)$ at atmospheric pressure. The Θ modules are operated at 950 V/cm and the Φ at 750 V/cm. Additional information on the modules and their performance is provided in table 2.4 [18].

2.4.5 Central Detector Electronics

All the central detectors have identical electronics composed of three main stages: 1) Preamplification, 2) pulse shaping, and 3) analog to digital conversion.

Preamplification is accomplished by a hybrid IC based upon the Fujitsu MB43458 quad common base amplifier [19]. These preamplifiers are located on the chambers

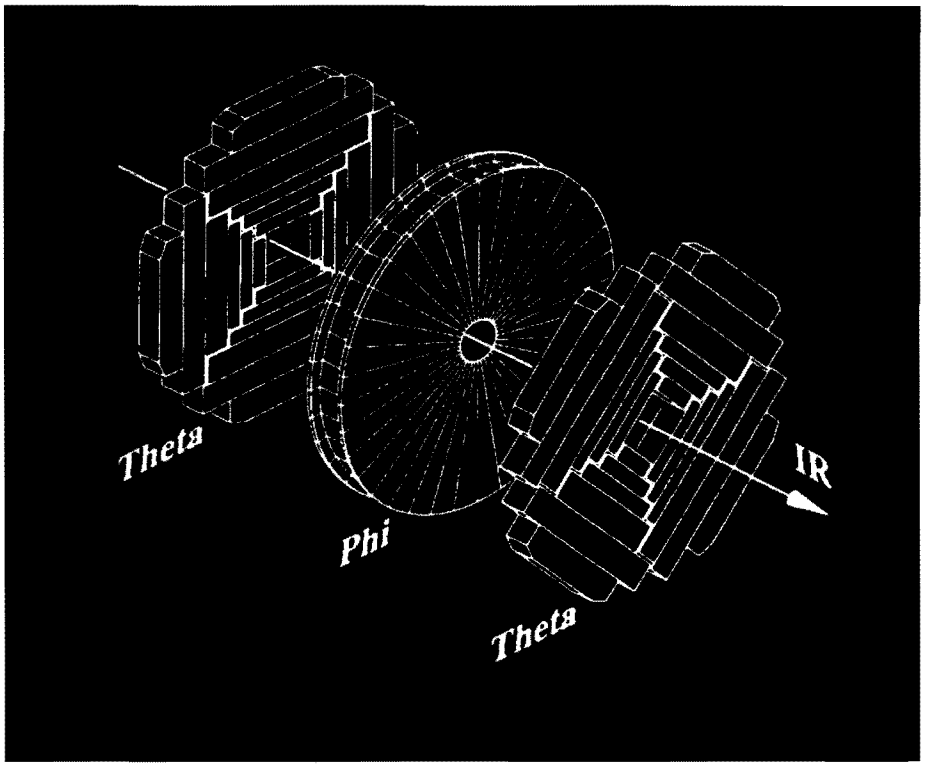

Figure 2.8. FDC Θ and Φ modules.

Table 2.4. FDC specifications and performance.

	Θ chamber	Φ chamber
$\|z\|$ intervals	104.8–111.2 cm	128.8 to 135.2 cm
Radial interval	11 to 61 cm	11 to 61 cm
Number of cells(wires)[a]	6	16
Sense wires/cell	8	16
Sense wire resolution	200 μm	200 μm
Delay line resolution	4 mm	20 mm
Pair resolution	2 mm	2 mm

[a]The number of cells along the radius for Θ chambers and the number of wires along z for Φ chambers

themselves. The output signal from these preamplifiers are carried to the detector platform, where the shaping circuits are located.

The shaping circuitry consists of a shaper hybrid amplifier and a header with individualized shaping components [28]. The two are mounted on separate printed circuit boards for each channel so that they can be adjusted according to the different gains and pulse shapes of each chamber. The amplification and shaping is done in 3 stages. Differential video amplifiers are used in the first and third stage whereas a single ended amplifier with a RC network is used in the second stage to provide cable compensation. The headers of the first and second stage have a one pole zero filter for shaping. The signal from the shaping circuits to the digital conversion electronics located in the MCH is carried by a 45 m coaxial cable with an impedance of 75 Ω .

Digitization is also done in three stages. The first stage is an analog buffer amplifier circuit. Voltage offset and gain correction are done here using programmed information for each channel. The gain correction amplifies large signals by a factor 8.5 less than that used for small signals thus increasing the dynamic range of the device. The second stage is based on a SONY eight bit flash analog to digital (FADC) converter, operated at 106 MHz. This performs the actual digitization whose output is stored in the front end memory. The data in the front end is dumped if the event is rejected by the level 1 trigger. Otherwise it is compressed in the third stage and stored in backend memory. This compression is done using a zero suppression (ZSP) circuit which suppresses pedestal data between pulses. More details about the central detector electronics can be found in [18] and [28].

2.5 Calorimeter

Calorimetry is very crucial for the D0 detector. This is because the absence of a central magnetic field makes the calorimeter the only system which provides energy measurement for electrons, photons and jets. The calorimeter is also required for the

identification of electrons, photons, jets and missing E_t.

The D0 calorimeter (figure 2.9) is a sampling calorimeter with Uranium/Copper/-stainless steel as the absorber and liquid Argon as the ionization medium. Liquid Argon offers the advantages of unit gain, radiation hardness and the relatively low cost of readout electronics. The disadvantage is the requirement of cryostats for maintaining the Liquid Argon at 86 K and the inaccessibility of the calorimeter modules during operation.

A typical calorimeter unit cell consists of an absorber plate and a signal board with the gap between them filled with liquid argon. This is illustrated in figure 2.10. The absorber plate is grounded and a positive voltage of 2.0-2.5 kV is applied to the signal board to create the electric field necessary to drift the electrons from the ionization medium (liquid argon) to the signal board. The signal board construction is of two different types depending upon the location of the board. When the gap between neighbouring azimuthal sectors is critical the signal boards are made of multilayer printed circuit boards. The outer surfaces are coated with a high resistivity carbon loaded epoxy and the required segmentation is provided by etched pads on an interior surface. The signal from these pads is brought out by traces on another interior surface. The other signal boards consist of copper pads sandwiched between two 0.5 mm G-10 sheets having the same resistive coating on the outer side. The signal board in figure 2.10 is of the latter type. Readout cells are formed by ganging together several signal boards with approximately the same $\Delta\eta$ and $\Delta\phi$ in depth.

As shown in figure 2.9 the calorimeter is divided into three sections: The central calorimeter (CC) which covers the central region and 2 endcap calorimeters (EC) which cover the forward region. Figure 2.9 illustrates this and also the hermiticity of the calorimeter.

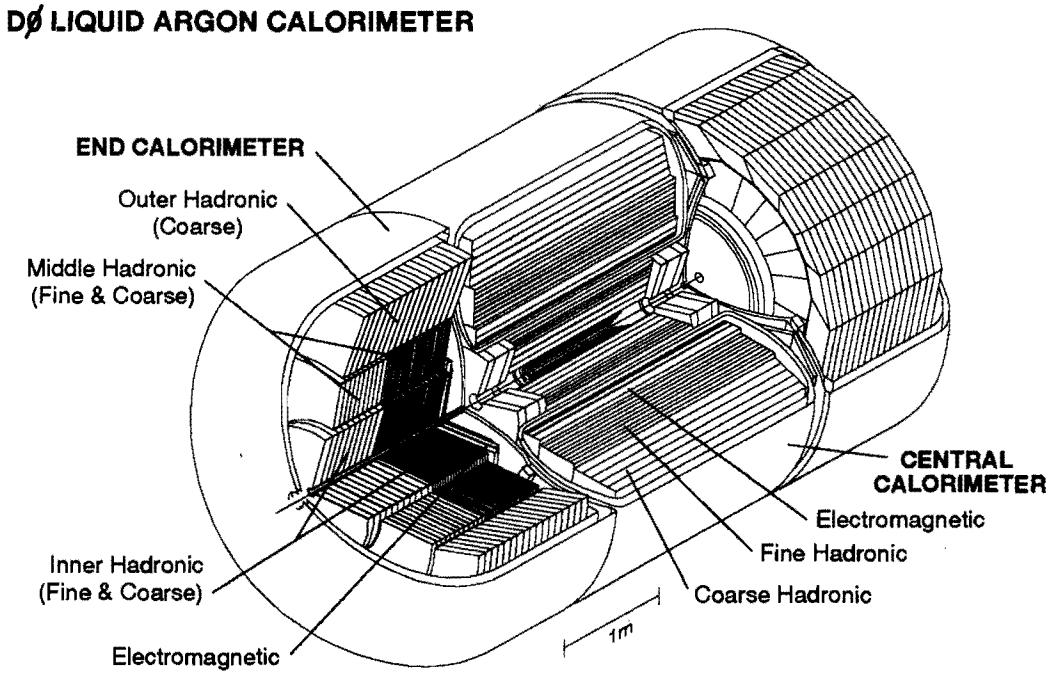

Figure 2.9. Isometric view of calorimeter.

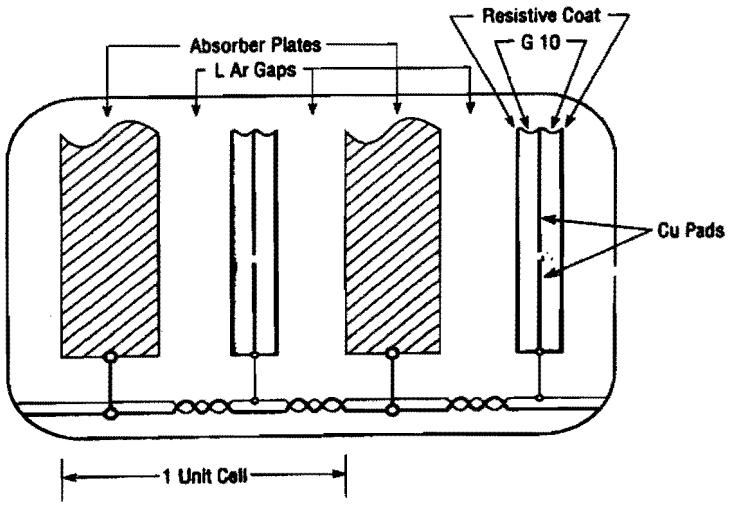

Figure 2.10. Schematic view of a calorimeter cell.

2.5.1 The Central Calorimeter (CC)

The CC consists of three concentric cylindrical layers. The innermost layer is made up of 32 azimuthal electromagnetic (EM) modules. These modules use 3 mm thick uranium as the absorber. The signal boards readout cables are ganged into 4 longitudinal layers called EM1 through EM4, with EM1 being the innermost and EM4 the outermost. The layers have 2.0, 2.0, 6.8, and 9.8 radiation lengths (X_0) of material respectively. The transverse segmentation is $\Delta\eta = 0.1$ and $\Delta\phi = 0.1$ except in EM3 where it is 0.05×0.05. Just outside the EM layer are 16 azimuthal fine hadronic (CCFH) modules. Here the absorber is 6 mm thick uranium and there are only 3 longitudinal readout layers with 1.3, 1.0, and 0.9 absorption lengths (λ_A) of material respectively. As for the EM1, 2 and 4, the transverse segmentation is 0.1×0.1. The outermost layer consists of 16 azimuthal coarse hadronic (CCCH) modules. The absorbers are 46.5 mm copper plates and there is only 1 longitudinal readout layer

with 3.2 λ_A of material. The transverse segmentation is again 0.1×0.1. Table 2.5 lists the important specifications for the CC. Performance factors for the CC are given in table 2.6 [18, 29].

Table 2.5. CC specifications.

	EM	FH	CH
Number of modules	32	16	16
Absorber	Uranium	Uranium	Copper
Absorber thickness (mm)	0.118	0.236	1.625
Argon gap (mm)	0.09	0.09	0.09
Number of cells/module	21	50	9
Number of layers	4	3	1
Cells per readout layer	2,2,7,10	20,16,14	9
Radiation length/cell	0.975	1.92	3.29
Absorption length/cell	0.036	0.0645	0.317
Total radiation length	20.5	96.0	32.9
Total absorption length	0.76	3.23	33.17

Table 2.6. CC and EC performance factors.

Energy resolution - electromagnetic	$15\%/\sqrt{E}(\text{GeV}) + 0.3\%$
Energy resolution - hadronic	$50\%/\sqrt{E}(\text{GeV}) + 4\%$
Position resolution (EM)	$2\ \text{cm}/\sqrt{E}(\text{GeV})$

2.5.2 The Endcap Calorimeters (EC)

The two endcap calorimeters extend the calorimeter coverage up to $|\eta| = 4.5$. They are similar in construction to the central calorimeter in gap structure, readout structure, and segmentation. They also contain EM and hadronic sections but these portions are distributed differently in four types of modules. The absorber plates are the same in EM and fine hadronic portions but the coarse hadronic portions use 46.5

mm stainless steel plates instead of copper. Transverse segmentation is also the same except for $3.2 < |\eta| < 4.5$ where it increases from 0.2×0.2 to 0.4×0.4.

The location of the four modules is illustrated in figure 2.9. The innermost module (ECEM) contains a single EM portion. As for the CC, it also has four readout layers (termed EM1 through EM4). These have radiation lengths of 0.3, 2.6, 7.9 and 9.3 respectively. However, the material of the inner cryostat wall brings the total radiation length of EM1 to 2.0. Behind the ECEM modules are 2 inner hadronic (ECIH) modules. The fine hadronic part has 4 readout sections, each containing 16 absorber plates while the coarse hadronic portion has a single readout section containing 13 absorber plates. The middle hadronic (ECMH) and outer hadronic (ECOH) are concentric layers outside the ECEM and ECIH modules. The ECMH has 4 FH portions of $0.9\lambda_A$ each and 1 CH section of 4.4 λ_A whereas the ECOH has only one CH section of 4.4 λ_A. Detailed specifications of the EC are given in table 2.7.

Table 2.7. EC specifications.

	EM	IFH	ICH	MFH	MCH	OH
Number of modules	1	1	1	16	16	16
Absorber[a]	U	U	U	U	SS	SS
Absorber thickness (mm)	0.118	0.236	0.236	0.236	1.83	1.83
Argon gap (mm)	0.09	0.082	0.082	0.087	0.087	0.087
Number of cells/module	18	64	12	60	14	24
Number of layers	4	4	1	4	1	3
Cells per readout layer	2,2,6,8	4x16	12	4x15	12	3x8
Total radiation length	20.13	121.8	32.78	115.5	37.95	65.07
Total absorption length	0.949	4.912	3.573	4.045	4.084	7.006

[a] U=Uranium,SS=Stainless steel

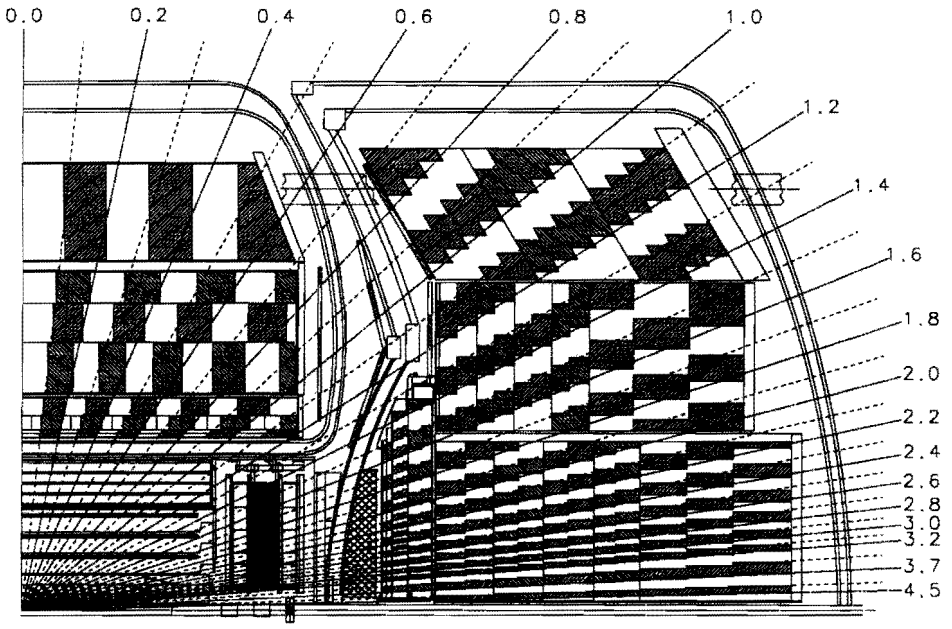

Figure 2.11. Schematic view of calorimeter segmentation.

2.5.3 Intercryostat Detector (ICD) and Massless gaps (MG)

As can be seen in figure 2.11, the region $0.8 < |\eta| < 1.4$ contains a significant amount of dead material (support structures, module endplates etc.). The ICD and massless gaps help to compensate for the energy deposited in this region. The ICD consists of 384 scintillator tiles mounted on the inner surface of the EC. The tiles have a size of 0.1×0.1 in $\Delta\eta \times \Delta\phi$ and exactly match the liquid argon calorimeter cells. The massless gaps consist of single cells which have only the liquid argon and signal boards and are located in the CCFH, ECMH, and ECOH modules.

2.5.4 Calorimeter Electronics

Signal processing for the calorimeter starts with preamplification electronics located in four enclosures on the surface of each cryostat. The signal is brought to these

enclosures in two steps. In the first step Tefzel insulated 30 Ω coaxial cables carry the signal from the calorimeter modules to 4 cryostat feedthrough ports. 8 T-shaped feedthrough boards which penetrate each port, reorder the module oriented input side to η-ϕ order and bring the signal outside. Short cables then carry the signal to the preamplification enclosures. The charge-sensitive hybrid preamplification has two different gains to provide full dynamic range response.

The preamplifier output is carried by twisted pair cables to the baseline subtracter (BLS) shaping and sampling hybrid circuits located in the detector platform. The circuits sample the signal just before each beam crossing and 2.2 μs after. The difference of the two is provided as a DC voltage proportional to the collected charge. Two storage capacitors provide double buffering for each channel. The inputs for the level1 trigger are extracted at the input of the BLS with a rise time of $\simeq$ 100 ns.

The BLS outputs are amplified by a factor of 1 to 8 depending on the signal size, multiplexed by a factor of 16, and then sent on twisted pair cables from the detector platform to the MCH. 24-channel 12-bit ADC circuits in the MCH digitize the signal within 160 μs.

2.6 Muon System

The D0 muon system consists of toroidal magnets and proportional drift tubes (PDT) located outside the calorimeter. There are 5 toroidal magnets covering the region $|\eta| \leq 3.6$. The PDTs associated with the central toroid ($|\eta| \leq 1$) and the two endcap toroids ($1 < |\eta| \leq 2.5$) are called the wide angle muon system (WAMUS). The PDTs associated with the 2 smaller toroids covering the region $2.5 < |\eta| \leq 3.6$ are called the small angle muon system (SAMUS).

Each system consists of three sets of PDTs. One set of PDTs, located between the calorimeter and the toroid (layer A), consists of 4 wire layers. The remaining two sets (layers B and C) are located outside the toroid and consist of 3 wire layers each.

The wire layers (cells) are rectangular in cross section and vary in length from 2.5 to 6 m. Adjacent cells at different radii are staggered to resolve left right ambiguities. The wires are along the x-y plane so that the drift direction is parallel to the bend caused by the magnetic field which is approximately azimuthal. Track measurements along the direction of the wire are made using vernier cathode pads located at the top and bottom of each cell in conjunction with the measurement of difference in arrival time of the signal at the two ends of the wire. Each cathode pad consists of an inner and outer pad separated by a repetitive diamond shaped insulating pattern. The ratio of the charge induced on the inner and outer pads provides a measure of the coordinate along the wire, modulo the repeat distance of the diamond pattern (61 cm). This measurement along with the the approximate measurement from the signal arrival time difference at the ends of the wire gives the complete measurement along the wires.

The muon momentum is obtained by measuring the initial muon direction before it enters the toroid and the final direction after it passes the toroid. The initial direction is determined from the track coordinates from layer A and the primary interaction vertex. If the muon is isolated, information from the central tracker and energy deposits from the calorimeter can also be used. The final direction is obtained from track coordinates from layer B and layer C which are separated by 1 to 3 m. For low p_t muons the momentum resolution is dominated by multiple coloumb scattering in the toroid which limits $\delta p/p$ to 18% whereas the resolution of the drift chamber dominates for higher momenta. The resolution is given by the equation:

$$(\delta p/p)^2 = 0.18^2 + (0.01p)^2$$

when p is in GeV/c.

The amount of material encountered when passing through the calorimeter and

toroids varies from $9\lambda_A$ to $20\lambda_A$ for different Θs. This is illustrated in figure 2.12. The high number of λ_A reduce the amount of hadronic punchthrough which translates to very clean muon identification.

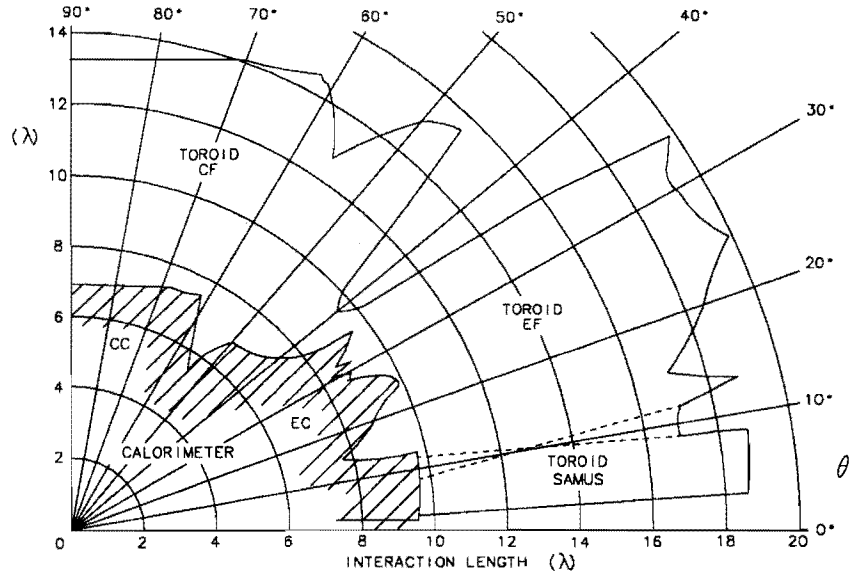

Figure 2.12. Interaction length seen by muons.

2.6.1 Muon Electronics

The muon chambers cover a large area as they are the outermost detectors. Therefore, all muon electronics before the digitizing stage are located on the chamber module itself. This includes preamplification, signal shaping, multiplexing to the digitizers, and monitoring electronics. Cathode pad signals are preamplified by a hybrid circuit charge sensitive preamplifier and then processed by a baseline subtracter (BLS). Preamplification and BLS circuits are both similar to the corresponding calorimeter circuits. A pad latch records PDT cells whose cathode pads have been struck from the pad BLS information. Anode wire signals are brought to a pair of wires which

are jumpered at the far ends of the anode wires and amplified and discriminated in a pair of hybrid circuits. The resulting output is fed to two time to voltage hybrids and two time difference to voltage hybrids. These circuits give analog information about the time and the time difference between hits (up to 2) on the wire pair. All the information is then multiplexed and sent to digitizers located in the MCH. The digitizers are 12 bit ADC circuits similar to the calorimeter digitizers.

CHAPTER 3

FROM COLLISIONS TO DATA

This chapter describes the details of selecting events observed by the D0 detector for recording, the details of recording these events, the online processing of these events and the offline processing till the reconstruction stage. The energies of electrons and hadronic jets, and missing E_t require corrections after this stage. These corrections are also described here.

3.1 Overview

The accelerator provides a $p\bar{p}$ bunch crossing every 3.5 μs (at 286 Khz) at the D0 intersection region. The D0 trigger system selects events which would be interesting and it is only these events which are recorded to tape. The trigger system comprises three levels. The first two (level 0 and level 1) are hardware triggers which bring down the event rate to $\sim$ 150 kHz and 200 Hz. The last level (level 2) is a software trigger which further brings down the event rate to 2 Hz. Figure 3.1 is a block diagram which shows the level 2 trigger and the flow of data from the detector to the VMS Host machine. The host machine then stores all data on tape for reconstruction at a later stage and sends some of the data (10%) for immediate processing. The details of processing at each stage is described below.

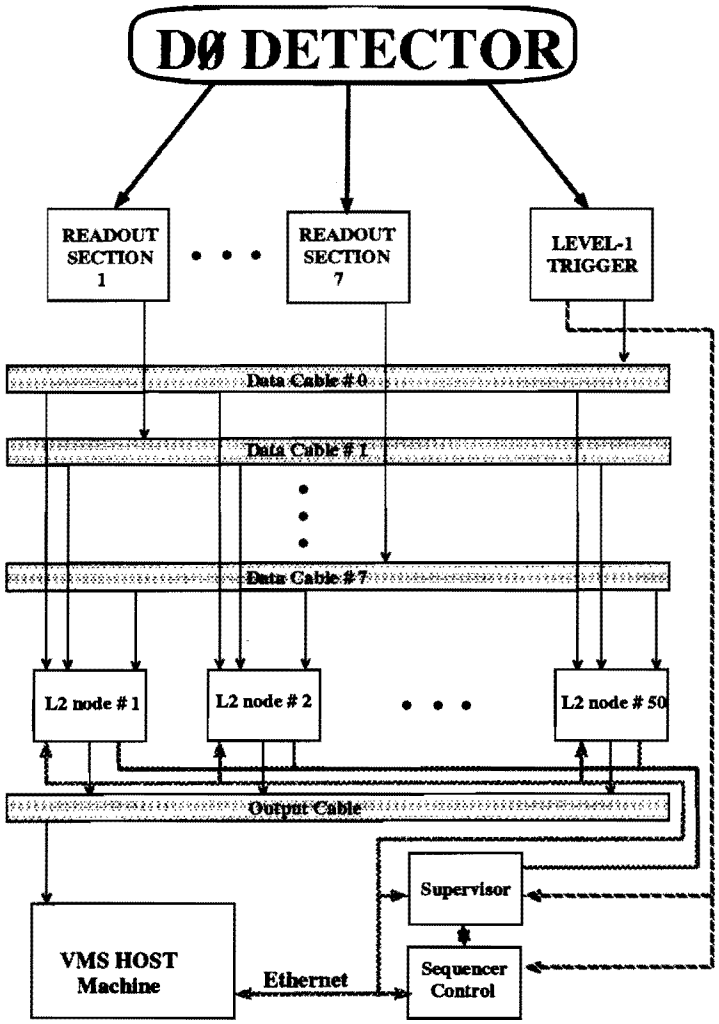

Figure 3.1. Block diagram of the data acquisition system.

3.2 *Level 0*

The Level 0 trigger is the first level of the three level trigger system used at D0. It consists of 2 sets of scintillator arrays mounted on the front surface of each endcap calorimeter. These arrays cover the region $1.9 < \eta < 2.3$ partially and the region $2.3 < \eta < 3.9$ almost completely. With this coverage, $\geq$ 99% of non-diffractive inelastic collisions are triggered by the system [18, 30]. Figure 3.2 shows the layout of a single level 0 detector.

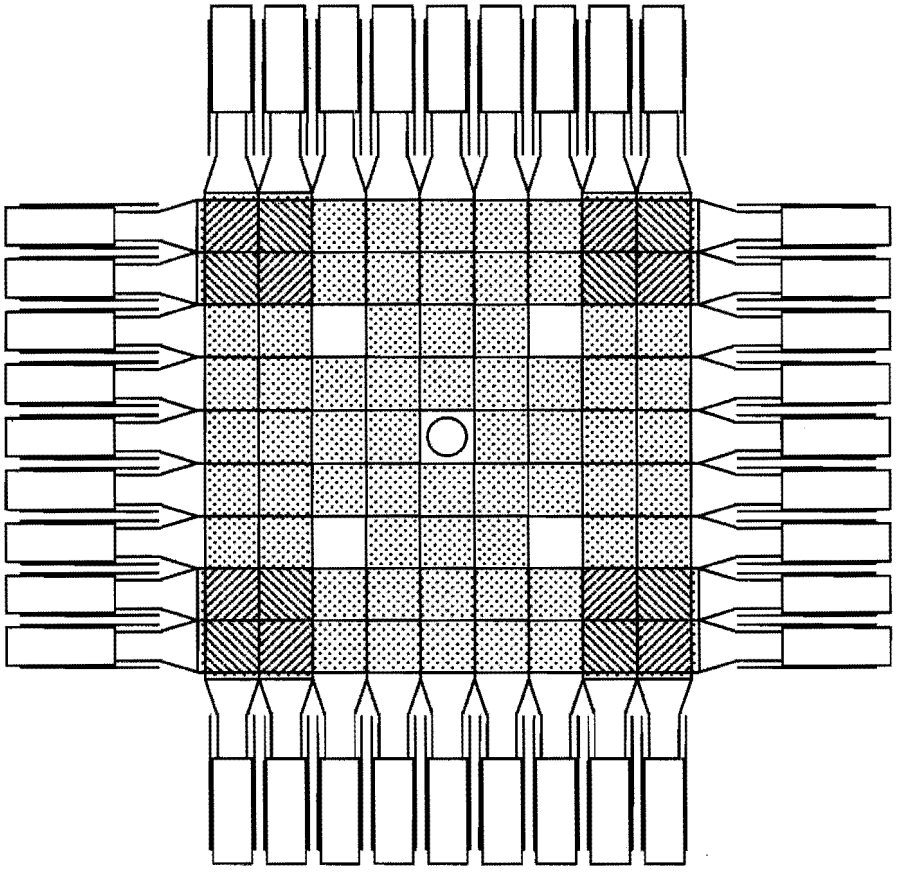

Figure 3.2. layout of scintillator arrays in a single L0 detector.

The Level 0 performs the following functions:

1. *Primary trigger function:* It indicates the occurrence of non-diffractive inelastic collisions.

2. *Calculation of z-vertex:* The z-vertex of an interaction can be calculated by measuring the time difference in the arrival of the particles from the interaction at the two level 0 detectors. Two z -vertices are calculated. One is a fast measurement which is obtained by using a GaAs digital TDC. This z vertex, called the fast z (z_f), has a resolution of 15 cm and is obtained within 800 ns of the interaction [31]. z_f is used to further eliminate beam-gas and beam-halo interactions by a vertex cut of $|z_f| < 97$ cm. It can also be used by the level 1 trigger for E_t corrections. This correction is essential because the interaction vertex spread ($\sigma_z = 30$ cm or $\sigma_t = 1$ ns) causes a significant error in the E_t calculated from the nominal vertex position. The second more accurate z-vertex is calculated by applying full calibration and time slewing corrections. This vertex called the slow z (z_s) has a resolution of 3.5 cm and is obtained within 2.1 μs of the interaction [31]. z_s is used by some level 2 triggers for E_t corrections. The standard deviation of the time difference used for z_s is used to flag multiple interactions. This can be done because beam crossings with multiple interactions have an increased spread in their arrival times (σ_t) at the level 0 detector. Thus events with $\sigma_t < 0.6$ ns are flagged 'likely single' interaction; events from this category with narrower spread ($\sigma_t < 0.4$) ns are flagged 'most likely single' interaction. Events with $\sigma_t > 0.6$ ns are broadly flagged 'likely multiple' interaction; events from this category with $\sigma_t > 1.0$ ns are flagged ' most likely multiple' interaction [31].

3. *Calculation of luminosity:* The tevatron luminosity is calculated from a knowledge of the rate of non-diffractive inelastic collisions and its cross section. The former is obtained from level 0 after applying the $|z_f| < 97cm$ cut. For the

cross section the value in reference [32] is used. The corrections for multiple interactions are also applied. The error in the luminosity is 12% and this comes mainly from the error in the cross section and the error in the efficiency of the level 0 detector (determined from Monte Carlo) [33].

3.3 *Level 1*

The level 1 trigger has the task of selecting events at a rate of 200 Hz from the non-diffractive inelastic event rate of ~150 kHz (after level 0 triggers). The decision on the selection of the events is made within the beam crossing time of 3.5 μs and is based on the information furnished by the calorimeter and muon system (in addition to the level 0 detector explained in the last section).

The Calorimeter: Information from the calorimeter comes through analog trigger pickoffs from BLS circuits. These are summed into $\Delta\eta = \Delta\phi = 0.2$ trigger towers out to $|\eta| = 4.0$. The layers of the calorimeter which contribute to the trigger, and their transverse segmentation are shown (in the regular $\Delta\eta = 0.1$ tower geometry) in figure 3.3. There are separate trigger towers for the electromagnetic (EM) and fine hadronic (FH) sections of the calorimeters (1280 of each). The signals from the trigger towers which represent the energies deposited in the corresponding trigger tower are first scaled to correspond to transverse energies and then used by the level 1 trigger to construct the following [34, 35]:

1. The transverse electromagnetic energy: $\mathrm{EMt} = \sum_{i=1}^{1280} \mathrm{EMt_i}$
2. The transverse hadronic energy: $\mathrm{Ht} = \sum_{i=1}^{1280} \mathrm{Ht_i}$
3. The total transverse energy: $\mathrm{Et} = \mathrm{EMt} + \mathrm{Ht}$
4. The missing transverse energy: $\mathrm{MPt} = \sqrt{(\mathrm{EM_x} + \mathrm{H_x})^2 + (\mathrm{EM_y} + \mathrm{H_y})^2}$ where $EM_x = \sum_{i=1}^{1280} \mathrm{EMt_{i=1}} \cos(\Phi_i)$ and $EM_y = \sum_{i=1}^{1280} \mathrm{EMt_{i=1}} \sin(\Phi_i)$ with similar formulas for H_x and H_y. The Φ_i are the azimuthal angles of the trigger towers.

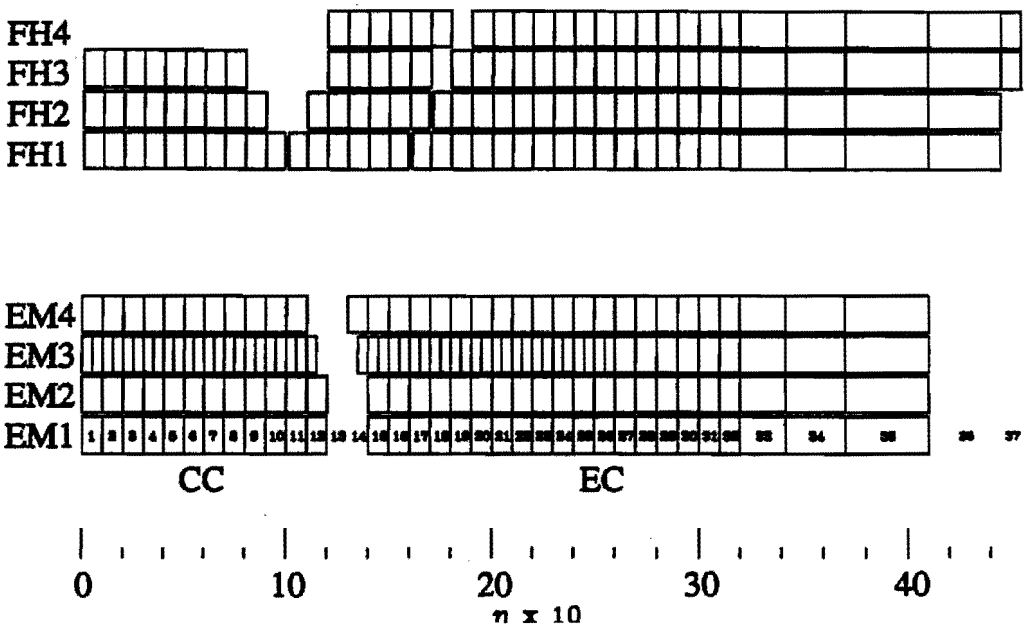

Figure 3.3. Transverse segmentation of calorimeter layers which contribute to trigger towers.

5. The energies corresponding to the transverse energies: $\mathrm{EM} = \sum_i^{1280} \frac{\mathrm{EMt_i}}{\sin(\theta_i)}$, $\mathrm{H} = \sum_i^{1280} \frac{\mathrm{Ht_i}}{\sin(\theta_i)}$ where the θ_i are the angle between the beam line and the line from the interaction vertex to the trigger towers.

The muon system: The muon system information is used by the level 1 system to obtain the number of muons in three different η regions: the 'central' ($|\eta| < 1.0$), 'end' ($1.0 < |\eta| < 1.7$), and 'SAMUS' ($|\eta| = 1.7$ to the beam pipe) [41].

The quantities above are compared with criteria which are supplied to the level 1 trigger via the trigger control computer (TCC). The decision is then made to accept the event for further processing, depending upon the combination of criteria which the event satisfied. The combinations of criteria which should pass the event for further processing is itself programmable. This programmability and the ease with which the criteria can be changed results in a very flexible level 1 system.

3.4 Level 2

This is the final level of triggering. Trigger decisions at this level are more complex as more information is available. The trigger is implemented by calling several tools. Tools are Fortran routines which make several requirements on the event and the objects (electrons, jets, muons etc.) in the event according to the parameters used in calling them. Thus calling various tools with a set of parameters defines a level 2 trigger. For any level 1 trigger passed there are a few corresponding specific level2 triggers. An event is required to pass at least one of these specific triggers to be written to tape. The six tools which were available during the run are:

1. *L2_EM:* This tool finds EM objects - electrons and photons. With this tool it is possible to require a given number of electrons/photons over a given E_t (this E_t threshold can be set different for electrons/photons in the CC and EC). The algorithm used in finding the electron/photon and some of the parameters used by the algorithms can also be specified.

2. *MUON_L2:* This tool finds muons. The parameters which can be required of the event by using this tool are: the number of muons which should pass a specified minimum P_t cut and a maximum $|\eta|$ cut.

3. *L2_JETS:* This tool finds jets. It is possible to require the event to have a given number of jets over a given E_t. Several parameters which are used in the definition of the jet can be specified. Some of them are the cone size of the jet core, total cone size of the jet, maximum and minimum transverse size of jet and the maximum and minimum electromagnetic fraction of the jet.

4. *L2_ETMISS:* This tool finds the missing E_t of the event and requires it to be over a given value.

5. *L2_ETACUT:* This tool is used to make η cuts on objects found by the other tools. The cut can be made on either physics η or detector η and is specified by giving both a maximum and minimum value (physics η is calculated using the real vertex of the event. The detector η is calculated by using the nominal collision point, which is the center of the detector as the vertex). The cut can also be made on the η gap between pairs of a given object.

6. *L2_MASSCUT:* This tool calculates the invariant mass of pairs of a given object and then makes a cut on it. Each object can also be made to satisfy η cuts.

The algorithms used by the tools to define objects are as follows:

1. *Electrons/photons:* This algorithm relies on the characteristics of shower shapes produced by electrons/photons in the calorimeter and is applied on electron/-photon candidates provided by level 1. The candidates are EM trigger towers which have an E_t above some threshold required in level 1. For each candidate the EM and FH1 (1st fine hadronic layer) energy in 3×3 readout towers around the peak EM3 (3rd EM layer) cell are unpacked and the shower centroid found. Here the peak EM3 cell is defined as the one with the largest single EM3 deposit inside the trigger tower. The E_t is then corrected for vertex position (using the slow z vertex) and leakage out of the nominal cluster size. After making an E_t cut on this corrected E_t, cuts are made on the longitudinal and transverse shower shapes, track match (for electron only), and the isolation.

   The shower shape cuts can be classified as primary and secondary as described below. The primary cuts provide most of the background rejection and are used whenever the shower shape cuts are required. The secondary cuts on the other hand are are used only when a 'tight' electron/photon definition is required. Their main purpose is to reject obviously pathological events (mainly hot cells) rather than a genuine physics background [36].

The longitudinal shape of a shower is specified by the energy deposited along the direction of motion of the particle creating the shower. Thus longitudinal shape cuts rely on variables which are a function of the total energy deposited in different calorimeter layers (4 EM and the first FH). The variables which were used are $F(i) = E(i)/\text{SUMEM}$ where $i = 1,5$. Here SUMEM is the sum of the energies of the four electromagnetic layers for $i = 1,4$, and the energy of the first fine hadronic layer for $i = 5$. $E(i)$ are the energy in the 3×3 readout towers around the readout tower containing the peak EM3 cell. The primary longitudinal shape cuts are imposed on F(5) and F(3). F(1), F(1)+F(2) and F(4) are used for making secondary longitudinal shape cuts. The above cuts depend both on energy and η. F(1)-F(4) have both upper and lower side cuts. F(5) has only an upper side cut.

The transverse shape of a shower is specified by the energy deposited in the direction perpendicular to the direction of motion of the particle creating the shower. Transverse shape cuts are therefore cuts on variables which are a function of the energy deposited in different cells of a given calorimeter layer or different towers. Most of the variables use the energy deposited in the cells of the third EM layer. The shower maximum of EM showers should most often be in this layer. This is also the reason for the finer segmentation ($\Delta\eta = \Delta\phi = 0.05$) of this layer than other layers of the calorimeter. The variables used are R5, R5-R3, E5 $\times$ 5, E3 $\times$ 3, and dE5 $\times$ 5/E3 $\times$ 3. Here Rn is the energy weighted $< r >$ of the shower in the nth layer in units of EM3 cells, E$n \times n$ is the sum of energy in $n \times n$ EM3 cell regions around the peak, and dE$n \times n$/En$'$ $\times$ n$'$ is (E$n \times n$ $-$ En$'$ $\times$ n$'$)/En$'$ $\times$ n$'$. The primary transverse shape cuts are on R5-R3 for the CC, $dE5 \times 5/E3 \times 3$ for the $|\eta| < 3.1$ region of EC, and $dE7 \times 7/E3 \times 3$ for the $|\eta| = 3.1, 3.2$ region of EC. The secondary transverse shape cuts are on $dE5 \times 5/E3 \times 3$, R5, R3 and $dE4 \times 4/E2 \times 2$ in the CC, R3 is used in EC for

$|\eta| < 3.1$ as secondary shape cut and $dE7 \times 7/E5 \times 5$ is used for $|\eta| = 3.1, 3.2$. The cuts used for transverse shape definition for various η are shown in table 3.1. When a cut is primary in an η region it is marked with 'XX', when the cut is secondary the mark is 'X'.

The electron/photon identification algorithm at level 2 is discussed in more detail in [37] and [38].

Table 3.1. Transverse shape cuts applied for various η intervals.

η tower	dE5×5/E3×3	R5-R3	R5	R3	dE4×4/E2×2	dE7×7/E5×5
1-12	X	XX	X	X	X	
13						
14-25	XX			X		
26-30	XX			X		
31-32						X

2. *Muons:* The muon algorithm at the level 2 stage is equivalent to the first two steps of the offline muon algorithm described in the next section [39].

3. *Jets:* The following algorithm is applied on jet candidates supplied by the level 1 trigger [40]. These candidates are trigger towers whose (EM+Hadronic) E_t are greater than a given threshold. The algorithm cycles through the list of candidates in descending order of E_t and for each candidate forms an E_t cluster by adding the E_t of all trigger towers whose center lie within a given radius. Other candidates included in the cluster are no longer considered candidates. An E_t weighted η and ϕ are computed and considered the η and ϕ of the jet. Finally the jet E_t and η are corrected for the event vertex after all the jets have been found.

4. *Missing E_t:* The missing E_t is defined as in the preceding section. However in level 2 the more accurate slow z vertex z_s is used to make a correction. Correction is also made by the deletion of noisy cells in the calorimeter. Noisy cells are determined by looking for the highest E_t cell in the event and checking whether it is isolated meaning it has little energy in neighbouring depth layers in the same tower.

3.5 *Triggers for events for $t\bar{t} \rightarrow ee$ Analysis*

The information available at each trigger stage and the tools available for the construction of a trigger have been described in the previous sections. The trigger for the selection of events for $t\bar{t} \rightarrow ee$ analysis was designed to accept top events decaying to the dielectron channel (signal) with high efficiency and to reject the overwhelming QCD dijet background. A brief description of the study leading to the final trigger used is given below. The study was performed using the trigger simulator [44, 45] which simulated both level 1 and level 2 triggers offline. ISAJET [46] Monte Carlo samples of events corresponding to various values of the top mass were first passed through the D0 detector simulation package D0GEANT [47, 48] and then processed by the trigger simulator in order to obtain the trigger efficiency for the signal. Dijet QCD Monte Carlo events were passed through the simulation packages to obtain the anticipated background rate for the triggers. For the signal top Monte Carlo samples for top mass m_t = 80, 100, 120, 140, 160 and 180 GeV were studied. As an illustration results are presented here for m_t = 100 and 120 GeV only. For these masses the estimated [17] cross section for production of $t\bar{t}$ events is 103 and 39 pb respectively. This corresponds to a cross section of $\sim$ 1.3 and $\sim$ 0.5 pb respectively for the $t\bar{t} \rightarrow ee$ channel. This is in contrast to the cross section for QCD dijet events whose cross section is of the order of $\sim$ 100 μb.

Events in the $t\bar{t} \rightarrow ee$ decay channel have 2 well isolated high E_t electrons, jets

from the b quarks and missing E_t. Three different triggers are involved in collecting these and were used as logical OR for data acquisition: (1) Trigger ELE_HIGH which requires events to be associated with at least 1 high E_t electron, (2) Trigger ELE_2_HIGH which requires the presence of at least 2 high E_t electrons, and (3) Trigger ELE_JET which requires at least 1 high E_t electron, at least 2 energetic jets and substantial missing energy $\not\!\!E_t$. A detailed study of the efficiency for detecting top events and the suppression rate of background events has been made to determine the parameters (e.g. thresholds for electron or jet E_t) for each of these triggers [41]. General features of these triggers are discussed below:

ELE_HIGH Trigger — This trigger requires at least 1 electron at both level 1 and level 2 stages. As discussed in previous sections, level 1 electrons are defined solely by the amount of energy deposited in EM towers; level 2 electrons undergo additional tests on the shape of the shower. The role of these triggers in event selection is presented here by requiring electrons at level 1 only, and then at both level 1 and level 2 trigger. The level 1 efficiency for Monte Carlo top events of mass 120 and 100 GeV as a function of the trigger tower level 1 E_t threshold energy is shown in figure 3.4a and 3.4b respectively. The QCD dijet rate after level 1 is shown in 3.4c. These figures show that a choice of an E_t threshold of 12 GeV (for example) will have high efficiency for detecting top events and the QCD dijet rate is also seen to go down to ~ 10 μb.

We now choose 12 GeV as the threshold E_t (level 1) and impose level 2 electron trigger. Figure 3.5 shows signal efficiencies and dijet rates as a function of the E_t threshold of the required electron at level 2. It is seen that a threshold E_t value of as high as 20 GeV can be chosen to keep very high signal efficiency. Under this condition, the dijet rate goes down to ~ 0.5 μb. Although this trigger is not desirable since the signal to noise ratio, S/N is rather poor, this trigger was used for the analysis in combination (logical OR with other triggers) with other triggers (described below) in

order to improve acceptance for the $t\bar{t} \rightarrow ee$ events. It should be noted that the offline analysis (to be described in the next chapter) of these triggered events improve the S/N ratio. The trigger conditions of ELE_HIGH trigger is symbolically expressed as EM(1,12) + L2EM(1,20), where EM(1,12) stands for at least 1 electron with $E_t > 12$ GeV in level 1 and L2EM(1,20) stands for at least 1 electron with $E_t > 20$ GeV at level 2.

ELE_2_HIGH Trigger — This trigger requires at least 2 electrons at both level 1 and level 2. The efficiency for the signal and the rate of QCD events as a function of level 1 threshold E_t values of electrons are shown in figure 3.6a, 3.6b, and 3.6c. In this figure, level 2 electrons are not subjected to any threshold condition. Figures 3.6a and b show that the level 1 electron E_t threshold should be chosen to be around 6 GeV to retain high efficiency. Imposing level 1 E_t threshold for both electrons at 6 GeV, the signal efficiency and background rate as a function of level 2 E_t threshold are shown in figure 3.7. Typically, a value of 12 GeV for the level 2 electrons is used for this trigger. Under this condition the background QCD dijet event rate corresponds to a cross section of ~ 0.08 μb. This trigger thus has a better S/N ratio (than ELE_HIGH) with a signal efficiency of $\sim 60\%$. This trigger is symbolically written as EM(2,6) + L2EM(2,12).

ELE_JET Trigger — This trigger requires simultaneous presence of at least 1 high E_t electron, at least 2 narrow jets and substantial missing E_t in the events. As mentioned earlier, various level 2 tools are utilized to define objects as electron, jets, muon etc.. Using L2_EM (electron identification) and L2_JETS tool, this trigger demands at least 1 electron and at least 2 narrow jets of cone size 0.3. An additional requirement of missing E_t from the L2MS tool is also required. Almost all electrons identified by the L2_EM tool are also identified as jets by the L2_JETS tool. Hence, an electron is counted twice — as an electron as well as a jet.

Essentially this trigger is made out of three logical coincidences: level 1 object

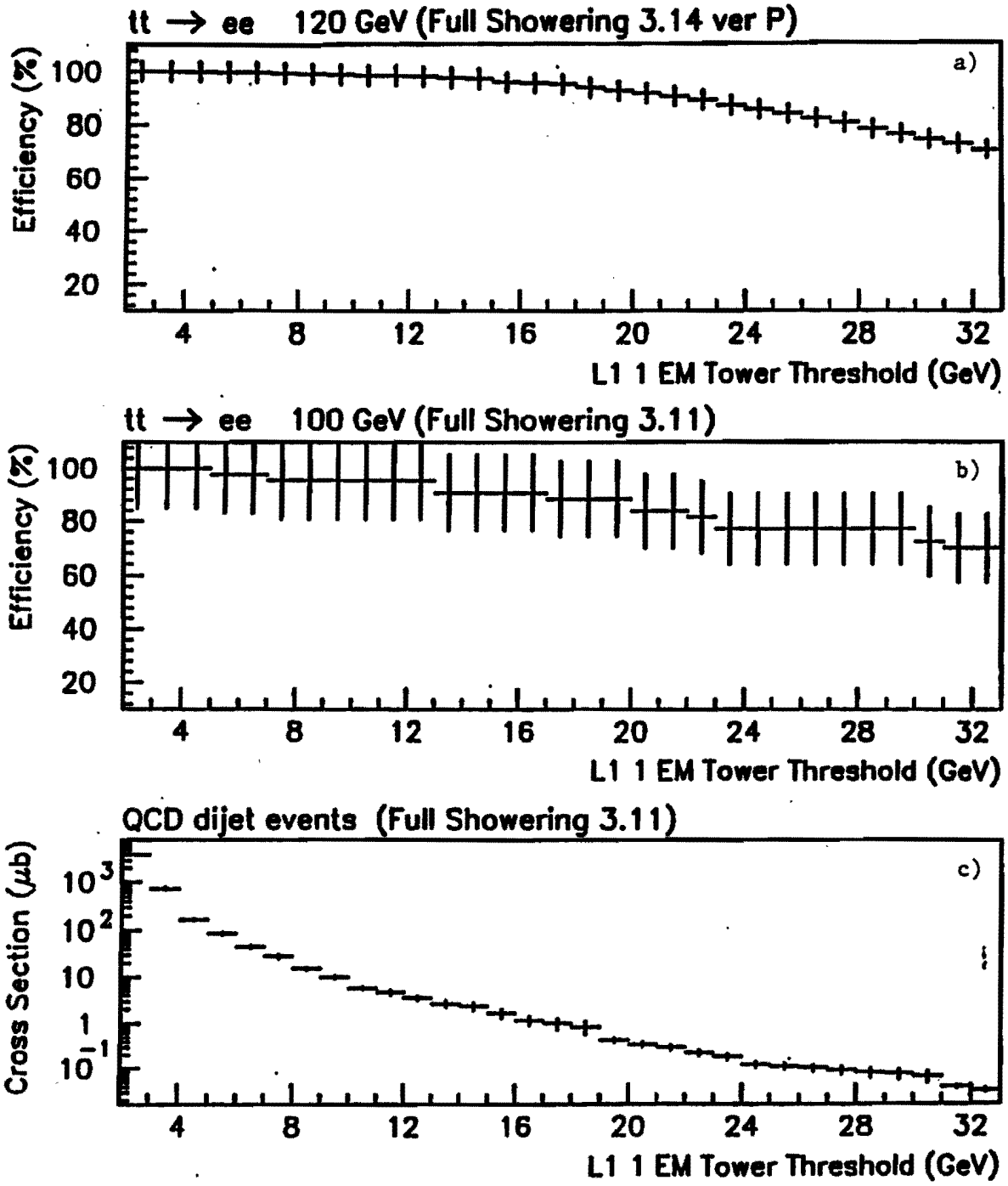

Figure 3.4. Level 1 trigger efficiency vs. P_t required on 1 EM tower for a) Top MC with $m_t = 120$ GeV b) Top MC with $m_t = 100$ GeV and c) Integrated QCD cross section vs. P_t required on 1 EM tower. background.

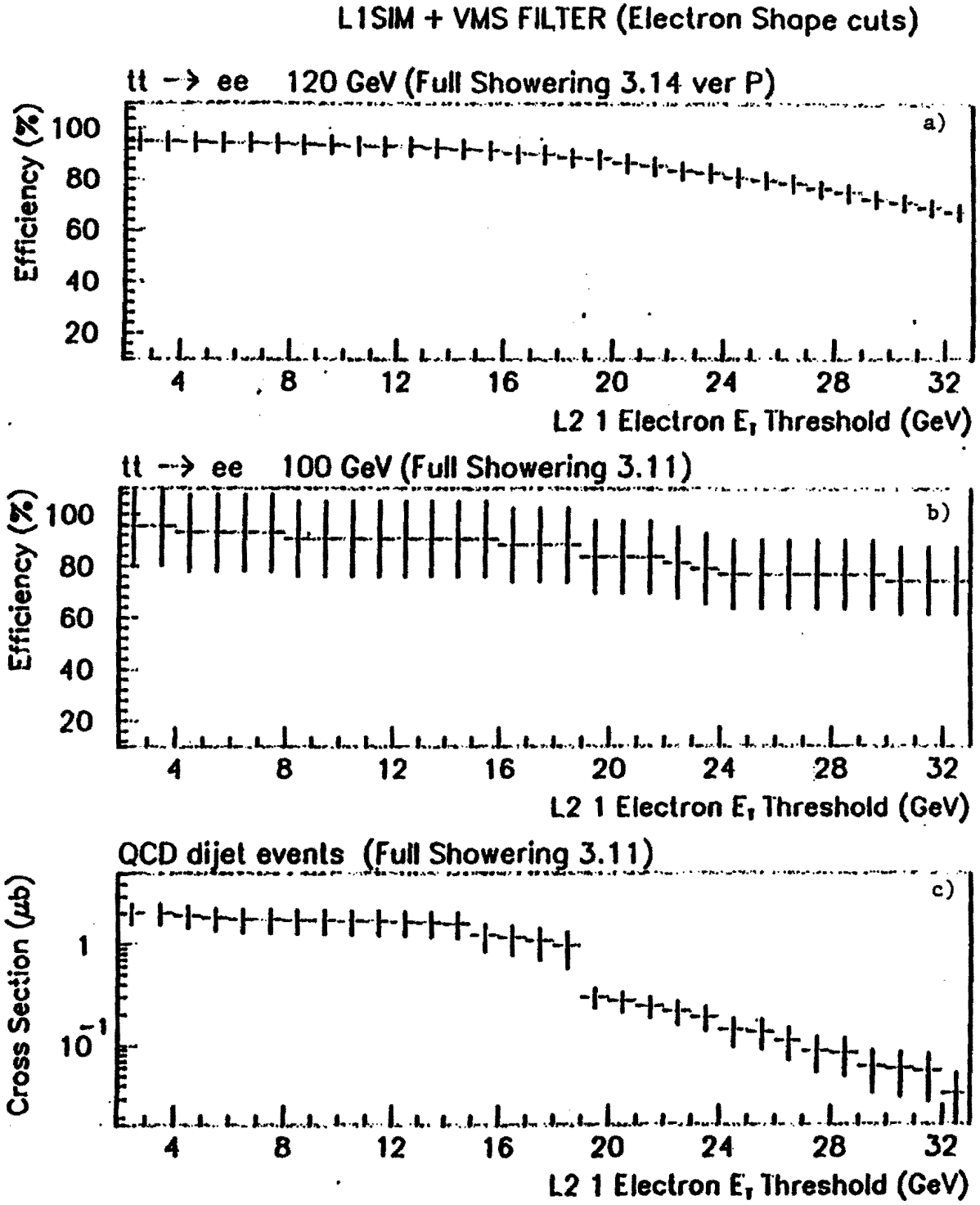

Figure 3.5. Level 2 trigger efficiency vs. P_t requirement on 1 level 2 EM object a) Top MC with $m_t = 120$ GeV b) Top MC with $m_t = 100$ GeV and c) Integrated QCD cross section vs. P_t. Level 1 requirement for all three plots: 1 EM tower > 12 GeV.

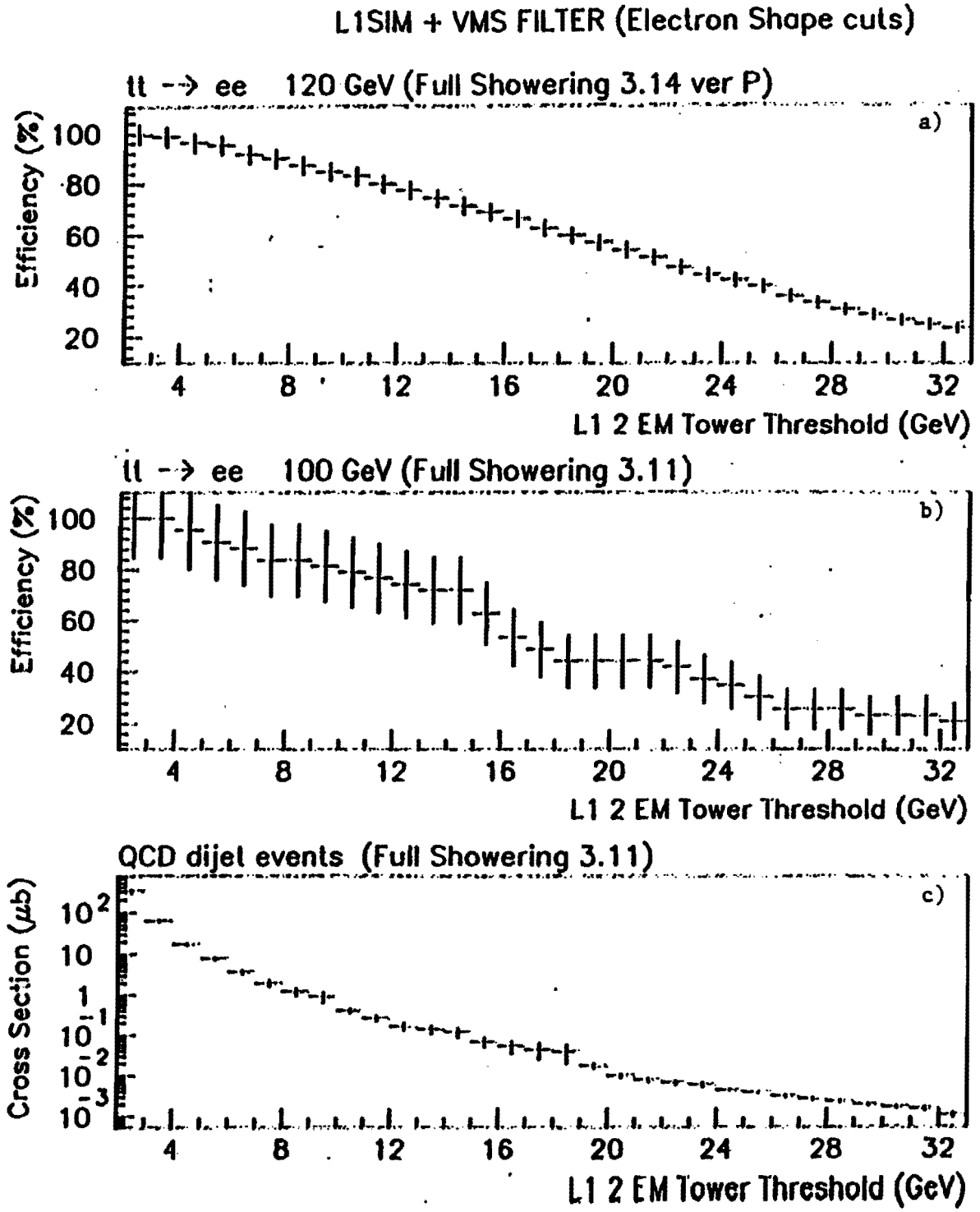

Figure 3.6. Level 1 trigger efficiency vs. P_t required on each of 2 EM tower for a) Top MC with $m_t = 120$ GeV b) Top MC with $m_t = 100$ GeV and c) Integrated QCD cross section vs. P_t per EM tower.

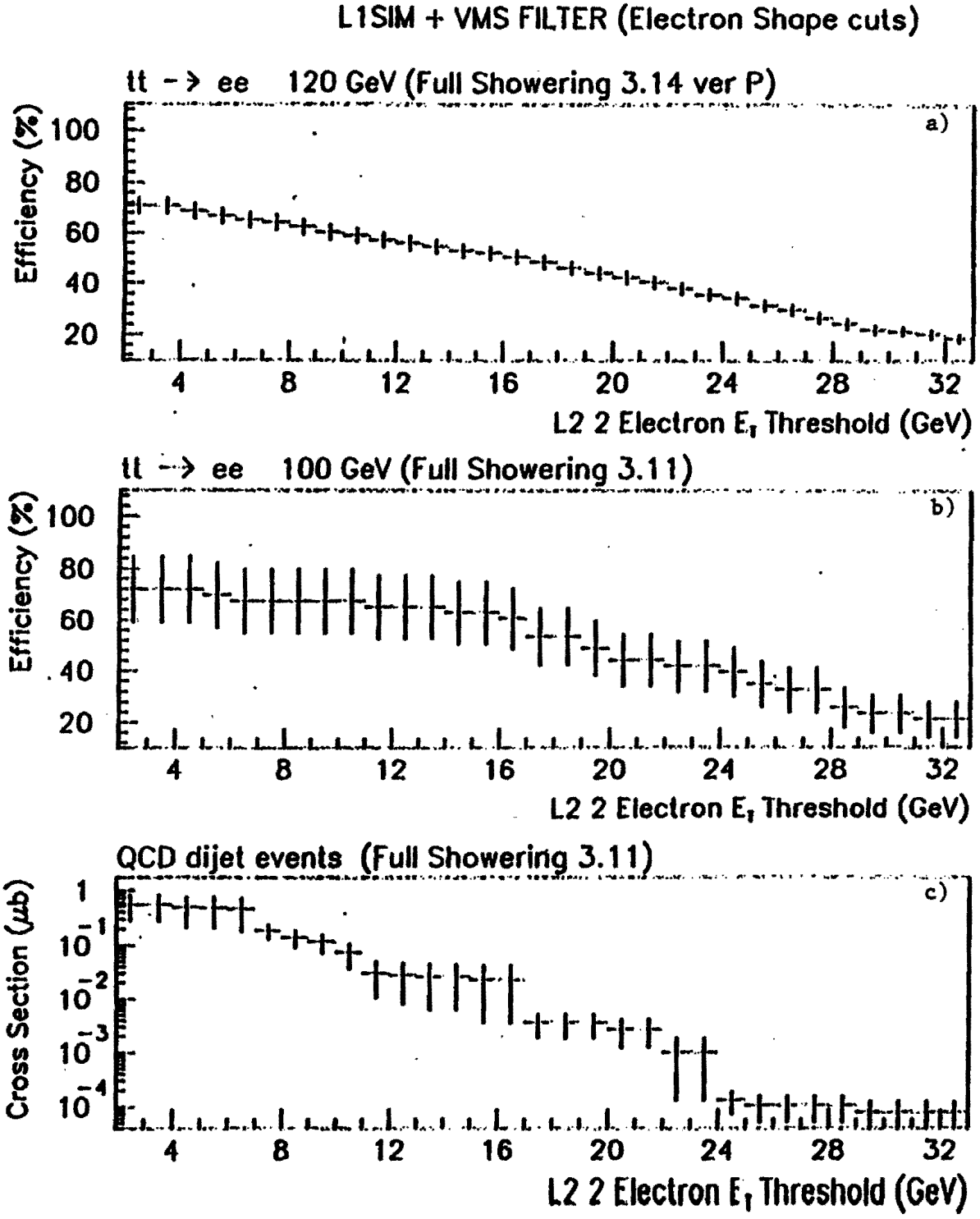

Figure 3.7. Level 2 trigger efficiency vs. P_t required on each of 2 level 2 EM objects. a) Top MC with $m_t = 120$ GeV b) Top MC with $m_t = 100$ GeV and c) Integrated QCD cross section vs. P_t per EM object. Level 1 requirement for all three plots: 2 EM towers > 6 GeV.

definition, level 2 object definition and imposition of missing E_t. The variation of signal efficiency and QCD background as these conditions are applied to the trigger is discussed below.

If only the level 1 condition EM(1,12) + JT(2,5) is applied (i.e at least one electron with $E_t > 12$ GeV, plus at least 2 jets with $E_t > 5$ GeV), then the triggered events correspond to a cross section of 2.1 ± 0.4 μb for QCD dijet events and signal events have high efficiency as presented in Table 3.2. In the next step we consider that the electron be identified by level 2 trigger and that the event be associated with missing E_t. In figure 3.8, signal efficiencies and background event rate are shown as a function of level 2 P_t values of jets when the trigger condition is EM(1,12) + JT(2,5) + L2EM(1,12) + L2MS(10). We see that the level 2 P_t threshold of 10 GeV corresponds to a dijet cross section of 0.1 μb. This is also the value of level 2 jet P_t after which the efficiency of the trigger for $m_t = 120$ GeV starts going down from a value of $\sim$ 89%. The same plots for the trigger condition EM(1,12) + JT(2,5) + L2EM(1,12) + L2MS(20) show similar characteristics (figure 3.9), however the background is smaller at $\sim$ 9 pb and the efficiency lower at $\sim$ 79% ($m_t = 120$ GeV) for a level 2 jet P_t threshold of 16 GeV. The former values of the threshold were preferred in view of the higher efficiencies for the ELE_JET trigger.

The ELE_JET trigger when combined with ELE_HIGH and ELE_2_HIGH (logical OR of three of them) gives an efficiency of 91% for a top mass of 120 GeV. Event reconstruction is done offline on all the events which pass the trigger. The algorithms used in the definitions of objects are different as they need not be as fast as the level 2 algorithms, which are used online where speed is crucial. The offline reconstruction is described in the next section.

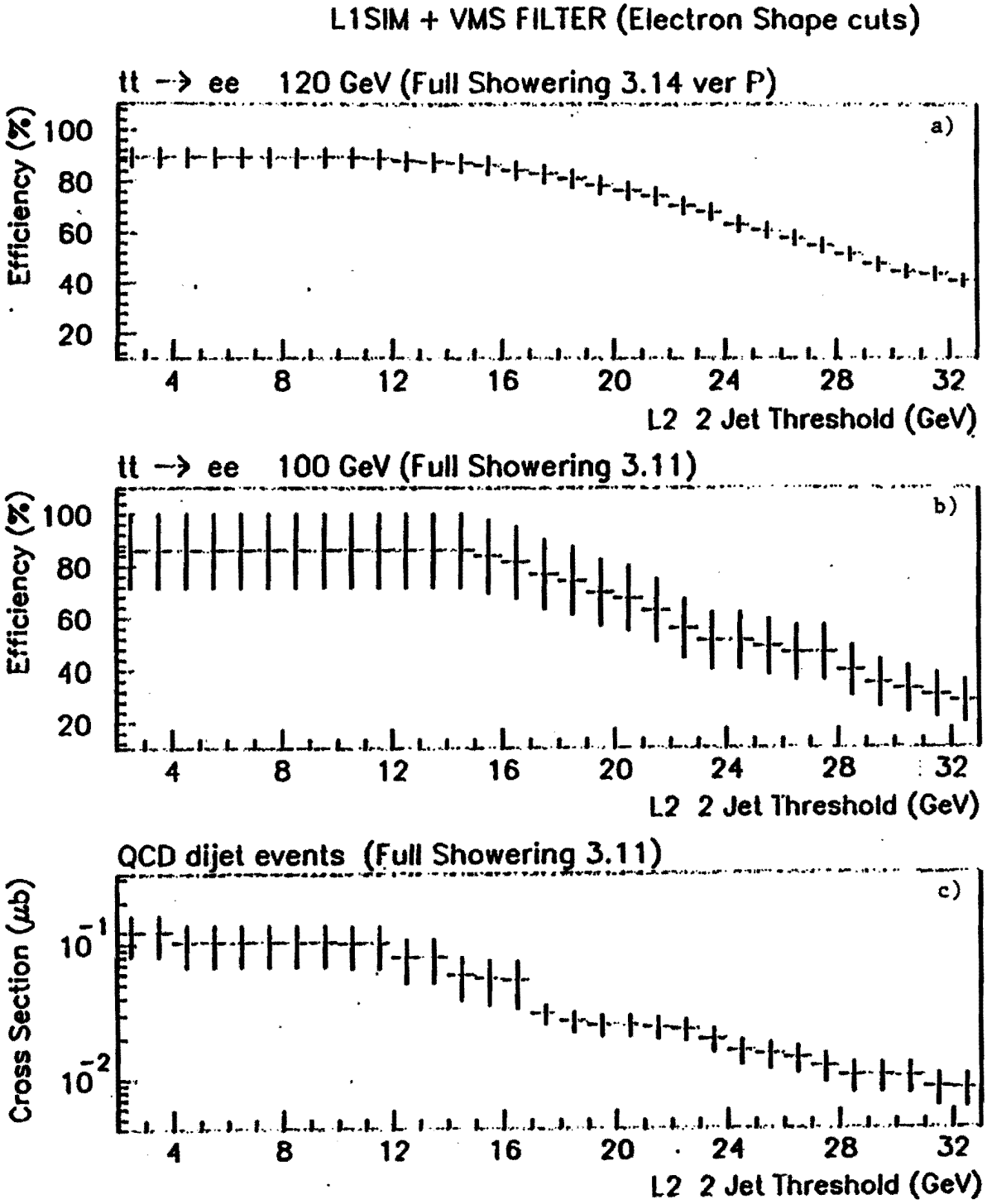

Figure 3.8. Level 2 trigger efficiency vs. P_t required on each of 2 jets in Level 2 for a) Top MC with $m_t = 120$ GeV b) Top MC with $m_t = 100$ GeV and c) Integrated QCD cross section vs. P_t per jet. Other requirement on all three plots: Level 1 — 1 EM tower > 12 GeV and 2 hadronic towers > 5 Gev. Level 2 — 1 EM object > 12 GeV and $\not\!\!E_t$ > 10 GeV.

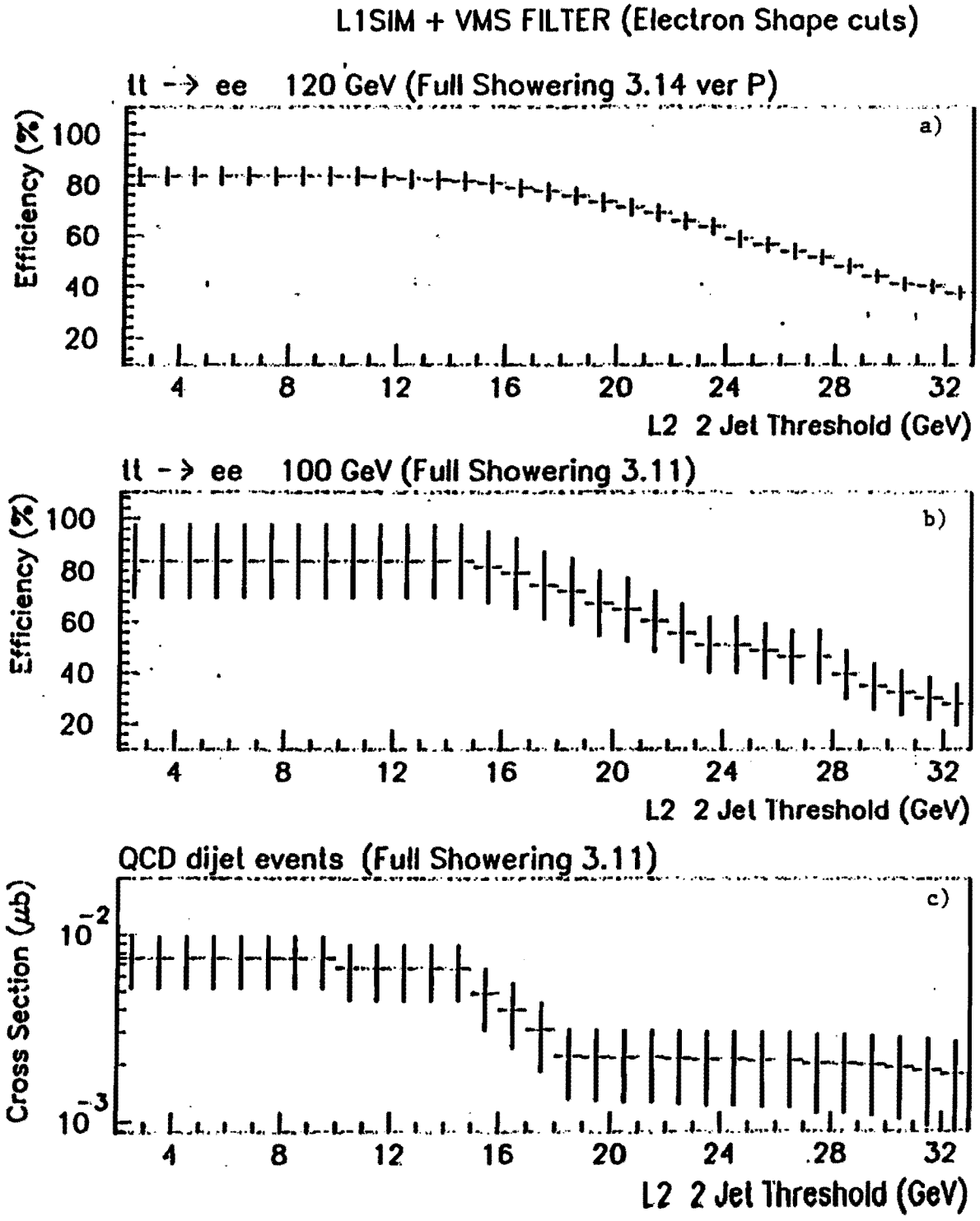

Figure 3.9. Level 2 trigger efficiency vs. P_t required on each of 2 jets in Level 2 for a) Top MC with $m_t = 120$ GeV b) Top MC with $m_t = 100$ GeV and c) Integrated QCD cross section vs. P_t per jet. Other requirement on all three plots: Level 1 — 1 EM tower > 12 GeV and 2 hadronic towers > 5 Gev. Level 2 — 1 EM object > 12 GeV and $\not\!\!E_t$ > 20 GeV.

Table 3.2. Trigger efficiencies and QCD di-jet rates.

Trigger condition	efficiency(%)		QCD di-jet cross section
	m_t=120 GeV	m_t=100 GeV	
1) EM(1,12)+JT(2,5)	100±19	93±15	2.1±0.4 μb
2) EM(1,12)+JT(2,5)+ L2EM(1,12)+L2JET(2,10) +L2MS(10)	89±4	86±14	0.10±0.03 μb
3) EM(1,12)+JT(2,5)+ L2EM(1,12)+L2JET(2,16) +L2MS(20)	79±3	79±13	4.0±0.1 pb

3.6 Event Reconstruction

Event reconstruction is done by a software package named D0RECO. This package identifies various physics objects present in the event from the information in the raw data and gives two output files called the DST and the STA. The STA has the raw data information as well as detailed information on the reconstructed objects whereas the DST has information only about the reconstructed objects. This makes the DST 10 times smaller than STAs which are typically 600 Kbytes for a single event. This makes it possible to keep the DST on disk for easy access during further analysis.

The processing of the data is common for all physics analyses till the DST, STA stage. These files are processed by the various physics groups in different ways depending upon their physics goals. Each group may even find it necessary to define the physics objects differently. This requires the D0RECO definition of objects to be loose enough so that further analyses may arrive at their lists of physics objects by making cuts rather than starting all over again from raw data. The algorithms used for finding the various physics objects are given below.

3.6.1 *Jet Identification*

Jets can be defined by several algorithms. Two types of algorithms used in D0 are the nearest neighbor algorithm and the cone algorithm ([42, 43] describe the motivation for this algorithm) with various values of R, where $R = \sqrt{(\delta\eta)^2 + (\delta\phi)^2}$ is the radius of the cone in η, ϕ space. For the $t\bar{t} \rightarrow ee$ analysis the cone algorithm with a radius of 0.5 is used. The nearest neighbour algorithm is described in the subsection on electron identification. Here we describe the cone algorithm [49].

Calorimeter towers with a minimum E_t of 1 GeV are ordered in E_t and starting from the highest E_t tower preclusters are formed by including contiguous cells out to a radius of 0.3 (in η, ϕ space). These contiguous cells should have an E_t of at least 1 GeV to be included in the precluster. The formation of preclusters cuts down on the number of towers which can be considered a possible starting point for jet formation. The center of the precluster is considered the center of the cone jet. All towers within a radius of R from the center are included in the jet and a new E_t weighted center is calculated. This procedure of finding the new center is repeated until the jet center is stable. When jets share energy they are combined or split depending upon the fraction of energy shared relative to the lower jet E_t. If the fraction is less than 0.5 they are split, otherwise they are combined. When the jets are split the energy of a cell in the overlap region is assigned to the jet whose axis is closest to the cell. Finally an E_t cut of 8 GeV is imposed on all jets.

3.6.2 *Electron Identification*

Electrons are identified by looking for electromagnetic clusters (EM) which have an associated track in the central tracker. Cuts are then made on cluster, track characteristics and the match between the cluster and the track.

The procedure starts by the formation of EM clusters by using the nearest neighbor

algorithm. EM calorimeter towers (4 EM layers and first layer of fine hadronic) are ordered in E_t. Clusters are then formed by looping over all towers and looking for neighboring towers with highest E_t above 50 MeV and linking neighboring towers. A minimum E_t cut of 1.5 GeV is then applied on the clusters. Once the EM clusters are formed, cuts are made on the following characteristics.

EM fraction: This is a very powerful cut which provides good discrimination against charged hadrons. The EM fraction is defined as

$$\frac{\text{Energy in layers EM1 + EM2 + EM3 + EM4}}{\text{Energy in layers EM1 + EM2 + EM3 + EM4 + Hadronic}}$$

and it is required that it be $\geq 90\%$. The cut has an efficiency of $\sim 99\%$. Figure 3.10 has a plot of the EM fraction distribution for electron candidates from $Z \rightarrow ee$ data events. It can be seen that the distribution should have a very small tail for EM fraction $< 90\%$.

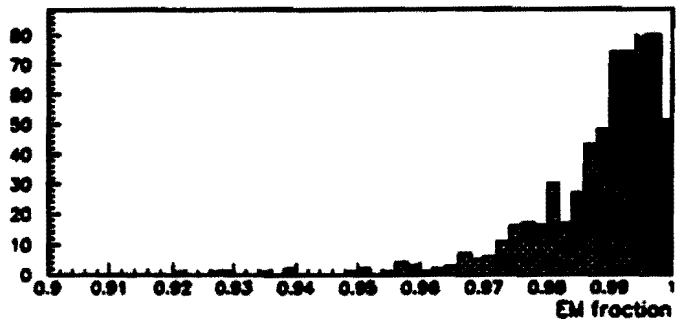

Figure 3.10. EM fraction distribution for electron candidates from $Z \rightarrow ee$ events.

Cluster shape: The cluster shape of electron clusters was studied in the test beam and in the Monte Carlo. There was good agreement between the two. For making shape cuts on the EM clusters for EID the Monte Carlo is taken as reference.

The shower shape can be characterised by the fraction of energy in each layer

of the calorimeter. However these fractions are not independent of each other. The covariance matrix method described here takes into account the energy fractions and their correlation.

A covariance matrix M for each of 37 η towers is computed from a reference sample of N Monte Carlo electrons with energies ranging from 10 GeV to 150 GeV. The matrix elements M_{ij} are defined as

$$M_{ij} = \sum_{n=1}^{N} (x_i^n - \overline{x_i})(x_j^n - \overline{x_i})$$

where x_i^n is the value of the i^{th} variable for the n^{th} electron and $\overline{x_i}$ is the mean of the i^{th} variable. The 41 variables used are the fractional energies in layers 1,2,4 of the EM calorimeter, the fractional energy in each cell of a 6×6 array of cells in layer 3 centered on the most energetic tower in the EM cluster, the logarithm of the cluster energy and the z position of the event vertex.

Using this matrix the covariance parameter

$$\chi^2 = \sum_{ij} (x_i - \overline{x_i}) H_{ij} (x_j - \overline{x_i})$$

can be used as a measure of the consistency of the shape of any data shower with respect to the shower shape of the N Monte Carlo electrons. Here $H = M^{-1}$ and x_i are the 41 variables used to characterize the shower.

In general, the values of the variables x_i are not normally distributed and therefore the covariance parameter χ^2 does not follow a normal distribution. H is a symmetric matrix and can be diagnolized using an appropriate unitary matrix U. The χ^2 is then

given by

$$\chi^2 = yHy^T$$

so that the transformed matrix $H' = U^T HU$ and the components of the vector y are uncorrelated variables. Components of y which dominate the value of χ^2 can now be limited to a maximum value which will maximize the electron finding efficiency and rejection power.

The distribution of χ^2 for electron candidates from $Z \rightarrow ee$ decays and inclusive jet data is shown in figure 3.11.

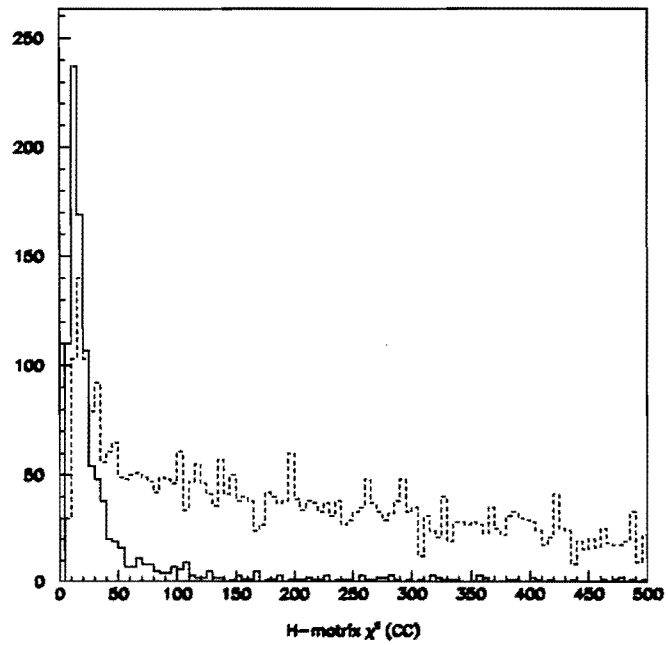

Figure 3.11. χ^2 distribution for electron candidates from $Z \rightarrow ee$ decays (solid line) and inclusive jet data (dashed line).

Cluster - Track match: A track in the central tracker pointing to the EM cluster is required for EID. This discriminates against photons which are produced from the decay of π^0 and η mesons which are copiously produced in $p\overline{p}$ collisions. A

logarithmically weighted shower centroid is defined for this purpose as follows:

$$x_{cog} = \frac{\sum_i w_i x_i}{\sum_i w_i}$$

where the weights w_i are defined as

$$w_i = max\left(0, w_0 + \ln\left(\frac{E_i}{E}\right)\right)$$

where E_i is the energy in the i_{th} cell, E the energy of the cluster, and w_0 a parameter chosen to optimize the position resolution. The log weighted centroid is used because of the exponential lateral development profile of an electromagnetic shower. The position resolution is 1.5 to 2.0 mm as determined by measurements from a test electron beam. The significance of the track match between a reconstructed track and an EM cluster is then defined as

$$S_{CC} = \sqrt{\left(\frac{\Delta\phi}{\delta_{\Delta\phi}}\right)^2 + \left(\frac{\Delta z}{\delta_{\Delta z}}\right)^2}$$

in the CC and

$$S_{EC} = \sqrt{\left(\frac{\Delta\phi}{\delta_{\Delta\phi}}\right)^2 + \left(\frac{\Delta R}{\delta_{\Delta R}}\right)^2}$$

in the EC. Here $\Delta\phi$ is the azimuthal mismatch, Δz the mismatch in z and ΔR the mismatch transverse to the beam. δ_x is the resolution for observable x. The distribution of the track match significance variable S is shown in figure 3.12 for electron candidates from $Z \rightarrow ee$ decays and inclusive jet data.

Track - Ionization: Photon conversions in the material in front of the tracking

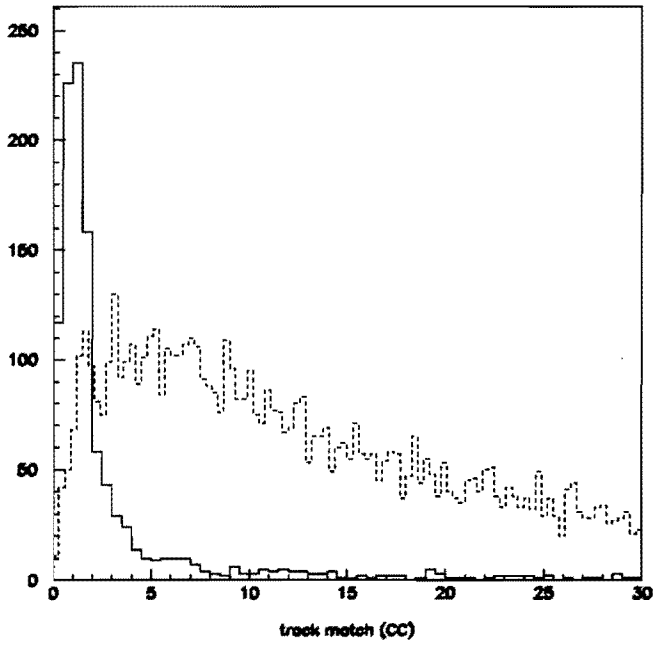

Figure 3.12. Track match significance(S) distribution for electron candidates from $Z \rightarrow ee$ decays (solid line) and inclusive jet data (dashed line).

chambers produce e^+e^- pairs. The tracks of the two particles are very close because of the absence of a magnetic field in the tracking region and are very often reconstructed as a single track. However the ionization for the e^+e^- pairs should be twice that for an electron. The ionization per unit length (dE/dx) is shown in figure 3.13 for reconstructed single tracks from inclusive jet data. The two peaks from single tracks and e^+e^- pairs can be seen. Cutting on dE/dx is thus useful in reducing the background from these conversions.

Isolation: The isolation variable for an EM cluster is defined as:

$$f_{iso} = \frac{E(0.4) - EM(0.2)}{EM(0.2)}$$

where $E(0.4)$ is the energy deposited in the cone $R < 0.4$, $R = \sqrt{\Delta\phi^2 + \Delta\eta^2}$ around the electron direction and $EM(0.2)$ the EM energy in the cone $R < 0.2$. This variable

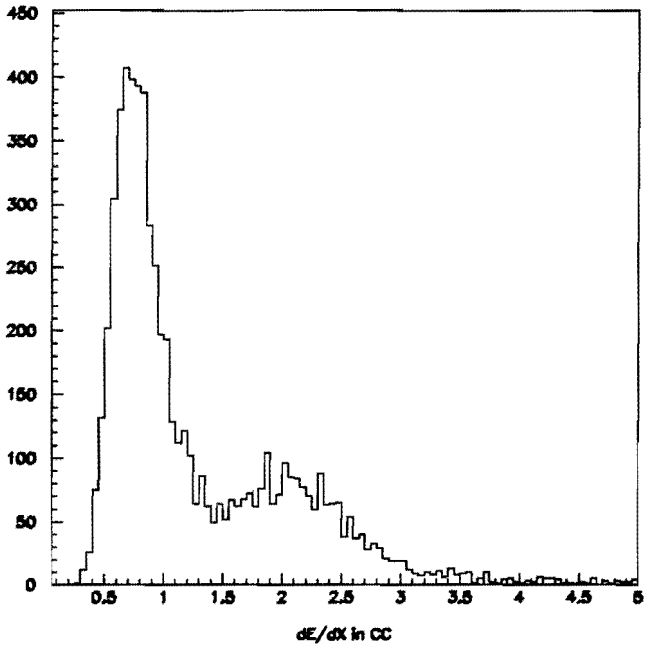

Figure 3.13. dE/dx distribution for electron candidates from inclusive jet data.

is good for making cuts on electrons/photons in processes where they are expected to be isolated. Figure 3.14 has a plot of f_{iso} for electron candidates from $Z \rightarrow ee$ decays where the electrons are expected to be isolated and for electron candidates in an inclusive jet sample where electrons are not expected to be isolated.

3.6.3 Muon Identification

The detection of muons proceed through three distinct steps [39]. In the first step the algorithm loops through the raw data to determine the location of hits in specific muon chambers. This location is then transformed into hits in the D0 global coordinate system using survey information and chamber geometry. In the second step a pattern recognition algorithm finds groups of hits which could possibly be from a muon. A preliminary fit is then made using these hits. The muon momentum is then corrected for energy loss in the calorimeter and the iron toroid. This correction is determined from a Monte Carlo study which yielded the average energy loss of muons for a given

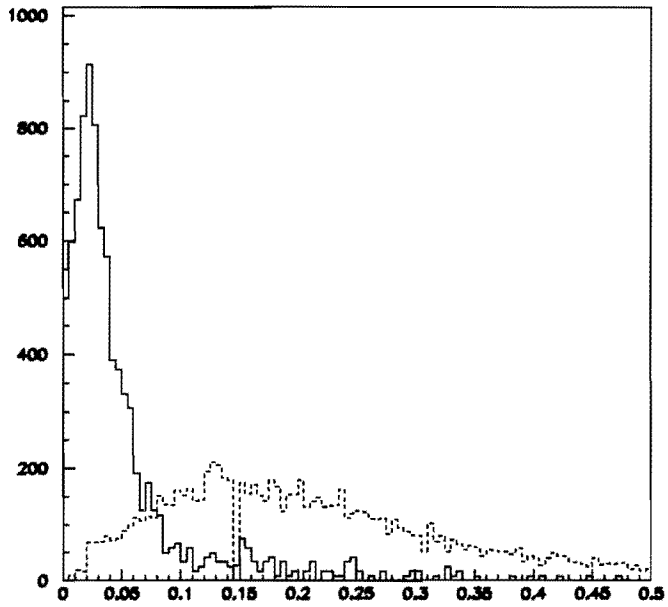

Figure 3.14. Isolation distribution for electron candidates from $Z \rightarrow ee$ decays (solid line) and inclusive jet data (dashed line).

path in the detector. In the final step a global fit is made using information from the calorimeter and the central tracker.

3.6.4 Missing E_t

The vector sum of the P_t of all particles produced in any event should be equal to zero. Therefore the P_t of particles not detected by the detector should be equal and opposite to the vector sum of the P_t of all other particles in the event. This is the only quantity which signals the presence of particles like neutrinos which are not detected by the D0 detector. Since only the energy of all particles (except muons) is measured by the D0 detector the corresponding E_t is used and is termed the missing E_t of the event.

When the event does not have any muons (which do not deposit all their energy in the calorimeter) the missing E_t obtained from just the calorimeter information is

a good measure of the true missing E_t. However when there are muons present in the event the E_t information from the muon system has to be included to obtain the missing E_t. The latter will be referred to as the muon corrected missing $E_t(\not\!\!E_t^{\mu})$. The former will be referred to as the missing E_t ($\not\!\!E_t$) and will be used in the $t\bar{t} \rightarrow ee$ analysis. The formula used for calculating $\not\!\!E_t$ is [50]

$$\begin{aligned} \not\!\!E_t &= \sqrt{E_x^2 + E_y^2} \\ E_x &= -\sum_i E_i \sin(\theta_i)\cos(\phi_i) \\ E_y &= -\sum_i E_i \sin(\theta_i)\sin(\phi_i) \end{aligned}$$

Here i runs over all n cells in the calorimeter. E_i is the energy deposited in cell i and θ_i and ϕ_i are the polar and azimuthal angles respectively of the center of cell i from the vertex of the event.

3.7 Corrections

Several corrections have to be applied to the energy of the physics objects given by D0RECO. This is because the D0 calorimeter energy scale and the algorithms to implement the energy scale on some objects were finalized during/after the run and hence could not be included in D0RECO. The EM energy scale is obtained from the nominal test beam response and is fine tuned in such a way that the Z mass obtained by the reconstruction of $Z \rightarrow ee$ decays equals the value measured at LEP. This response is different for the three parts of the calorimeter and the hence the above procedure is carried out for each one of them by requiring that both the electrons from the Z, decay into the same part of the calorimeter (CC, ECN and ECS). More details about the correction can be found in [51].

The correction for jet energies is more complicated. Jets are composed of several

particles, most of them at low momenta. Therefore the non linear response, especially at low momenta, and the response variations of the detector due to poorly instrumented regions make it necessary to correct jet energies [52]. Other effects for which jet energy corrections are required are the shift in energy due to the combination of zero suppression and asymmetric pedestal distributions, the contribution to the jet energy from the underlying event, and the energy deposition outside the cone by particles which are within the jet cone [52]. The corrections are first carried out for jets in the central region($|\eta| < 0.7$) and then transferred to the forward region.

The energy response in the central region is obtained by a variation of the missing transverse energy projection fraction (MPF) method [53, 54]. In this method the EM energy scale is used as the reference. A sample of events which have a good EM cluster and a jet in the central region are used. In such events the missing E_t component in the direction of the transverse energy of the EM cluster should ideally be zero. It is not so in practice and the value is assumed to be due to the jet response. This quantity is called the MPF [55]:

$$\mathrm{MPF} = \frac{\vec{\not{E}}_t \cdot \hat{n}_t^{\gamma}}{E_t^{\gamma}}$$

where $\hat{n}_t^{\gamma}$ is the unit vector in the azimuthal direction of the photon, E_t^{γ}. The jet response R_j is then given by $R_j = 1 + \mathrm{MPF}$.

The correction for the effect due to zero suppression and uranium noise is determined from data which was taken without zero suppression. The correction for the underlying event is assumed to be equal to the contribution measured in minimum bias events. The correction for out of cone showering was determined to be about 4% from test beam showers [52]. The correction factor which includes the contribution of all the correction factors described above is shown in figure 3.15 for 0.5 cone jets as a function of jet transverse energy for two values of η.

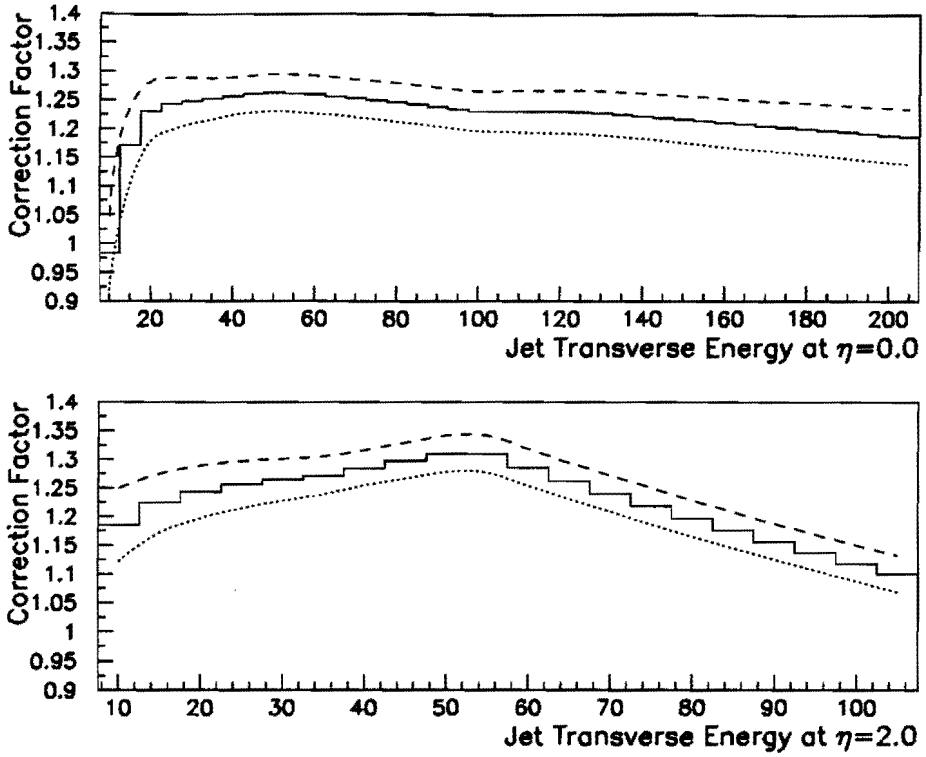

Figure 3.15. Correction factor for 0.5 cone jets. The solid line is the mean value. The dashed and the dotted lines are the 1σ maximum and minimum values respectively.

Once all the above corrections have been applied to the jets in the central region they are transferred to jets in the forward region by using P_t balance. In this method dijet events with at least one jet in the central region are used. The correction is obtained by comparing the P_t of the central jet with the P_t of the other jet as a function of the η of the other jet. This method has the advantage that all the corrections are taken care of automatically thus avoiding the difficulty of getting the corrections in the forward region.

The missing E_t correction just reflects the change in the jet and EM object E_ts after the above corrections are made.

3.8 Summary

In this chapter we have described the online processing of the events collected at D0 followed by the offline processing which is common to all physics analyses. At

this stage of the offline processing all objects in the events have been found and their parameters and characteristics are available. The analysis for the search for the top now consists of making judicious cuts on these events so that backgrounds are eliminated and most of the top signal preserved. This is presented in the next chapter.

CHAPTER 4

ANALYSIS OF COLLIDER DATA

This chapter describes two analyses for the search for the top quark in the dielectron decay channel. The chapter begins with a description of the data sample, the triggers used and the specific electron identification requirements for the analyses. The kinematic cuts used to select a top signal, the motivation for the cuts and the results obtained are then described. An estimate of the expected number of signal and background events is necessary to understand the significance of this result. The description of the procedure for making this estimate and its result conclude this chapter.

The kinematic cuts used to arrive at a top signal were designed after a study of the kinematics of the top and background processes and estimating the number of signal and background events in the data collected. As the kinematics of the top quark decay depends upon the mass of the top quark (m_t), optimal kinematic cuts for top signal had to be determined by generating Monte Carlo events in the mass range in which the search was being made. Thus for the first analysis (Analysis I) the cuts were designed to search for the top quark at a mass greater than the lower mass limit of 91 GeV/c^2 set by CDF and up to a mass of 120 GeV/c^2. The cuts were such that at least a few signal events were expected for a reasonable signal to background ratio. The second analysis (Analysis II) concentrated the search at higher values of m_t.

4.1 Data Sample

This analysis used data from the 1992-93 collider run. The entire data was used with the exception of data collected during bad runs and events which had the micro blank bit on. Bad runs are runs taken when the detector or the data acquisition system had problems. These were problems which resulted in faulty data which could not be corrected during offline processing. Some of the typical problems which resulted in this kind of data loss are: Level 2 trigger corruption, bad calorimeter octants, no level 0 readout, and corruption of muon readout. The micro blank bit for an event was turned on if the particular event occurred when a main ring bunch passed the D0 detector — this is a time period when there are huge losses in the detector. The integrated luminosity of the entire run was $14.6\,\mathrm{pb}^{-1}$. The integrated luminosity of bad runs was $0.195\,\mathrm{pb}^{-1}$. The correction factor for micro blanked bits is 0.94. Correction for both sources of data loss yields an integrated luminosity of

$$13.5 \pm 1.6\,\mathrm{pb}^{-1}$$

where the standard D0 luminosity error of $\pm 12\%$ [section 3.1] is used.

4.2 Triggers

It is required that the events satisfy one or more of the three triggers ELE_JET, ELE_HIGH or ELE_2_HIGH. At the level 2 stage the first trigger which is the primary dielectron channel trigger demands the presence of one high energy electron, two energetic jets (which at level 2 also includes electrons) and large missing transverse energy. The second (third) trigger demands the presence of one (two) high energy electron only to safeguard against losing events with mismeasured missing transverse energy. The definition of these triggers is shown in table 4.1. The efficiency of this

Table 4.1. Triggers used in $t\bar{t} \rightarrow ee$ analysis.

Trigger name	Trigger condition	Level1	Level2
ELE_JET	EM(1,10) + JT(2,5) + L2EM(1,15) + L2JET(2,10) + L2MS(10)	1 EM tower with $E_t > 10$ GeV 2 Jets with $E_t > 5$ GeV	1 e with $E_t > 15$ GeV 2 Jets with $E_t > 10$ GeV $\not\!\!E_t > 10$ GeV
ELE_HIGH	EM(1,10) + L2EM(1,20)	1 EM tower with $E_t > 10$ GeV, MB	1 e with $E_t > 20$ GeV
ELE_2_HIGH	EM(2,7) + L2EM(2,10)	2 EM towers with $E_t > 7$ GeV	2 e with $E_t > 10$ GeV

trigger condition was determined by the trigger simulator [44, 45] to vary from 86% for a top mass of 80 GeV/c^2 to 94% for a top mass of 180 GeV/c^2 as shown in table 4.2.

Table 4.2. Trigger efficiency for various values of top mass.

Top mass (GeV/c^2)	Trigger efficiency (%)
80	86
100	90
120	91
140	93
160	93
180	94

A total of $\sim$ 2.2 million events passed these triggers. These events were then reconstructed by D0RECO and passed through the event selection criteria described in the next section to arrive at the final signal sample.

4.3 Event Selection

The event selection criteria imposed on the reconstructed events were chosen to maximize the efficiency for $t\bar{t}$ events and at the same time minimize the background. The definitions of an electron used in the selection criteria is given below. This is followed by the description of the kinematic cuts which constitute the selection criteria.

4.3.1 Electron Definition

A list of electrons in an event and their parameters is provided by the reconstruction package D0RECO. The algorithm used in their definition has been described in section 3.6. The parameters involved in the electron definition are:

1. *EM fraction (f_{EM}),*
2. *Cluster shape (χ^2),*
3. *Trackmatch significance (S),*
4. *Track ionization (dE/dx), and*
5. *Isolation (f_{iso}).*

D0RECO makes cuts on only one these five parameters (EM fraction, $f_{EM} > 0.9$) in identifying an object as an electron.

For further analysis, two sets of electron identification criteria are defined by imposing cuts on the remaining four parameters. These are termed 'loose' and 'tight' and are different for Analysis I and Analysis II. The definitions are shown in table 4.3 and 4.4 which also show the corresponding efficiencies for both the central calorimeter (CC) and the end calorimeters (EC). The main objective of the additional cuts is to obtain more rejection against backgrounds and at the same time maintain a reasonable efficiency for identifying electrons from $t\bar{t} \rightarrow ee$ decay. From the table it can be

Table 4.3. Electron definition (Analysis I).

EID criteria	Definition	Efficiency in CC and EC	$P_{j\to e}$ ($\times 10^{-4}$) in CC and EC[a]
Loose I	$f_{iso} < 0.1$, $\chi^2 < 100/200$[b] No track match significance (S) cut	77.3%, 79.5%	2.21, 8.61
Tight I	$f_{iso} < 0.1$, $\chi^2 < 100/200$ $S < 5.0$	73.1%, 54.5%	1.48, 2.03

[a]The probability of a jet being misidentified as an electron

[b]100/200 are the cut values for CC and EC respectively

Table 4.4. Electron definition (Analysis II).

EID criteria	Definition	Efficiency in CC and EC	$P_{j\to e}$ ($\times 10^{-4}$) in CC and EC[a]
Loose II	$f_{iso} < 0.1$, $\chi^2 < 100$ $S < 5.0$, No dE/dx cut	76.7%, 56.6%	2.5, 3.3
Tight II	$f_{iso} < 0.1$, $\chi^2 < 100$ $S < 5.0$ $dE/dx_{cdc} < 1.5$ or $dE/dx_{cdc} > 3.0$ $dE/dx_{fdc} < 1.3$ or $dE/dx_{fdc} > 2.5$	72.4%, 45.6%	0.8, 2.0

[a]The probability of a jet being misidentified as an electron

seen that the additional trackmatch significance (S) requirement (Analysis I) and the track-ionization (dE/dx) requirements in the tracking chambers (Analysis II) for the 'tight' electron increases the rejection against misidentified jets by a factor of $\sim$ 3–4 in the EC and CC respectively.

4.3.2 Kinematic Cuts

The kinematic cuts which constitute the event selection criteria are described below in the order in which they were made. The motivation for making these cuts and the effect of the cuts on data are also described.

1. **Electron cuts:** A minimum of two electrons with $E_t > 20\,\mathrm{GeV}$ and $|\eta| < 2.5$ are required. At least one of the electrons should be tight. The other electron can be tight or loose. This cut suppresses background from $b\bar{b}$, $c\bar{c} \rightarrow ee$, Drell-Yan and misidentified jets. The electrons produced through b and c quark decay are not as well isolated as electrons from top (both the 'tight' and 'loose' criteria require well isolated electrons). This is true for misidentified jets also. Furthermore most $b\bar{b}$, $c\bar{c} \rightarrow ee$ and Drell-Yan events are not expected to produce electrons which have a large E_t. Figure 4.1 has a plot of the E_t of the second leading electron (the electron with the second highest E_t) for Monte Carlo (MC) generated $t\bar{t} \rightarrow ee$ (figure 4.1a) and $b\bar{b}$, $c\bar{c} \rightarrow ee$ (figure 4.1b) events. It can be observed that the E_t of the electron is a very sharply falling curve for the $b\bar{b}$, $c\bar{c} \rightarrow ee$ background. The electron cuts have an efficiency of $19 \pm 2\%$ for $t\bar{t} \rightarrow ee$ (this includes detector acceptance, electron reconstruction and electron selection efficiencies) and rejects $99 \pm 1\%$ of the $b\bar{b}$ $c\bar{c} \rightarrow ee$ background. Imposing the tight criteria for EID reduces electron background from jets which get misidentified as electrons, and conversion electrons. This reduces significant 'instrumental backgrounds' from W + jets and QCD processes. This criteria is

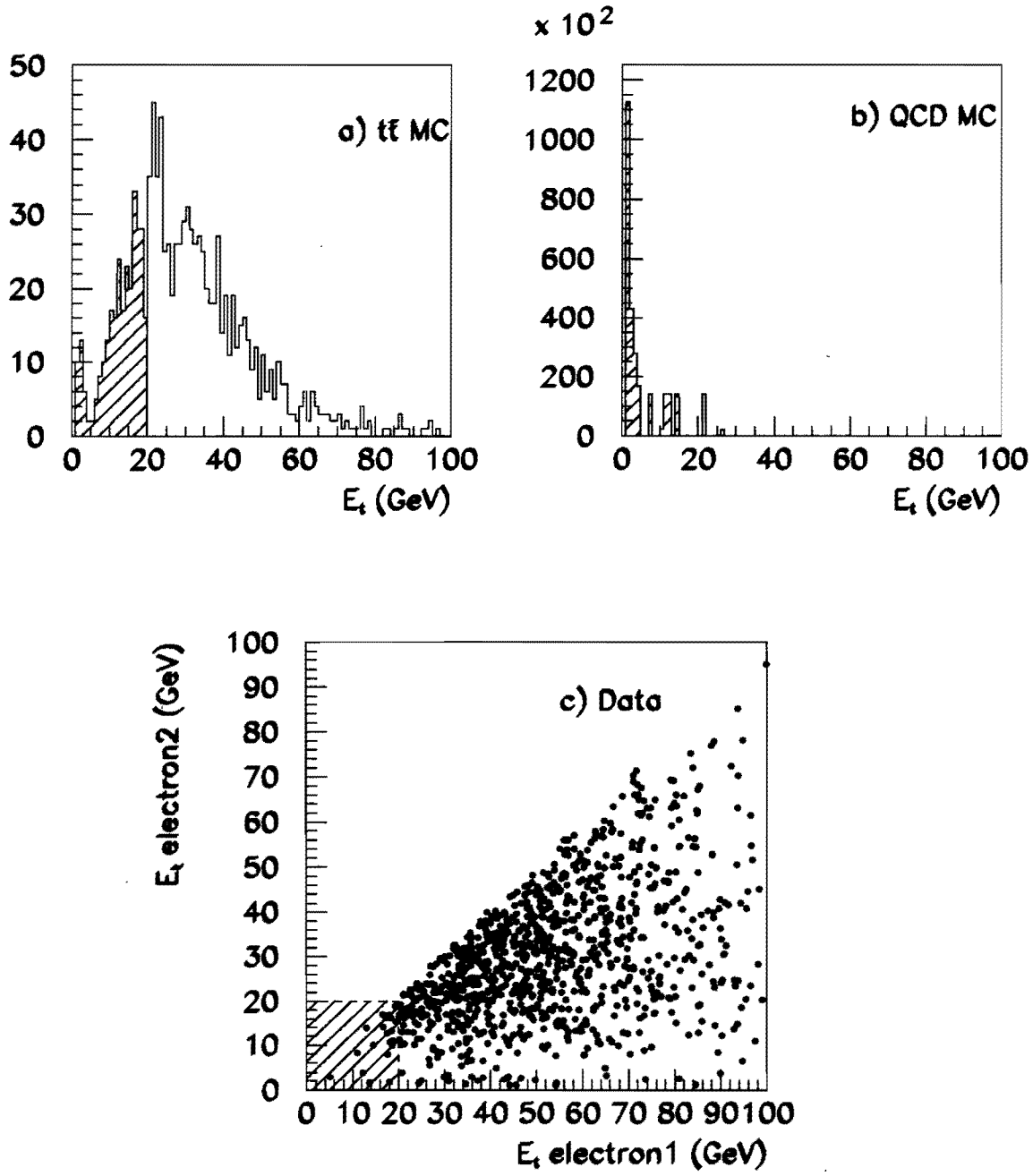

Figure 4.1. (a) E_t spectrum of second leading electron for $t\bar{t}$ ($m_t = 140$ GeV) (b) QCD Monte Carlo (c) scatterplot of E_t of first leading electron versus the second for Data.

imposed on only one of the electrons in favor of retaining a higher efficiency. 999 and 739 data events survive this cut for Analysis I and Analysis II respectively. In figure 4.1c, the events of Analysis II are presented as a scatter plot of two electron transverse energies. The events which survive this cut in Analysis II are shown in the unshaded region.

2. **Z mass cut:** Events in which the dielectron invariant mass of the leading electron pair lies in the Z mass region are rejected, if the $\not\!\!E_t$ < 40 GeV. The leading electron pair consists of the two electrons which have the highest E_t. The Z mass region is taken to be the region between 79 GeV/c^2 and 103 GeV/c^2 which is $|\Delta M_Z| \leq 12$ GeV/c^2. This cut has been determined from a study of $t\bar{t} \rightarrow ee$ MC events, $Z \rightarrow ee$ MC events and jet data. Figure 4.2 has the $\not\!\!E_t$ plotted vs. the dielectron invariant mass for $t\bar{t} \rightarrow ee$ and $Z \rightarrow ee$ MC events which have passed cut 1. The plots illustrate the discrimination provided by this cut against the $Z \rightarrow ee$ background and also show the increase in the acceptance for top events with $\not\!\!E_t$ > 40 GeV obtained by accepting events with $\not\!\!E_t$ > 40 GeV. The increase in acceptance is 15% of all top events (top mass 140 GeV/c^2) which have passed cut 1. The cut value of 40 GeV on $\not\!\!E_t$ is motivated by the $\not\!\!E_t$ spectrum for jet data shown in figure 4.3. It is seen that the probability of jet events (which are also not expected to have much $\not\!\!E_t$ like the $Z \rightarrow ee$ events) having $\not\!\!E_t$ > 40 GeV is small (0.0014). For Analysis I (II) 169 (111) out of the 999 (739) data events survive this cut. The effect of this cut on data is illustrated in figure 4.2 for Analysis II where the plotted events have already passed cut 1.

3. **Missing E_t cut:** Events which have a $\not\!\!E_t$ < 25 GeV are rejected. After the preceding two cuts most of the background is expected to be from $Z \rightarrow \tau\tau$, $WW \rightarrow ee$ and Drell-Yan events. There are also some $Z \rightarrow ee$ events (Zs with

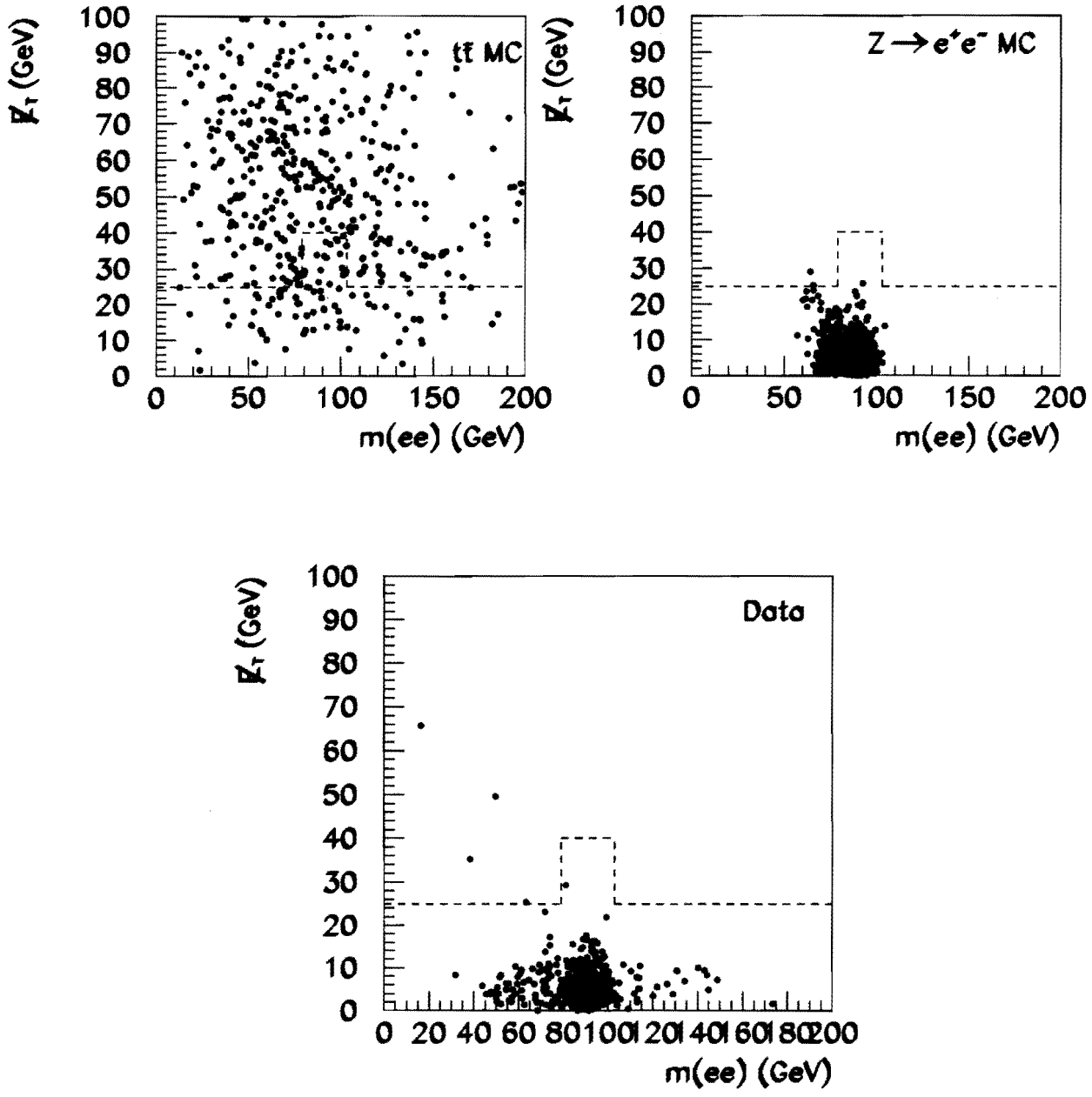

Figure 4.2. $\not\!\!E_t$ vs M_{ee} for $t\bar{t}$ and $Z \rightarrow ee$ Monte Carlo, and Data. The plotted events have passed electron cuts.

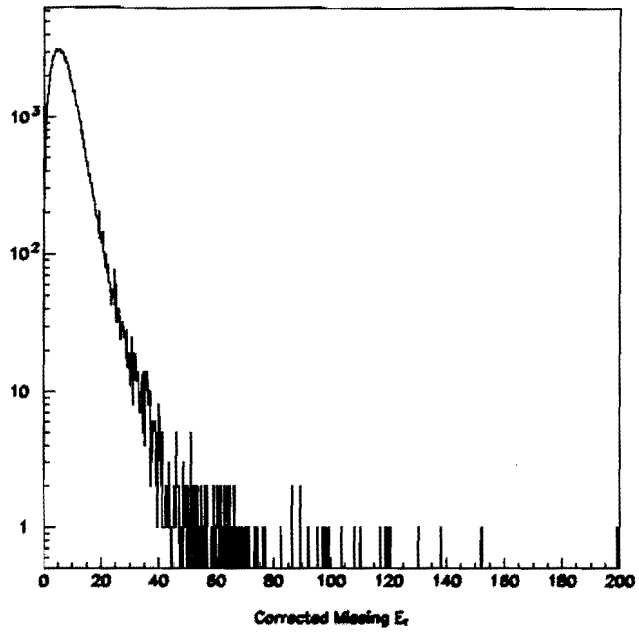

Figure 4.3. $\not\!\!E_t$ spectrum for jet data.

mismeasured electrons) which do not lie in the mass window of cut 2. However $Z \rightarrow \tau\tau$, Drell-Yan and $Z \rightarrow ee$ events are not expected to have significant $\not\!\!E_t$. This can be seen in fig. 4.2 for $Z \rightarrow ee$ events and in fig. 4.4 for $Z \rightarrow \tau\tau$ and $WW \rightarrow ee$ events. The events in fig. 4.4 have already passed cuts 1 and 2. Fig. 4.4 also shows the $\not\!\!E_t$ for $t\bar{t} \rightarrow ee$ MC events. The events in the shaded area of the figure are the events which are lost because of the cut. This is only 17% for the top signal and 27% for $WW \rightarrow ee$ but 96% for $Z \rightarrow \tau\tau$. Only 4 data events survive this cut. The effect of this cut on data is illustrated in figure 4.4 for Analysis II where the plotted events have already passed cut 1 and 2.

4. **Jet E_t cut:** At least 1 jet with $E_t > 15\,\text{GeV}$ is required for Analysis I. For Analysis II at least 2 jets with $E_t > 15\,\text{GeV}$ and $|\eta| \leq 2.5$ are required. At this stage most of the background to the signal is from $WW \rightarrow ee$ events. These events are very much similar to the top quark in all the variables on which cuts

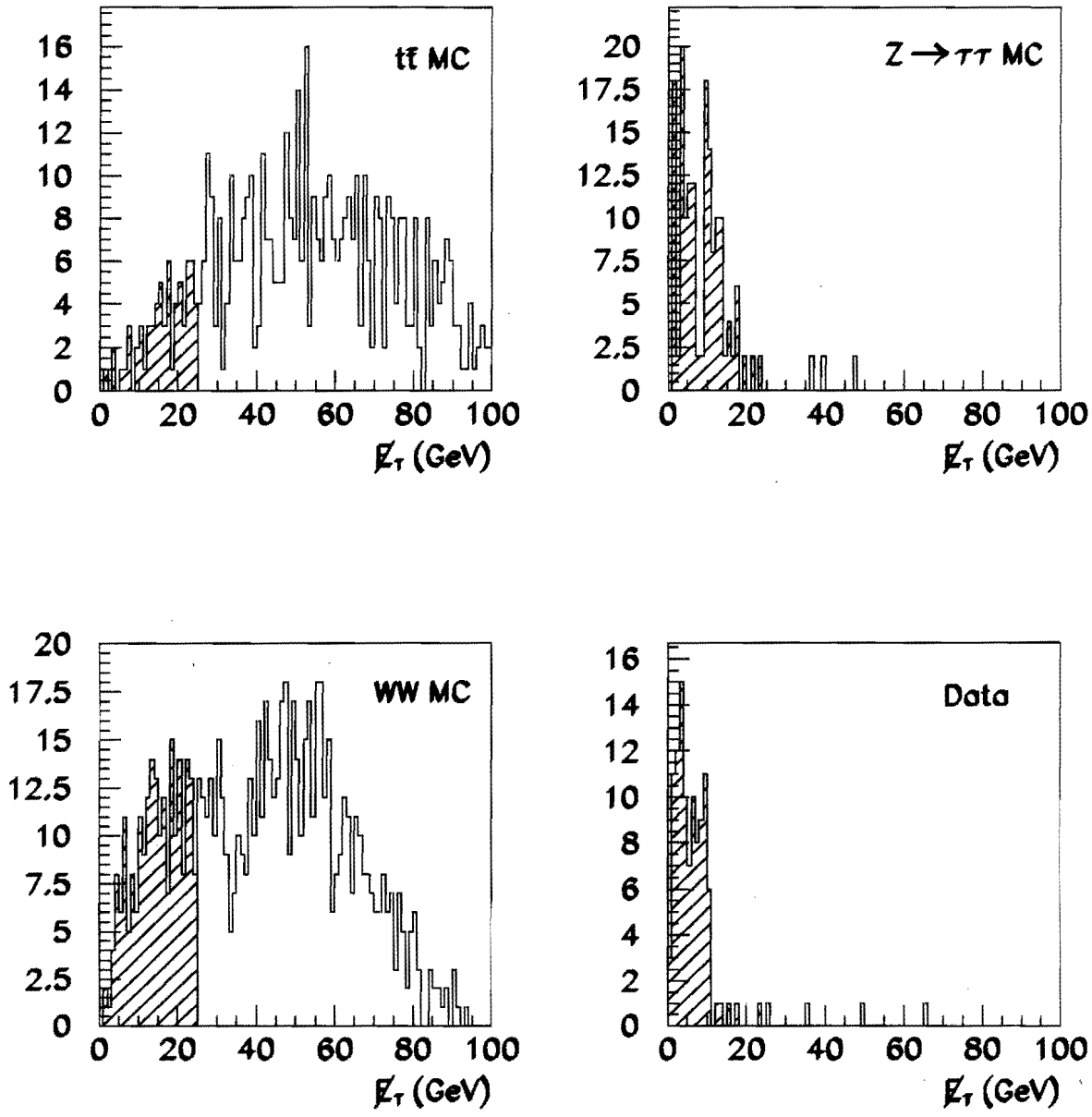

Figure 4.4. $\not\!\!E_t$ spectrum for $t\bar{t}$, $Z \rightarrow \tau\tau$, and $WW \rightarrow ee$ Monte Carlo, and Data. The events plotted have passed electron E_t cut and Z mass cut.

Table 4.5. Effect of cuts on data.

Cut ⇓	Number of events passing cut	
	Analysis I	Analysis II
Electron cut	999	739
Z mass cut	169	111
$\not\!\!E_t$ cut	4	4
Jet cut	1	0

Table 4.6. Top candidate from Analysis I (Run 55642, Event 166).

Particle	E_t (GeV)	η	ϕ (rad)
Electron 1	36.0 ± 1.0	-0.14	3.91
Electron 2	28.9 ± 0.8	0.50	5.42
Jet 1	69.5 ± 12.1	-0.85	0.72
Jet 2	17.7 ± 3.1	-2.52	5.15
$\not\!\!E_t$	44.6 ± 12.2		3.01

have been made - electron E_t, $\not\!\!E_t$ and the dielectron invariant mass. However they are not expected to have two high E_t jets whereas 92% of the top events which pass the previous cuts have 2 jets (expected from the b quark) with $E_t > 15$ GeV. Fig. 4.5 shows the number of jets (with $E_t > 15$ GeV) for $t\bar{t} \rightarrow ee$ and $WW \rightarrow ee$ MC events which have passed all the previous cuts. This cut also reduces the remaining background resulting from misidentified jets. Only one event from data survived this cut for Analysis I and no event survived this cut for Analysis II.

The effect of all cuts is summarized in table 4.5. The one event which survives all selection criteria in Analysis I contains two high E_t electrons, two jets and large $\not\!\!E_t$. The details of this event are given in table 4.6. This event does not survive the selection cuts of Analysis II because the $|\eta|$ of the second jet is more than 2.5.

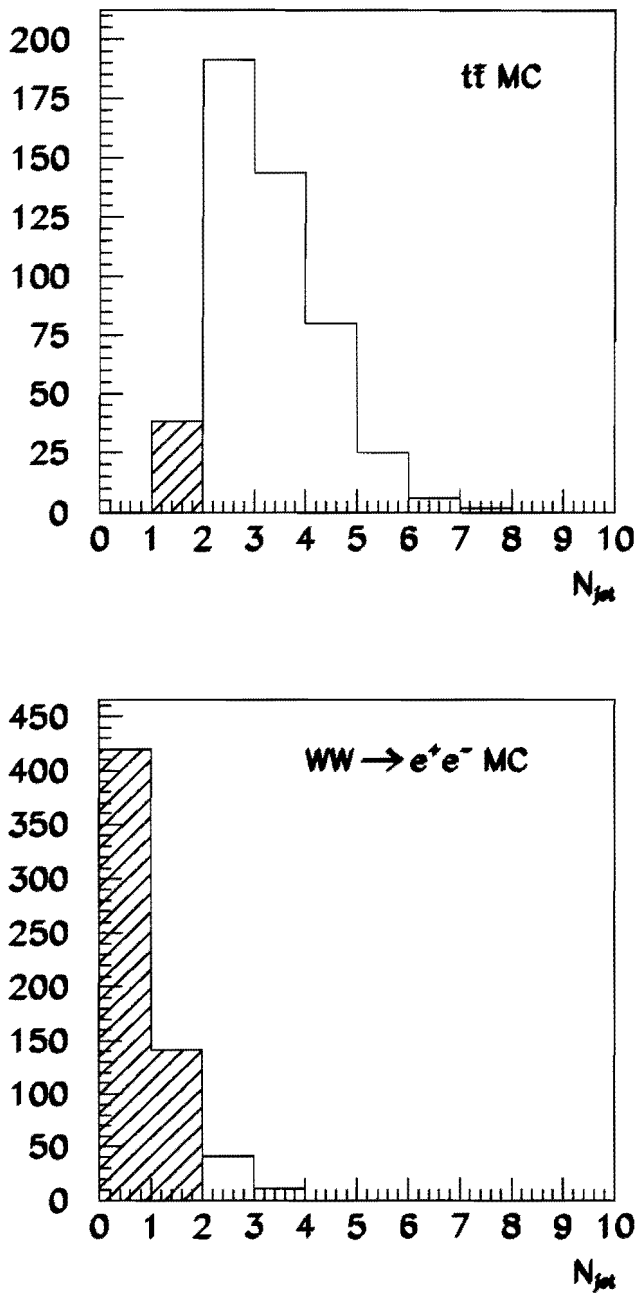

Figure 4.5. Number of jets with $E_t > 15$ GeV for $t\bar{t}$ and $WW \rightarrow ee$ Monte Carlo.The plotted events have passed all kinematic cuts except for the jet cuts.

4.4 Calculation Of Expected Background

4.4.1 Physics Background

Backgrounds to the top signal from processes which can produce dielectron final state signatures similar to the top are termed physics backgrounds [as discussed in section 1.3]. Most of these backgrounds are estimated by using Monte Carlo samples of the particular physics process under consideration. The number of background events which will pass the kinematic cuts and make it to the signal can be estimated by the same procedure which is used to estimate the signal from the top as discussed in the next section (4.5). However in order to use the available computing resources in an efficient manner, the complete Monte Carlo samples were not processed. Only preselected events which passed looser selection criteria were processed [58]. The details of the study of the various processes which were considered to be possible physics backgrounds for $t\bar{t} \rightarrow ee$ are as follows.

1. $Z \rightarrow ee$: 10,000 $Z \rightarrow ee$ events were generated by the ISAJET event generator and passed through both D0GEANT and D0RECO. Though a significant number of events pass the electron cuts, the Z mass cut and the missing E_t cut reduce this background significantly. No events survive after the jet cut. This gives an estimate of < 0.15 for the expected number of events from this background process. In order to improve this result (arising from low statistics) 100,000 ISAJET events were generated and smeared with the detector resolution for jets and electrons. Again none of the events pass all the cuts applied on data. This reduces the estimate for the expected number of events from this background to < 0.015 events.

   As estimate of the above number was performed using data also. This was done by counting the number of $Z + 2$ jet events (jet $E_t > 15$ GeV) in the data

sample. The number of these events (22) multiplied by the probability of the event having $\not\!\!E_t$ > 40 GeV (0.0014) gives the number of expected events from this process (0.03). The above probability is again obtained from figure 4.3 by counting the number of events with $\not\!\!E_t$ > 40 GeV and dividing it by the total number of events. Based on this study the number of background events for this process was conservatively estimated to be 0.03 ± 0.02

2. $Z \rightarrow \tau\tau \rightarrow ee$: 2500 ISAJET events were generated for this process and passed through D0GEANT and D0RECO. The $\not\!\!E_t$ cut is the most effective in reducing this background. The number of events which survive all the cuts is 4.

3. $WW \rightarrow ee$: This is a background process which is hard to discriminate against because of its close resemblance to the $t\bar{t} \rightarrow ee$ signature. Only the jet cuts provides significant reduction for this background. This reduction is sufficient because of the small cross section for this process (9.5 pb [56]. The study was performed using 2500 $WW \rightarrow ee$ events which were generated using the PYTHIA event generator and then passed through both D0GEANT and D0RECO. A total of 34 events survive all the cuts.

4. $QCD \rightarrow ee$: This background was studied very carefully because of the huge cross-section for QCD multijet production. The jet P_t spectrum for this process falls exponentially. Because of this Monte Carlo events were generated in different P_t bins as otherwise all events generated would be clustered near the low end of the spectrum. 2000 to 5000 $QCD \rightarrow ee$ events were generated in 9 P_t bins (10-20, 20-40, 40-60, 60-80, 80-100, 100-130, 130-160, 160-200 and 200-240 GeV/c) and passed through D0GEANT and D0RECO. These events included direct $b\bar{b}$ and $c\bar{c}$ and gluon bremsstrahlung to $b\bar{b}$ and $c\bar{c}$ and contained electrons from b and c decays only. The tight electron isolation requirement reduces this background significantly. No events survive all the cuts.

5. W + jets $\rightarrow$ ee: The jets in this background process are mainly gluon jets. Because of this, the probability of obtaining events with 2 prompt and isolated electrons is very small. This study was not carried on after the ISAJET generator stage.

6. Drell-Yan: $\gamma \rightarrow ee$: These events have a falling E_t spectrum. They also do not have much missing E_t. At the ISAJET generator stage the contribution from this process was determined to be negligible after electron E_t and missing E_t cuts.

7. $Z \rightarrow b\bar{b} \rightarrow ee$: Electrons from b decay are not well isolated and also the electron E_t spectrum starts falling before 20 GeV. The ISAJET study was enough to conclude that this process would not be a significant background.

8. $Z \rightarrow c\bar{c} \rightarrow ee$: The background from this process should be lower than the background from $Z \rightarrow b\bar{b} \rightarrow ee$. This is because electrons from c decay should have a lower E_t and be less isolated than electrons from b. This study was also done till the ISAJET stage only.

9. Drell-Yan: $\gamma \rightarrow \tau\tau \rightarrow ee$: This process was determined to contribute insignificantly after a study at the generator level. These events are like Drell-Yan: $\gamma \rightarrow ee$. They can have a larger $\not\!\!E_t$ but the cross section for the process is much lower.

10. $WZ \rightarrow ee$ The cross section for this process is predicted to be a factor of 10 smaller than the $WW \rightarrow ee$ cross section. Consequently the background contribution from this process was neglected.

11. $W\gamma \rightarrow ee$ This process is a background whenever the γ is misidentified as an electron. This happens when there is an accidental overlap of a track from the underlying event or when the γ converts.

The backgrounds from the physics processes 1–4 are tabulated in 4.7, the processes 5–11 do not contribute significantly to the background. In the table the quoted error

Table 4.7. Number of physics background events expected in $13.5\,\mathrm{pb}^{-1}$.

BACKGROUND	Number of events in $13.5\,\mathrm{pb}^{-1}$	
	Analysis I	Analysis II
$Z \rightarrow ee$	0.03 ± 0.03	0.03 ± 0.02
$Z \rightarrow \tau\tau \rightarrow ee$	0.09 ± 0.04	0.05 ± 0.03
$WW \rightarrow ee$	0.07 ± 0.01	0.01 ± 0.01
$b\bar{b}\,, c\bar{c} \rightarrow ee$	0.02 ± 0.01	0.02 ± 0.02
total	0.21 ± 0.05	0.11 ± 0.04

includes the statistical error and the dominant systematic error of 14%. The sources contributing to this systematic error and their values are listed in table 4.8. These

Table 4.8. Source of systematic errors and their values.

Source	Error (%)
Event simulation	8
Uncertainties in event reconstruction	10
electron identification	5
Modelling of trigger acceptance	5
total	14

include the contribution from uncertainties in event simulation (ISAJET was used as the event generator for all the background processes except $WW \rightarrow ee$ which was simulated using PYTHIA), detector modelling (GEANT [47]) and trigger acceptances. There is also an additional normalization error arising from the uncertainty in the integrated luminosity of 12%.

4.4.2 Instrumental Background

The instrumental background [section 1.3] is mostly due to W+jets events where one of the electron is from the W decay and the other is an electron due to a misidentified jet. The other source is from QCD events where two jets are misidentified as an electron and the $\not\!\!E_t$ in the event is due to the mismeasurement of the jets.

In order to determine this background a data sample was selected by requiring an electron with $E_T > 20$ GeV, $\not\!\!E_t > 25$ GeV and a jet with $E_T > 15$ GeV. These events were also required to pass the same triggers as the signal events. The number of background events from instrumental misidentification is then given by

$$N_{\text{fakes}} = N \times P_{\text{j}\to\text{e}}$$

where

N_{fakes} Number of estimated fakes

N Number of jets with $E_T > 20$ GeV in background data sample which when misidentified would result in a $t\bar{t} \to ee$ signal

$P_{\text{j}\to\text{e}}$ Probability of jet faking an electron

The probability of a jet being misidentified as an electron is determined by using a jet data sample. This sample has a very low "isolated" electron contamination. Therefore an "electron" found in this data sample, if any, should predominantly be from a misidentified jet. This rate is computed as

$$P_{\text{j}\to\text{e}} = \frac{N_{\text{electrons}}}{N_{\text{jets}}}$$

where

$N_{\text{electrons}}$ is the number of "electrons" with $E_t > 20$ GeV passing EID requirements.

N_{jets} is the total number of jets in the QCD jet trigger sample with $E_t > 20$ GeV.

It is found that $P_{\text{j}\to\text{e}}$ is different for CC and EC fiducial regions and is different for "tight" and "loose" EID criteria (table 4.9).

Table 4.9. Probability of jet being misidentified as electron.

	CC (10^{-4})	EC (10^{-4})
Analysis I		
$P_{\text{j}\to\text{etight}}$	1.48 ± 0.49	2.03 ± 1.02
$P_{\text{j}\to\text{eloose}}$	2.21 ± 0.90	8.61 ± 2.09
Analysis II		
$P_{\text{j}\to\text{etight}}$	0.8 ± 0.4	2.0 ± 1.0
$P_{\text{j}\to\text{eloose}}$	2.5 ± 1.2	3.3 ± 2.0

This made it necessary to divide the data sample in the following way (for Analysis II) and calculate "N" for each of them separately.

1. Events which have at least one loose electron with $E_t > 20$ GeV, three or more jets with $E_t > 15$ GeV where at least one jet has $E_t > 20$ GeV. These events are also required to survive the $\not\!\!E_t$ cut.

2. Events which have at least one tight electron with $E_t > 20$ GeV, three or more jets with $E_t > 15$ GeV where at least one jet has $E_t > 20$ GeV. Again these events should pass the $\not\!\!E_t$ cut.

In the two samples above the number of jets with $E_t > 20$ GeV in the CC ($N1_{cc}$ and $N2_{cc}$) and EC ($N2_{cc}$ and $N2_{ec}$) are counted. Using the probability that a jet is misidentified as an electron from table 4.9 the following three numbers are computed

1. The number of events in sample 1 where a jet is misidentified as the second electron which is tight ($N1_{cc} \times Pt_{cc} + N1_{ec} \times Pt_{ec}$):

$$N_1 = 0.029 \pm 0.015 \text{ events}$$

2. The number of events in sample 2 where a jet is misidentified as the second electron which is loose ($N2_{cc} \times Pl_{cc} + Nl_{ec} \times Pl_{ec}$):

$$N_2 = 0.043 \pm 0.021 \text{ events}$$

3. The number of events in sample 2 where a jet is misidentified as the second electron which is tight ($N2_{cc} \times Pt_{cc} + N2_{ec} \times Pt_{ec}$):

$$N_3 = 0.019 \pm 0.007 \text{ events}$$

Addition of N_1 and N_2 gives the number of fake events with one electron which is a misidentified jet where the number of fake events having two tight electrons are double counted. Subtracting N_3 from this number gives us the required number (for Analysis II):

$$N_{\text{fakes}} = N_1 + N_2 - N_3 = 0.05 \pm 0.03 \text{ events (Analysis II).}$$

(The corresponding number for Analysis I obtained by a similar method is 0.32 ± 0.014 events.)

4.4.3 *Total Background*

The number of background events in 13.5 pb^{-1} of data is tabulated in table 4.10 for each significant physics background and for fakes. These numbers are tabulated for the cases when all the kinematic cuts have been applied, when the jet cut is not applied and when both the jet and Z mass cut have not been applied. These numbers illustrate the effectiveness of the cuts in the rejection of any particular background. Assuming the absence of a top signal the total background estimate should be equal to the number of events actually observed in the data. A reasonable agreement between the two numbers gives us confidence on the estimate of the total background. It is seen that the numbers agree reasonably well for the case when no Z mass cut and jet cuts have been applied. However for the case when only the jet cuts have not been applied the expected background is 0.92 ± 0.27, some what lower than the number of observed events which is 4.

Table 4.10. Number of background events expected in 13.5 pb^{-1} of data (Analysis II)).

BACKGROUND	No Z mass and Jet cut	No jet cut	After all cuts
$WW \rightarrow ee$	0.24 ± 0.04	0.22 ± 0.04	0.01 ± 0.01
$Z \rightarrow \tau\tau \rightarrow ee$	0.08 ± 0.03	0.08 ± 0.03	0.05 ± 0.03
$Z \rightarrow ee$	5.90 ± 0.37	0.14 ± 0.14	0.03 ± 0.02
$QCD \rightarrow ee$	0.02 ± 0.02	0.02 ± 0.02	0.02 ± 0.02
fakes	0.46 ± 0.23	0.46 ± 0.23	0.05 ± 0.03
total	6.70 ± 0.44	0.92 ± 0.27	0.16 ± 0.07
Data	5	4	0

4.5 *Calculation of Expected Signal*

The number of expected events is given by the formula:

$$n = \mathcal{L} \times \sigma \times Br \times Eff$$

where

1. $\mathcal{L}$ is the integrated luminosity of the data sample. Its value is $13.5\,\mathrm{pb}^{-1}$ as described earlier in this chapter.

2. σ is the Cross section for the production of the top quark. The central value from the paper by Laenen et al.[17] was used.

3. **Br** is the branching ratio for decay into the ee final state: $t\bar{t} \rightarrow W^+bW^-b \rightarrow e^-e^+\nu\bar{\nu}b\bar{b}$. The value is 1.24% as mentioned in the introduction.

4. **Eff** is the efficiency of detecting the top quark in the ee decay channel. The efficiency can be factorized as follows:

$$Eff = E_{trig} \times E_{acc} \times E_{eid} \times E_{cuts}$$

where

E_{trig} Trigger efficiency

E_{acc} Acceptance efficiency, given E_{trig}.

E_{eid} Electron ID efficiency

E_{cuts} Efficiency of kinematic cuts, given E_{trig} and E_{acc}.

E_{acc} has to be evaluated once E_{trig} is determined and similarly E_{cuts} after E_{trig} and E_{acc}. In practice the product $E_{acc} \times E_{cuts}$ is evaluated together, after E_{trig}

is determined. All the three factors E_{trig}, E_{acc} and E_{cuts} depend upon the kinematics of top production and decay, and are assumed to be independent of E_{eid}. They are determined by generating $t\bar{t} \rightarrow ee$ Monte Carlo events and then passing them through a simulation of the detector and the triggers. The ISAJET event generator [46], detector simulation package based on GEANT [48] and the trigger simulator [44, 45] were used for this purpose. The procedure is as follows: A known number (N_{tot}) of events are generated by the event generator. N_{tot} should be large enough so that the statistical error in the calculation is small or at least comparable to the error from other sources. Because of the large amount of computer time required to run the simulation packages (especially the detector simulation) the number N_{tot} is limited by the amount of computing resources available. The N_{tot} events are passed through the detector simulation whose output is in a format which is very similar to the real data events from collider operations. This output is then passed through the trigger simulator. The ratio of numbers which the trigger simulator passes (N_{trig}) to N_{tot} is the trigger efficiency. This number has some of the geometrical acceptance of the detector folded into it. This output is then reconstructed by the same program which reconstructs the real data. The kinematical cuts are now applied to the reconstructed Monte Carlo events as one would do for real data except that EID requirements are not applied on the EM clusters. The ratio of the number of events which survive the cuts(N_{cuts}) to N_{trig} is the product of E_{acc} and E_{cuts}. Thus at this stage one has all the efficiency numbers except for E_{eid}. This number is determined from $Z \rightarrow ee$ data [57]. The efficiency is different for tight and loose electrons and is also different in the CC and EC. This means that the following kinds of top events will have different EID efficiencies - Events with both the required electrons in the CC, both required electrons in the EC and finally events with one required electron in the CC and one in the EC. The

number of events of each kind are counted and applied as a weight to get the overall EID efficiency.

$$E_{eid} = \frac{N_1 \times E_1 + N_1 \times E_2 + N_3 \times E_3}{N_1 + N_2 + N_3}$$

where

N_1,E_1 are the number and EID efficiency of events with both required electrons in the CC

N_2,E_2 are the number and EID efficiency of events with both required electrons in the EC

N_3,E_3 are the number and EID efficiency of events with one required electron in the CC and the other in EC.

E_1 is given by the expression $e_{xc}^2(2 \times (e_{tc} \times e_{tct}) - e_{tct}^2)$

e_{xc} is the efficiency of isolation and h-matrix χ^2 cuts in the CC

e_{tc} is the efficiency of finding an electron track in the CC.

e_{tct} is the efficiency of the 'tight' criteria in the CC after an electron track has been found.

The expressions for E_2 and E_3 follow in a similar way.

The expected number of $t\bar{t}$ events in the signal is shown in table 4.11 for various values of top mass. The table also shows the efficiency and the product of the cross section and branching ratio for each top mass.

The number of events estimated as above gives us the expected number of $t\bar{t}$ events in the signal which have decayed into the dielectron channel. However $t\bar{t}$ events decaying into the $e\tau$ and $\tau\tau$ decay channels can also have the signature of the dielectron channel

Table 4.11. Event yield.

Top mass in GeV/c^2	$\sigma\times$ BR(ee)	Eff.(%)[a] I	Eff.(%)[a] II	# of events in 13.5pb^{-1} I	# of events in 13.5pb^{-1} II
80	2.10	9.3		5.2 ± 0.09	
100	0.83	14.7		2.5 ± 0.45	
120	0.37	18.7	10.3	1.2 ± 0.21	0.67 ± 0.12
140	0.18	19.5	12.8	0.6 ± 0.10	0.36 ± 0.07
160	0.095	20.3	14.1	0.3 ± 0.10	0.19 ± 0.04
180	0.052		15.4		0.11 ± 0.02

[a] I and II stand for Analysis I and Analysis II respectively

when the τ decays to an electron. These contributions have to be estimated to give the total number of $t\bar{t}$ events in the signal. They are estimated by the same method described above by using $t\bar{t}$ ISAJET events which decay into the above channels and in which the τs decay to an electron. The results are shown in 4.12 for Analysis II. Figure 4.6 shows a plot of the number of top events one expects to see as a function of top mass for both the analyses.

Table 4.12. Event yield after including contribution from $e\tau$ and $\tau\tau$ channels (Analysis II).

Top mass (GeV/c^2)	$\sigma \times$ BR(ee)	Eff.(%)	# of events in 13.5pb^{-1}
120	0.37	11.3	0.76 ± 0.12
140	0.18	14.1	0.41 ± 0.07
160	0.095	15.6	0.22 ± 0.04
180	0.052	16.5	0.12 ± 0.02

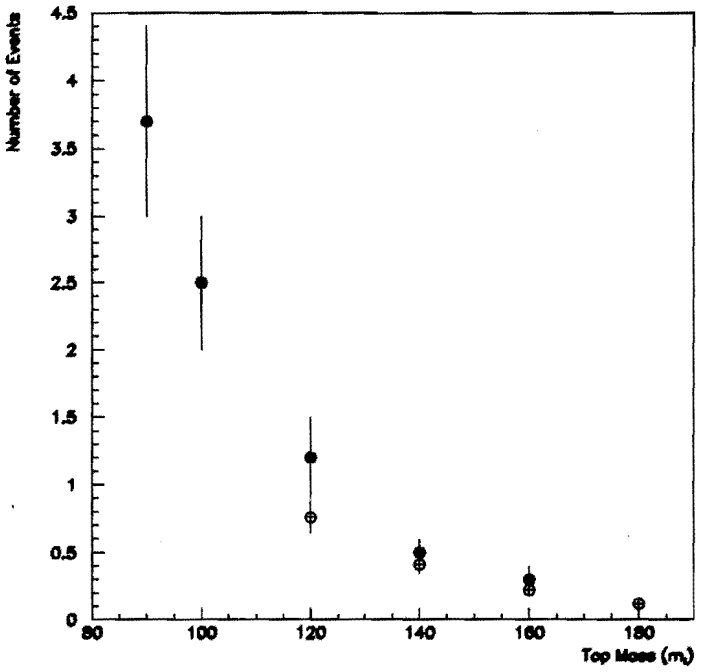

Figure 4.6. Expected number of $t\bar{t} \rightarrow ee$ events as a function of top mass. The solid points are for Analysis I and do not include contributions from $e\tau$ and $\tau\tau$ channels, the hollow points are for AnalysisII and include contributions from $e\tau$ and $\tau\tau$ channels.

CHAPTER 5

CONCLUSIONS

The analyses performed to search for the top quark in the dielectron decay channel were described in the previous chapter. These analyses assume that the top quark decays according to the minimal standard model and hence the conclusions made here are valid only under this assumption. The results of the analyses have also been given in the previous chapter. In summary, Analysis I yields one signal event with an estimated background of 0.5±0.3; Analysis II yields no event with an estimated background of 0.16±0.07 event. These data can be used to set an upper limit on the cross section for the production of top quark. The result is described in the next section. The production of top quark has also been investigated in other top decay channels by the D0 collaboration. A top mass limit based on these channels for Analysis I, and cross sections for $t\bar{t}$ production as a function of top mass for Analysis II are discussed below.

5.1 Cross Section and Top Mass Limit from Analysis I

The cross section for $t\bar{t}$ production is given by the formula

$$\sigma = \frac{N - B}{\epsilon \mathcal{B} \int \mathcal{L}\, dt}.$$

Here N is the number of observed events in a data sample corresponding to an integrated luminosity of $\int \mathcal{L}\, dt$ and ϵ and $\mathcal{B}$ the efficiency for detection of $t\bar{t}$ events in a given channel and the branching ratio in that channel respectively. The upper limit on the cross section at 95% CL is the value of σ below which σ has 95% probability of being, given the resolution on the determination of σ. It is assumed that N follows a Poisson distribution, whereas the factors in the denominator (ϵ and $\int \mathcal{L}\, dt$) are normally distributed. This makes it complicated to determine the distribution of σ. The procedure which was followed to make this determination is explained in [59] which describes both an analytical solution which is solved numerically and a Monte Carlo method which replicates D0's run a large number of times to determine the probability of the actual experiment for a given cross section. The results (for Analysis I) are tabulated in table 5.1 for various values of top mass m_t. Here the background estimate B was not subtracted from the signal sample (1) to arrive at a conservative upper limit. The efficiency values from table 4.11 and the integrated luminosity value of 13.5 pb^{-1} mentioned in section 4.1 were used.

Table 5.1. Upper limit on the cross section for various top masses from $t\bar{t} \rightarrow ee$ Analysis I and combined Analysis I. The combined Analysis I includes results from the ee, $e\mu$, e-jets and μ-jets channels.

	σ_{ul} (pb)	
Top Mass (GeV/c^2)	$t\bar{t} \rightarrow ee$ Analysis I	Combined Analysis I
80	353	
90	250	73.6
100	206	54.3
120	163	27.9
140	156	21.9
160	149	20.0

The upper limit on the cross section has also been obtained by the D0 collaboration by combining results from the search for the top quark in other decay channels.

The decay channels combined with Analysis I for the $t\bar{t} \rightarrow ee$ channel were the corresponding analyses in the $e\mu$, e-jets and μ-jets channels which were optimized to search for the top quark in the mass range $\sim 90 - 120$ GeV/c^2. The $e\mu$ channel is the dilepton channel in which one W decays to an e and the other a μ. The e-jets (μ-jets) channel is a single lepton channel in which one W decays leptonically to an e (μ) and the other to quarks. The product of efficiency (ε) and branching ratio ($\mathcal{B}$), and the number of expected signal ($\langle N \rangle$) and background events for each of the analyses is shown in table 5.2. The Integrated luminosity quoted in this table (and hence $\langle N \rangle$ and the physics background) are different from the earlier published value in [61] because of the change in the world average measured $p\bar{p}$ total cross section used to calculate the integrated luminosity [62]. The upper limit on the cross section obtained

Table 5.2. (Efficiency) $\times$ (branching ratio) ($\varepsilon \times \mathcal{B}$), expected number of events for signal ($\langle N \rangle$) and background for the observed integrated luminosity ($\int \mathcal{L}dt$) and the number of events observed in data for the four channels included in Combined Analysis I.

m_t (GeV/c^2)		ee	$e\mu$	e-jets	μ-jets
	$\varepsilon \times \mathcal{B}$ (%)	0.15 ± 0.02	0.31 ± 0.06	0.28 ± 0.08	0.15 ± 0.07
90	$\langle N \rangle$	3.7 ± 0.7	7.5 ± 1.9	6.8 ± 2.4	2.7 ± 1.5
	$\varepsilon \times \mathcal{B}$ (%)	0.18 ± 0.02	0.39 ± 0.07	0.44 ± 0.12	0.19 ± 0.08
100	$\langle N \rangle$	2.5 ± 0.5	5.4 ± 1.3	6.0 ± 2.0	2.0 ± 1.0
	$\varepsilon \times \mathcal{B}$ (%)	0.23 ± 0.03	0.42 ± 0.08	1.13 ± 0.22	0.61 ± 0.20
120	$\langle N \rangle$	1.2 ± 0.3	2.2 ± 0.6	6.0 ± 1.5	2.4 ± 0.9
	$\varepsilon \times \mathcal{B}$ (%)	0.24 ± 0.03	0.46 ± 0.09	1.45 ± 0.19	0.90 ± 0.27
140	$\langle N \rangle$	0.5 ± 0.1	1.1 ± 0.3	3.3 ± 0.7	1.5 ± 0.6
	$\varepsilon \times \mathcal{B}$ (%)	0.25 ± 0.03	0.48 ± 0.09	1.69 ± 0.18	0.85 ± 0.24
160	$\langle N \rangle$	0.3 ± 0.1	0.6 ± 0.1	1.9 ± 0.3	0.7 ± 0.2
$\int \mathcal{L}dt$ (pb^{-1})		13.5 ± 1.6	13.5 ± 1.6	13.5 ± 1.6	10.0 ± 1.2
Data		1	1	1	0
Physics background		0.2 ± 0.1	0.5 ± 0.1	2.1 ± 1.2	1.2 ± 0.8
Fake background		0.3 ± 0.2	0.5 ± 0.2	0.3 ± 0.3	0.3 ± 0.1
Total background		0.5 ± 0.2	1.0 ± 0.3	2.4 ± 1.3	1.5 ± 0.9

from the combined analysis of these channels (referred to as Combined Analysis I) is shown in table 5.1 along with the values obtained from the $t\bar{t} \rightarrow ee$ channel alone.

Having obtained the upper limit on the cross section for production of the top quark as a function of top mass, the lower limit on m_t is easily obtained. This is done by using the theoretical curve for the cross section for $t\bar{t}$ production at the tevatron (section 1.2.3). Figure 5.1 shows the curve of the upper limit (at 95% CL) on the cross section (for Combined Analysis I) intersecting with the curve of $t\bar{t}$ production cross section at the tevatron to give a lower limit on the mass of the top quark of 129 GeV/c^2. The change from the published value of 131 GeV/c^2 [61] results from the change in the value of the integrated luminosity.

5.2 *Cross Section for $t\bar{t}$ Production at Higher Mass Values ($>$ 120 GeV/c^2)*

Analysis II was optimized to search for $t\bar{t}$ production at higher mass values ($>$ 120 GeV/c^2). This analysis was combined with corresponding analyses from 6 more top decay channels which were also optimized to search for $t\bar{t}$ production at higher mass values. The six decay channels are: $e\mu$, $\mu\mu$, e-jets, μ-jets, e-jets/μ, and μ-jets/μ. The additional $\mu\mu$ channel is the dilepton channel in which both the Ws from $t\bar{t}$ decay to μs. The e-jets/μ and μ-jets/μ channels are the single lepton channels in which a soft muon is observed. These events are not included in the e-jets and μ-jets channels. The results from each of these analyses is shown in table 5.3 which shows the product of efficiency (ε) and branching ratio (B), the number of expected signal events ($\langle N \rangle$), the expected background (B) and the number of data events in each channel. The total number of observed events is 9 and the expected background is 3.8 ± 0.9. The combined analysis (referred to as Combined Analysis II) was used to calculate a background subtracted $t\bar{t}$ production cross section ($\sigma_{t\bar{t}}$ using the formula $\sigma_{t\bar{t}} = \sum_{i=1}^{7}(N_i - B_i)/\sum_{i=1}^{7} \varepsilon_i B_i \int \mathcal{L}_i dt$. Here N_i are the number of observed events,

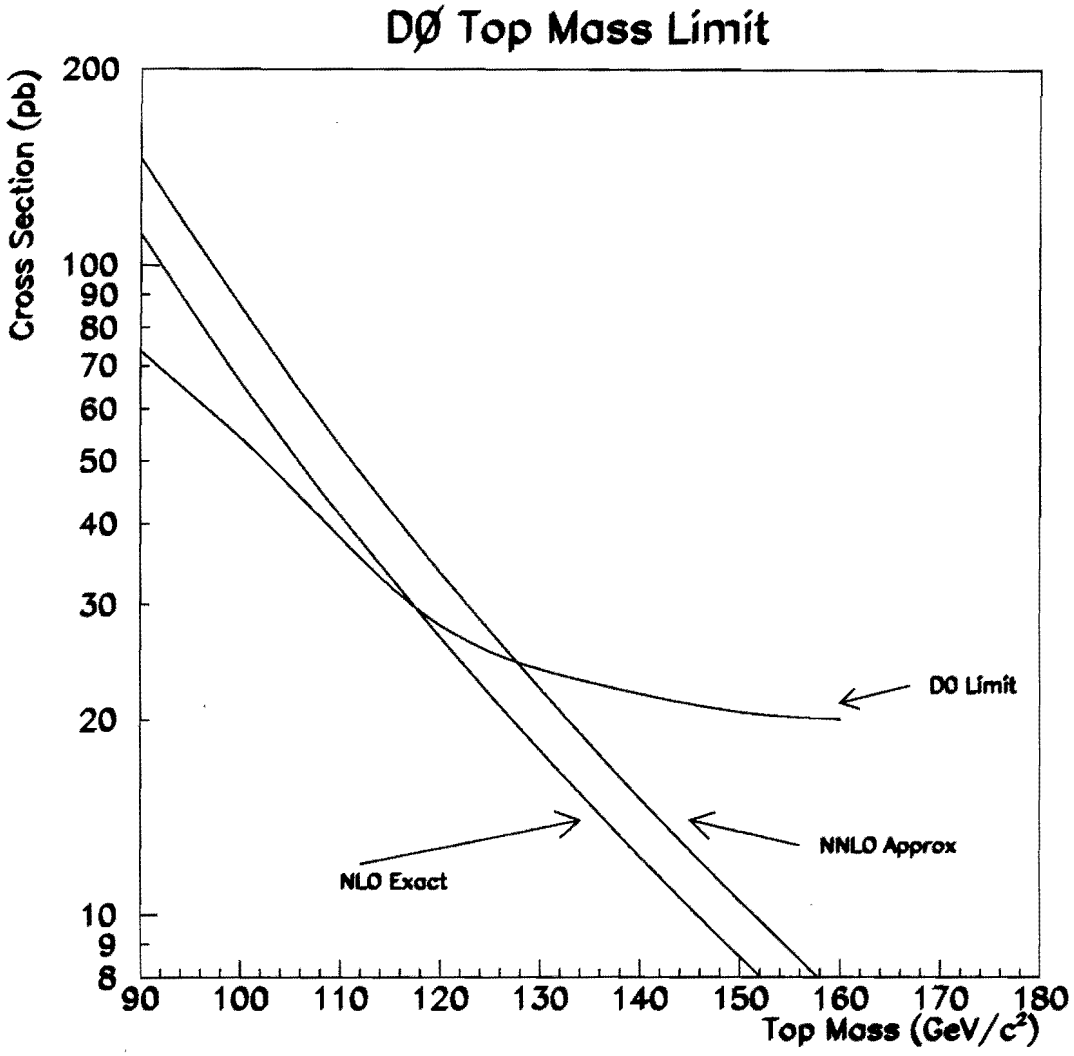

Figure 5.1. Upper limit (at 95% CL) on the cross section for top production obtained from Combined Analysis I (shown as the D0 limit) and the theoretical cross section for $t\bar{t}$ production at the tevatron.

Table 5.3. (Efficiency) $\times$ (branching ratio) ($\varepsilon \times B$), expected number of events for signal ($\langle N \rangle$) and background for the observed integrated luminosity ($\int \mathcal{L}dt$) and the number of events observed in data for the seven channels included in Combined Analysis II.

m_t (GeV/c^2)		ee	$e\mu$	$\mu\mu$	e-$jets$	μ-$jets$	e-$jets/\mu$	μ-$jets/\mu$	ALL
	$\varepsilon \times B$ (%)	0.18±0.02	0.32±0.06	0.13±0.02	1.1±0.3	0.8±0.2	0.6±0.2	0.4±0.1	
140	$\langle N \rangle$	0.41±0.07	0.72±0.16	0.22±0.04	2.5±0.6	1.3±0.4	1.3±0.4	0.7±0.2	7.1±1.1
	$\varepsilon \times B$ (%)	0.20±0.03	0.36±0.07	0.13±0.02	1.5±0.4	1.1±0.3	0.9±0.2	0.5±0.1	
160	$\langle N \rangle$	0.22±0.04	0.40±0.09	0.10±0.02	1.7±0.4	0.9±0.4	1.0±0.2	0.4±0.1	4.7±0.7
	$\varepsilon \times B$ (%)	0.21±0.03	0.41±0.07	0.13±0.02	1.6±0.4	1.1±0.3	1.1±0.2	0.7±0.1	
180	$\langle N \rangle$	0.12±0.02	0.23±0.05	0.05±0.01	0.9±0.2	0.5±0.2	0.6±0.2	0.3±0.1	2.7±0.4
$\int \mathcal{L}dt$ (pb^{-1})		13.5±1.6	13.5±1.6	9.8±1.2	13.5±1.6	9.8±1.2	13.5±1.6	9.8±1.2	
Data		0	1	0	2	2	2	2	9
Background		0.16±0.07	0.27±0.09	0.33±0.06	1.3±0.7	0.7±0.5	0.6±0.2	0.4±0.1	3.8±0.9

B_i are the expected background, ε_i are the detection efficiency, B_i the branching ratio and $\mathcal{L}_i$ the integrated luminosity. The summation i runs over the 7 decay channels used in the combined analysis. The calculation of the error on this cross section again involves the same problem of combining Gaussian and Poisson errors encountered while calculating the upper limit on the cross section. The same method is again used to evaluate the errors here. The results are plotted in figure 5.2. The solid line indicates the measured $t\bar{t}$ production cross section and the lightly shaded area the one standard deviation error. Also plotted in this figure is the theoretical value of the cross section and its uncertainty (dark shaded). The result from the CDF collaboration which showed evidence for $t\bar{t}$ production of top mass $174 \pm 10^{+13}_{-12}$ GeV/c^2 with a cross section of $13.9^{+6.1}_{-4.8}$ pb is shown as a shaded point with error bars.

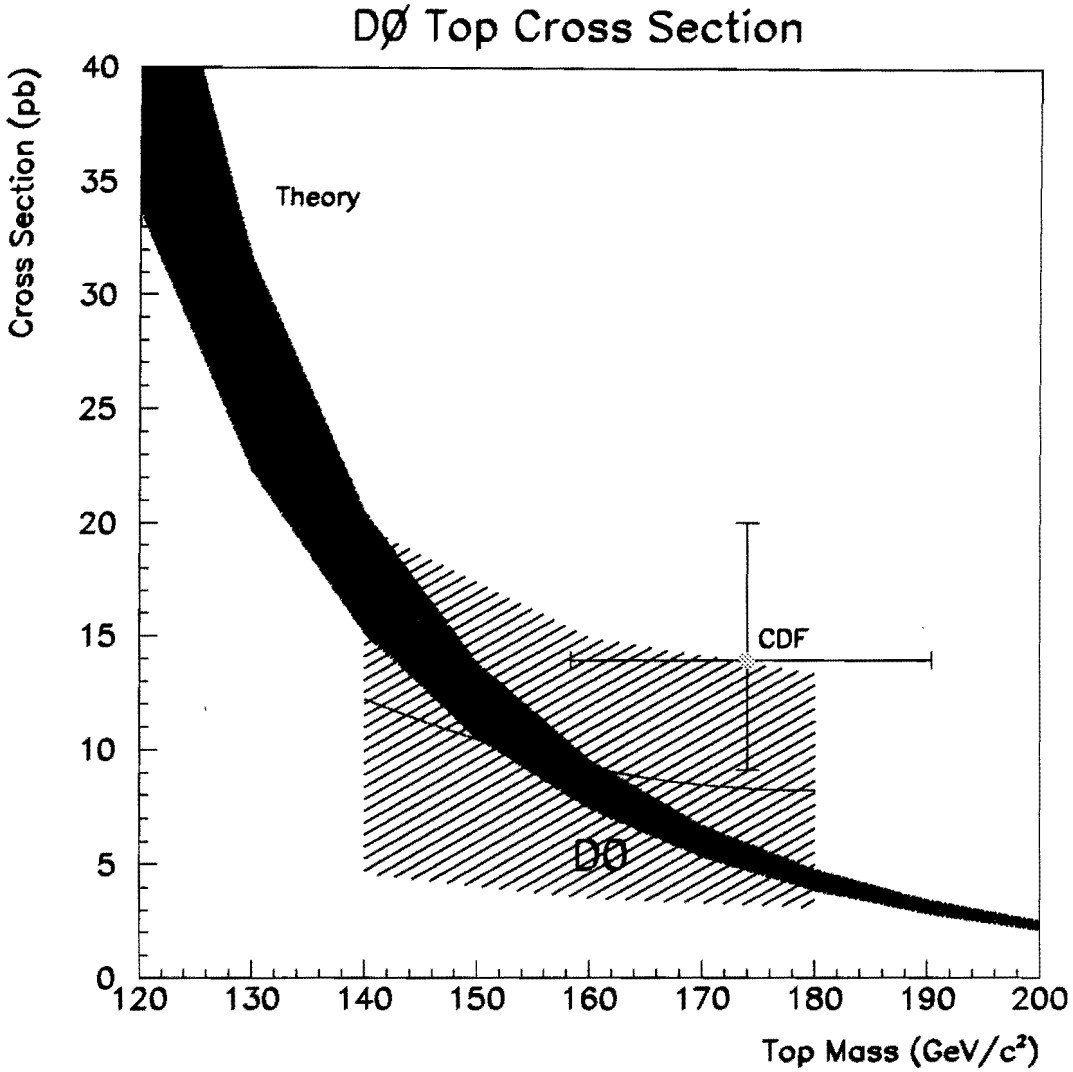

Figure 5.2. The measured $t\bar{t}$ production cross section for Combined Analysis II (solid line). The shaded band indicates the one standard deviation error. The theoretical prediction and the CDF result are also shown.

5.3 *Final remarks*

The search for the top quark in the dielectron decay mode shows no conclusive evidence for the existence of the top quark decaying according to the minimal standard model. However upper limits (at 95% CL) have been set on the production cross section of $t\bar{t}$ events at the tevatron for various top masses (using Analysis I).

The results of the analyses have been combined with top searches in other channels. Analysis I when combined with corresponding analyses to search for $t\bar{t}$ production in the decay channels $e\mu$, e-jets and μ-jets gives a lower limit on the mass of the top quark (at 95% CL) of 129 GeV/c^2.

Analysis II which was optimized for higher mass top (> 120 GeV/c^2) was combined with the corresponding analyses from the $e\mu$, $\mu\mu$, e-jets, μ-jets, e-jets/μ, and μ-jets/μ channels. The cross section for $t\bar{t}$ production for top mass 180 GeV/c^2 (160 GeV/c^2) obtained from this combined analysis is 8.2 ± 5.1 pb (9.2 ± 5.7 pb). This is consistent with theoretical cross section predictions for a Standard Model top. The cross section results are also consistent with results from the CDF collaboration (figure 5.2). The results, however, can not be regarded as evidence for the existence of the top quark.

APPENDIX A

Cross Sections and Branching Ratios

Total Cross Sections [63]: σ_{tot}

		$\sigma_{p\overline{p} \to t\bar{t}}$	
M_t	lower (pb)	central (pb)	upper (pb)
70	521	680	1102
80	265	335	507
90	145	180	258
100	85.2	103	142
110	52.7	61.6	81.4
120	33.7	38.9	49.7
140	15.1	16.9	20.5
160	7.41	8.16	9.53
180	3.86	4.21	4.78
200	2.09	2.26	2.52

...

$\sigma_{p\overline{p} \to Z} = 6257.5$ pb
$\sigma_{p\overline{p} \to W+X} = 20{,}857$ pb

...

$\sigma_{p\overline{p} \to W+njets}$ $(n \geq 0) = 1956.00 \pm 7.27 \pm 391.00$ pb
$(n \geq 1) = 566.80 \pm 3.33 \pm 113.00$ pb
$(n \geq 2) = 168.60 \pm 1.33 \pm 67.44$ pb
$(n \geq 3) = 45.44 \pm 0.63 \pm 27.26$ pb
$(n \geq 4) = 11.50 \pm 0.25 \pm 9.20$ pb

...

$\sigma_{p\bar{p} \to W^+W^-} \approx 10$ pb

...

$\sigma_{p\bar{p} \to W^\pm Z} \approx 2.4$ pb

...

$\sigma_{p\bar{p} \to W^\pm \gamma} \approx 60.6$ pb

...

$\sigma_{QCD \to b\bar{b}} \approx 25,000,000$ pb

...

$\sigma_{QCD \to c\bar{c}} \approx 300,000,000$ pb

...

$\sigma_{p\bar{p} \to \gamma \to ee} \approx 300$ pb ($M_{ee} > 25$ GeV)
$\sigma_{p\bar{p} \to \gamma \to \mu\mu} \approx 300$ pb ($M_{\mu\mu} > 25$ GeV)
$\sigma_{p\bar{p} \to \gamma \to \tau\tau} \approx 300$ pb ($M_{\tau\tau} > 25$ GeV)

Branching Ratios [63]: BR

$\mathrm{BR}(W \to e\nu_e, \mu\nu_\nu)$	$= 1/9$	$\approx 11.1\%$ (Ignoring $W \to \tau \to e\nu_e, \mu\nu_\mu$)
$\mathrm{BR}(Z \to ee, \mu\mu, \tau\tau)$		$\approx 3.34\%$
$\mathrm{BR}(Z \to u\bar{u}, c\bar{c})$		$\approx 11.8\%$
$\mathrm{BR}(Z \to d\bar{d}, s\bar{s}, b\bar{b})$		$\approx 15.2\%$
$\mathrm{BR}(W^+W^- \to ee + X, \mu\mu + X)$	$=1/81$	$\approx 1.23\%$
$\mathrm{BR}(W^+W^- \to e\mu + X)$	$=2/81$	$\approx 2.47\%$

...

$\mathrm{BR}(\tau \to \mu\overline{\nu_\mu}\nu_\tau)$	$\approx 17.8\%$
$\mathrm{BR}(\tau \to e\overline{\nu_e}\nu_\tau)$	$\approx 17.7\%$
$\mathrm{BR}(\tau^+\tau^- \to ee + X, \mu\mu + X)$	$\approx 3.1\%$
$\mathrm{BR}(\tau^+\tau^- \to e\mu + X)$	$\approx 6.3\%$
$\mathrm{BR}(\tau^+\tau^- \to e^+\mu^- + X)$	$\approx 6.3\%$

...

BIBLIOGRAPHY

[1] CDF Collaboration, F. Abe et al., *Phys. Rev. Lett.* **73** 225 (1994).

[2] G. L. Kane, *Top quark physics*, Preprint UM - TH - 91 - 32.

[3] D. H. Perkins, *Introduction to High Energy Physics*, (Addison-Wesley Publishing Company, 1987) pp. 6.

[4] K. Gottfried and V. F. Weisskopf, *Concepts of Particle Physics, Vol. 1*, (Oxford University Press, New York, 1984) pp. 99.

[5] M. G. Bowler, *Femtophysics*, (Pergamon Press, New York, 1990) pp 189.

[6] P. D. B. Collins and A. D. Martin, *Hadron Interactions*, (Adam Hilger Ltd, Bristol, 1984) pp. 126.

[7] K. Gottfried and V. F. Weisskopf, *Concepts of Particle Physics, Vol. 1*, (Oxford University Press, New York, 1984) pp. 165.

[8] A. Bean et al., *Phys. Rev. D* **35**,3533 (1987).

[9] G. L. Kane and M. Peskin, *Nucl. Phys. B* **195**, 29 (1982).

[10] G. L. Kane, *Modern Elementary Particle Physics*, (Addison-Wesley Publishing Company, 1993) pp. 268.

[11] CDF Collaboration, F. Abe et al., *Phys. Rev. D* **45**, 3921 (1992).

[12] Mark II Collaboration, G. S. Abrams et al., *Phys. Rev. Lett.* **63**, 2447 (1989).

[13] ALEPH Collaboration, D. Decamp et al., *Phys. Lett. B* **235**, 399 (1990).

[14] CDF Collaboration, *Proceedings of the 9th Topical Workshop in $p\bar{p}$ Collider Physics*, Tsukuba, edited by K. Kondo.

[15] D. Schaile, CERN-PPE/94-162, presented at 27th International Conference on High Energy Physics, Glasgow, July 1994.

[16] R. H. Dalitz and G. R. Goldstein, *Phys. Rev. D* **45**, 1531 (1992).

[17] E. Laenen, J. Smith and W. L. van Neerven, *Phys. Lett. B* **321**, 254 (1994).

[18] S. Abachi et. al., *Nucl. Instr. and Meth. in Phys. Res.*, A**338**, 185-253 (1994).

[19] D0 collaboration, *D0 detector design report*, D0 internal note # 137, Jul 1984. p. 3-1.

[20] W. J. Thompson, Ph.D thesis, State University of New York at Stony Brook, *Search for the top quark in the muon+jets channel at D0*, February 1994, pp 114-115.

[21] J. M. Butler, *Main Ring Deadtime*, D0 internal note # 1682, Feb. 1993.

[22] W. J. Thompson, Ph.D thesis, State University of New York at Stony Brook, *Search for the top quark in the muon+jets channel at D0*, February 1994, pp 111-142.

[23] A. R. Clark et. al., *Nucl. Instr. and Meth. in Phys. Res.,* A**279**, 243-248 (1989).

[24] D. Puseljić, Private communication.

[25] A. R. Clark et. al., *Nucl. Instr. and Meth. in Phys. Res.*, A**315**, 193 (1992).

[26] J. F. Detoeuf et. al., *Nucl. Instr. and Meth. in Phys. Res.*, A**265**, 157-166 (1988).

[27] J. F. Detoeuf et. al., *Nucl. Instr. and Meth. in Phys. Res.*, A**279**, 310-316 (1989).

[28] S. Rajagopalan, Ph.D thesis, Northwestern University. *The dE/dx capabilities of the D0 tracking system*, June 1992.

[29] P. Grannis, *The D0 Detector at the Fermilab Collider*, D0 internal note # 558, May 1987.

[30] J. Bantly et al., *The Level 0 Trigger for the D0 Detector*, D0 internal note # 1996, May 1987, p 1.

[31] J. Bantly et al., *The Level 0 Trigger for the D0 Detector*, D0 internal note # 1996, May 1987, p 2–5.

[32] FERMILAB-TM-1911, 1994, N. Amos et al., *Phys. Lett. B***243**, 158 (1990).

[33] J. Bantly et al., *The Level 0 Trigger for the D0 Detector*, D0 internal note # 1996, May 1987, p 5.

[34] J. Guida, *The D0 Calorimeter Trigger*, FERMILAB-Conf-92/370, Dec. 1992.

[35] M. Abolins et al., *Nucl. Instr. and Meth. in Phys. Res.*, A**289**, 543-560 (1990).

[36] M. Fatyga, *Tuning Electron ID parameters for the Level 2 Trigger using Test Beam Data*, D0 internal note # 1768, p 4.

[37] J. McKinley and J. Linneman, D0 internal note # 1354, Jan 1992.

[38] J. McKinley and J. Linneman, D0$CALOR_FILTER:L2_EM.DOC, D0 documentation file, Nov. 1993.

[39] D. Hedin, D0$MUON_UTIL$DOCS:MUON_ANALYSIS.MEM, D0 documentation file, Mar. 1992.

[40] R. Astur, D0$CALOR_FILTER:L2JETS.DOC, D0 documentation file, Oct. 1993.

[41] V. Balamurali et al., *Top Triggers*, D0 internal note # 1476.

[42] CTEQ Collaboration, in G. Sterman, ed., Handbook of Perturbative QCD, April 1993.

[43] J. E. Huth et al., in E.Berger, ed., Proc. Summer Study on High Energy Physics, Research Directions for the Decade, Snowmass, CO, Jun 25 - Jul 13, 1990.

[44] D0$LEVEL1:L1SIM.DOC, D0 documentation file, Dec. 1992.

[45] D. Claes, D0$LEVEL2:L2SIM.DOC, D0 documentation file, Apr. 1994.

[46] F. E. Paige and S. D. Protopopescu, *ISAJET 6.49: A Monte Carlo Event Generator for P-P and Pbar-P Reactions*, Fermilab Computing Division, PM0059, Aug. 1992.

[47] J. Womersley, *The D0 Monte Carlo*, D0 internal note # 1520, Aug. 1992.

[48] R. Brun et al., GEANT 3.15, program manual, CERN.

[49] N. J. Hadley, *Cone algorithm for jet finding*, D0 internal note # 904, Nov. 1989.

[50] M. Paterno, *A Study of the D0 Calorimeter $\not\!\!E_t$ Resolution Using Low E_t Jet Triggers*, D0 internal note # 1782, Jul. 1993.

[51] U. Heintz, *"Standard" EM Energy Scale Correction for RECO V10*, D0 internal note # 1758, Jun. 1993.

[52] H. Weerts, *Studies of Jet Production with the D0 Detector*, D0 internal note # 1956A, Oct. 1993.

[53] F. Abe et al., (CDF Collaboration), FERMILAB-Pub-92/182-E, 1992.

[54] A. Milder, Ph. D. thesis, University of Arizona, *Dijet Angular distributions at $\sqrt{s} = 1800$ GeV Using the D0 Detector*, 1993, p.76-108.

[55] B. Kehoe, *Resolution Bias in Jet Response Measurement*, D0 internal note # 2052, Feb. 1994.

[56] J. Ohnemus, Phys. Rev. D44, 1403 (1991).

[57] U. Heintz and M. Narain, *A Study of Electron ID Efficiencies using $Z \rightarrow ee$ decay*, D0 internal note # 1814, July 1993.

[58] J. Cochran, *$t\bar{t} \rightarrow$ dileptons: The Background Bible, Vol. 1.1*, D0 internal note in preparation.

[59] R. Partridge, *Top Limit Calculation*, D0 internal note # 1806, July 1993.

[60] Particle Data Group, "Review of Particle Properties", *Phys. Rev. D50, Part I*, Aug. 1994, p 1280.

[61] S. Abachi et. al., *Phys. Rev. Lett.*, **72**, 2138 (1994).

[62] FERMILAB-TM-1911, 1994.

[63] J. Cochran, Ph.D thesis, State University of New York at Stony Brook, *Search for Truth in the $e\mu$ channel at D0*, December 1993, Appendix A.